TECHNICAL
REPORT

ISO/TR
19319

Second edition
2013-03-15

Surface chemical analysis — Fundamental approaches to determination of lateral resolution and sharpness in beam-based methods

Analyse chimique des surfaces — Approche fondamentale pour la détermination de la résolution latérale et de la netteté par des méthodes à base de faisceau

Reference number
ISO/TR 19319:2013(E)

ISO copyright office
Case postale 56 • CH-1211 Geneva 20
Tel. + 41 22 749 01 11
Fax + 41 22 749 09 47
E-mail copyright@iso.org
Web www.iso.org

Published in Switzerland

Contents

Page

Foreword

ISO (the International Organization for Standardization) is a worldwide federation of national standards bodies (ISO member bodies). The work of preparing International Standards is normally carried out through ISO technical committees. Each member body interested in a subject for which a technical committee has been established has the right to be represented on that committee. International organizations, governmental and non-governmental, in liaison with ISO, also take part in the work. ISO collaborates closely with the International Electrotechnical Commission (IEC) on all matters of electrotechnical standardization.

International Standards are drafted in accordance with the rules given in the ISO/IEC Directives, Part 2.

The main task of technical committees is to prepare International Standards. Draft International Standards adopted by the technical committees are circulated to the member bodies for voting. Publication as an International Standard requires approval by at least 75 % of the member bodies casting a vote.

In exceptional circumstances, when a technical committee has collected data of a different kind from that which is normally published as an International Standard ("state of the art", for example), it may decide by a simple majority vote of its participating members to publish a Technical Report. A Technical Report is entirely informative in nature and does not have to be reviewed until the data it provides are considered to be no longer valid or useful.

Attention is drawn to the possibility that some of the elements of this document may be the subject of patent rights. ISO shall not be held responsible for identifying any or all such patent rights.

ISO/TR 19319 was prepared by Technical Committee ISO/TC 201, *Surface chemical analysis*, Subcommittee SC 2, *General procedures*.

This second edition cancels and replaces the first edition (ISO/TR 19319:2003), which has been technically revised.

Introduction

Surface-analytical techniques such as SIMS, AES and XPS enable imaging of surfaces. The most relevant parameter of element or chemical maps and line scans is the lateral resolution, also called image resolution.[1)]Therefore well defined and accurate procedures for the determination of lateral resolution are required. Those procedures together with appropriate test specimen are basic preconditions for comparability of results obtained by imaging surface-analytical methods and performance tests of instruments as well. This Technical Report is intended to serve as a basis for the development of International Standards.

Nowadays there is some confusion in the community in the understanding of the term “lateral resolution”. Definitions originating from different fields of application and different communities of users can be found in the literature. Unfortunately they are inconsistent in many cases. As a result, values of “lateral resolution” published by manufacturers and users having been derived by using different definitions and/or determined by different procedures cannot be compared to each other. It is the intention of this Technical Report to basically describe different approaches for the characterization of lateral resolution including their interrelations.

The term resolution was introduced with respect to the performance of microscopes by Ernst Abbe.[1] Later on it was applied to spectroscopy by Lord Rayleigh.[2] It is based on the diffraction theory of light and the original definition of lateral resolution as “the minimum spacing at which two features of the image can be recognised as distinct and separate” is in common use in the light and electron microscopy communities as documented in the standard ISO 22493:2008.[3]

However, in the surface analysis community a very different approach, the “knife edge method”, is the most popular one for the determination of lateral resolution. This method is based on evaluation of an image or of a line scan over a straight edge. Here lateral resolution is characterized by parameters describing the steepness of the edge spread function ESF. The standard “ISO 18516:2006 Surface Chemical Analysis – Auger electron spectroscopy and X-ray photoelectron spectroscopy – Determination of lateral resolution”[4] is limited to this approach. But the ESF and corresponding rise parameters $D_{\text{x-(1-x)}}$ are more related to image sharpness than to lateral resolution which refers to two separated features.

The reason why the original meaning of resolution is not commonly implemented in the common practice in surface analysis is the lack of suitable test specimens having the required features in the sub-µm range. However, recently a new type of test specimen was developed featuring a series of flat square-wave gratings characterized by chemical contrast and different periods.[5,6] Such test specimens may enable an implementation of the original definition of lateral resolution into practical approaches in surface chemical analysis.

Having solved the problem of availability of appropriate test specimens another problem has to be solved: The establishment of a criterion for whether two features are separated or not. The Rayleigh criterion[2] was developed for diffraction optics and its application in imaging surface analysis is not straightforward. The Sparrow criterion[7] defines a resolution threshold exclusively by the existence of a minimum between two maxima. Actually, for practical imaging in surface analysis, noise is a relevant feature especially at the limit of resolution. Therefore the Sparrow criterion will fail to solve the problem. The solution is to develop a resolution criterion relying on the detection of a minimum between two features but additionally considering noise effects.

The lateral resolution of imaging systems is strongly related to a number of functions describing the formation of images:

— the modulation transfer function,

— the contrast transfer function,

— the point spread function,

---

1) The term “image resolution” is used in the microscopy community whereas in the surface analysis community the term “lateral resolution” is common practice to distinguish it from “depth resolution”.

- — the line spread function and
- — and the edge spread function.

Those functions may be utilized to describe the performance of optical instruments and instruments used for imaging in surface analysis as well. In particular the contrast transfer function has been used successfully for the benefit of the determination of lateral resolution of imaging instruments in surface analysis.

Section 4 of this report describes the basics of procedures for the analysis of images of stripe patterns, narrow stripes and step transitions. A comparison of all procedures related to lateral resolution and sharpness is given in 4.1.7.

Section 5 of the report describes physical factors affecting lateral resolution, analysis area and sample area viewed by the analyser in Auger electron spectroscopy and X-ray photoelectron spectroscopy. Section 6 of the report gives guidance on the determination of sample area viewed by the analyser in applications of Auger electron spectroscopy and X-ray photoelectron spectroscopy.

Surface chemical analysis — Fundamental approaches to determination of lateral resolution and sharpness in beam-based methods

1 Scope

This Technical Report describes:

a) Functions and their relevance to lateral resolution:

  1) Point spread function (PSF) — see 4.1.1

  2) Line spread function (LSF) — see 4.1.2

  3) Edge spread function (ESF) — see 4.1.3

  4) Modulation transfer function (MTF) — see 4.1.4

  5) Contrast transfer function (CTF) — see 4.1.5.

b) Experimental methods for the determination of lateral resolution and parameters related to lateral resolution:

  1) Imaging of a narrow stripe — see 4.2

  2) Imaging of a sharp edge — see 4.3

  3) Imaging of square-wave gratings — see 4.4.

c) Physical factors affecting lateral resolution, analysis area and sample area viewed by the analyser in Auger electron spectroscopy and X-ray photoelectron spectroscopy — see Clauses 5 and 6.

2 Terms and definitions

For the purposes of this document, the following terms and definitions apply.

2.1
analysis area
<sample> two-dimensional region of a sample surface measured in the plane of that surface from which the entire analytical signal or a specified percentage of that signal is detected

[SOURCE: ISO 18115:2010, definition 5.8]

2.2
contrast transfer function
CTF
ratio of the image contrast to the object contrast of a square-wave pattern as a function of spatial frequency

Note 1 to entry: In this document the contrast transfer function CTF has been used also with an abscissa expressed in terms of w_{LSF}/P and is called the generalized contrast transfer function in those cases (cf. 4.4.3.2). w_{LSF} is the full width at half maximum of the line spread function LSF

Note 2 to entry: In transmission electron microscopy and other phase sensitive methods the term contrast transfer function is used with a different meaning considering amplitude as well as phase information.

2.3
cut-off frequency of the contrast transfer function
lowest spatial frequency at which the contrast transfer function CTF equals to zero

Note 1 to entry: In this document the spatial frequency at which the contrast transfer function CTF equals the threshold of resolution under consideration of noise (cf. 4.4.3.3) is called effective cut-off frequency of the contrast transfer function.

2.4
edge spread function
ESF
normalized spatial signal distribution in the linearized output of an imaging system resulting from imaging a theoretical infinitely sharp edge

[SOURCE: ISO 12231:2012, definition 3.43]

2.5
effective cut-off frequency
see cut-off frequency of the contrast transfer function, Note 1 to entry

2.6
effective lateral resolution
minimum spacing of two stripes of a square-wave grating at which the dip of signal intensity between two maxima of the image is at least 4 times the reduced noise σ_{NR}

2.7
generalized contrast transfer function
see **contrast transfer function**, Note 1 to entry

2.8
image contrast
c_i
$c_i = (I_{max}–I_{min})/(I_{max}+I_{min}) = \Delta I/2\ I_{mean}$ (Michelson contrast), where I_{max}, I_{min} and I_{mean} are signal intensities in the image

Note 1 to entry: Other definitions (not used in this document) include: difference in signal between two arbitrarily chosen points of interest (P_1, P_2) in the image field, normalized by the maximum possible signal available under the particular operating conditions, $c_i = |S_2 - S_1|/S_{max}$ (ISO 22493:2008, definition 5.3).

Note 2 to entry: With respect to aperiodic patterns the Weber contrast $c = (I - I_b)/I_b$ is used to quantify the contrast between a feature with the signal intensity I and the background signal intensity I_b.

Note 3 to entry: With respect to periodic object patterns, the terms contrast and modulation often are used synonymously.

2.9
image resolution
minimum spacing at which two features of the image can be recognised as distinct and separate

[SOURCE: ISO 22493:2008, definition 7.2]

2.10
lateral resolution
minimum distance between two features (in this document the period of a square wave grating) which can be imaged in that way, that the dip between two maxima is at least 4 times the **reduced noise**σ_{NR} (cf. 4.4.2.3)

Note 1 to entry: This definition is in accordance with the definition of image resolution given in ISO 22493:2008.

Note 2 to entry: This definition is different from the definition of lateral resolution given in ISO 18115:2010.

2.11

linear system

system whose response is proportional to the level of input signals

[SOURCE: ISO 9334:1995, definition 3.1]

2.12

line spread function

LSF

normalized spatial signal distribution in the linearized output of an imaging system resulting from imaging a theoretical infinitely thin line

[SOURCE: ISO 12231:2012, definition 3.94]

2.13

modulation

m

measure of degree of variation in a sinusoidal signal

$$m=\left(I_{\max}-I_{\min}\right)/\left(I_{\max}+I_{\min}\right)$$

[SOURCE: ISO 9334:1995, definition 3.17]

2.14

modulation transfer function MTF

ratio of the image modulation to the object modulation as a function of spatial frequency

[SOURCE: ISO/IEC 19794-6:2011, definition 4.7]

2.15

noise

time-varying disturbances superimposed on the analytical signal with fluctuations leading to uncertainty in the signal intensity

Note 1 to entry: An accurate measure of noise can be determined from the standard deviation of the fluctuations. Visual or other estimates, such as peak to peak noise in a spectrum or in a line scan, may be useful as semiquantitative measures of noise.

[SOURCE: ISO 18115:2010, definition 5.315]

Note 2 to entry: By averaging over $S_{\mathrm{PP}}/4$ data points of the line scan over a square-wave grating the standard deviation of noise σ_{N} can be reduced by a factor of $(S_{\mathrm{PP}}/4)^{1/2}$. $\sigma_{\mathrm{NR}} = (4/S_{\mathrm{PP}})^{1/2}\sigma_{\mathrm{N}}$ is called **reduced noise** in this document (cf. 4.4.2.3). S_{PP} means number of sampling points per period.

2.16

object pattern

spatial distribution of a sample property seen by the imaging instrument

[SOURCE: ISO 9334:1995, definition 4.1]

2.17

optical transfer function

OTF

frequency response, in terms of spatial frequency, of an imaging system to a sinusoidal object pattern and Fourier transform of the imaging system’s point spread function

[SOURCE: ISO 9334:1995, definition 3.8]

2.18
point spread function
PSF
normalized distribution of signal intensity in the image of an infinitely small point

[SOURCE: ISO 9334:1995, definition 3.5]

2.19
reduced noise
see **noise**, Note 2 to entry

2.20
Rose criterion
condition for an average observer to be able to distinguish small features in the presence of noise, which requires that the change in signal for the feature exceeds the noise by a factor of at least three

[SOURCE: ISO 22493:2008, definition 5.3.7]

2.21
sample area viewed by the analyser
two-dimensional region of a sample surface measured in the plane of that surface from which the analyser can collect an analytical signal from the sample or a specified percentage of that signal

2.22
sampling points per period
S_{PP}
grating period divided by sampling step width

Note 1 to entry: For the case of 3-stripe gratings the image of the grating may have a smaller period than the object grating (cf. 4.4.1.1). In this case it must be explained whether the grating period of the object or the image is considered.

2.23
signal-to-noise ratio
$R_{\mathrm{S/N}}$
ratio of the signal intensity to a measure of the total **noise** in determining that signal

[SOURCE: ISO 18115:2010, definition 5.427]

2.24
spatial frequency
reciprocal of the period of a periodic object pattern (grating)

3 Symbols and abbreviated terms

AES	Auger electron spectroscopy
c_{i}	image contrast
c_{o}	object contrast
$(c_{\mathrm{i}}/c_{\mathrm{o}})_{\mathrm{ThR}}$	$c_{\mathrm{i}}/c_{\mathrm{o}}$ at the threshold of resolution
CTF	contrast transfer function
d	distance between two narrow stripes
D	dip between two maxima
d_{gr}	distance between two consecutive gratings

D_{LSF}	data distance of the MTF calculated by Fourier transform
D_{ThR}	dip at the threshold of resolution
$D_{\mathrm{x-(100-x)}}$	ESF steepness parameter giving the distance between points of well-defined intensities x and 100-x (e.g. 20 % to 80 %) of the profile over a straight edge
DNR	dip-to-noise ratio
erf	error function
ESF	edge spread function
F_{r}	fit range
FWHM	full width at half maximum
G	gap between two stripes
G(x)	Gaussian function
$\mathrm{i}(x,y)$	normalized intensity distribution of measured signals in the image
I_{i}	incident beam current (in AES)
I_{max}	maximum value of signal intensity in the image of a 3-stripe-grating (A-B-A)
$I_{\mathrm{max\,l}}$	signal intensity of the left maximum in the image of a 3-stripe-grating (A-B-A)
$I_{\mathrm{max\,r}}$	signal intensity of the right maximum in the image of a 3-stripe-grating (A-B-A)
I_{min}	signal intensity of the minimum in the image of a 3-stripe-grating (A-B-A)
I_{pll}	intensity of the lower plateau of constant concentration
I_{plu}	intensity of the upper plateau of constant concentration
$J_{\mathrm{A}}(r)$	intensity distribution of detected Auger electrons as a function of the radius r
$J_{\mathrm{Ab}}(r)$	intensity distribution of detected Auger electrons that were created by backscattered
$J_{\mathrm{Ai}}(r)$	intensity distribution of detected Auger electrons that were created by the incident beam
k	spatial frequency
k_{S}	steepness parameter of the logistic function
L	length
$\mathrm{L}(x)$	Lorentzian function
L_{pl}	Length of a plateau of constant concentration
LSF	line spread function
m	modulation
m_{i}	image modulation
m_{o}	object modulation
M_{LSF}	length range of measured LSF values

MTF	modulation transfer function
$\mathrm{o}(x,y)$	object pattern
OTF	optical transfer function
P	grating period
P_0	period of the largest non-resolved grating
P_1	period of the first (finest) resolved grating
P_2	period of the second resolved grating
P_{int}	period at $R_{\mathrm{D/RN}} = 4$ determined by interpolation between P_0 and P_1
P_{ext}	period at $R_{\mathrm{D/RN}} = 4$ determined by extrapolation with P_1 and P_2
PSF	point spread function
PSV1	type 1 Pseudo-Voigt function
PSV2	type 2 Pseudo-Voigt function
q	grading factor of consecutive grating periods $q = P_{\mathrm{n+1}}/P_{\mathrm{n}}$
R	backscattering factor (in AES)
r	radius from the centre of the incident electron beam on the sample surface (in AES)
r_{e}	effective lateral resolution
$R_{\mathrm{D/RN}}$	ratio of dip-to-reduced-noise
R_{LSF}	length range where LSF data are used for Fourier transform
$R_{\mathrm{S/N}}$	signal-to-noise ratio
r_{max}	upper limit of integration in Formula (65)
s	mean deviation of w_{LSF} determined by a fitting procedure
S_{w}	sampling step width
S_{pp}	sampling points per period as a variable
spp	dimension unit of the variable S_{PP}
SIMS	Secondary Ion Mass Spectrometry
u	uncertainty of a quantity
U	expanded uncertainty of a quantity
U_{c}	combined expanded uncertainty of a quantity
w	full width at half maximum of a peak function
w_{G}	full width at half maximum of the Gaussian part of a type 2 Pseudo-Voigt function
w_{im}	full width at half maximum of the upper plateau of constant concentration in an image of

w_L	full width at half maximum of the Lorentzian part of a type 2 Pseudo-Voigt function
w_LSF	full width at half maximum of the line spread function
w_S	width of a stripe in the object pattern
x, x'	length variable
XPS	X-ray photoelectron spectroscopy
y, y'	length variable
Δr	lateral resolution
Δr (50)	lateral resolution determined from a 25% to 75% intensity change in a line profile over a straight edge
η	Lorentzian fraction of a Pseudo-Voigt function
σ_b	Gaussian parameter describing the radial distribution of backscattered electrons (in AES)
σ_i	Gaussian parameter describing the radial distribution of the incident electron beam (in AES)
σ_N	standard deviation of noise
σ_NR	standard deviation of reduced noise

4 Determination of lateral resolution and sharpness by imaging of stripe patterns

4.1 Theoretical background

4.1.1 Image formation and the point spread function (PSF)

The imaging process describes the formation of an image as a result of the interaction between an object and an imaging system. The object may be characterized by the object pattern $\mathrm{o}(x,y)$. This is determined by a distribution of a certain parameter, for instance a concentration of an element, in the object plane (x, y) and the relation of this parameter to the respective signal intensity seen by the imaging instrument. The imaging system is represented by its point spread function (PSF). The $\mathrm{PSF}(x\text{-}x',y\text{-}y')$ is the normalized intensity distribution of measured signals in the image $\mathrm{i}(x',y')$ related to a point at position (x,y) in the object pattern $\mathrm{o}(x,y)$.

For linear systems (cf. terms and definitions) the image is formed by the superposition of all intensity distributions produced in the image plane by each individual point of the object pattern $\mathrm{o}(x,y)$.[8] This is mathematically described by the convolution integral

$$\mathrm{i}(x',y') = \int_{-\infty}^{+\infty}\!\!\int \mathrm{o}(x,y)\,\mathrm{PSF}(x'-x,y'-y)\,\mathrm{d}x\,\mathrm{d}y \qquad (1)$$

This convolution integral can be written as

$$\mathrm{i}(x,y) = \mathrm{o}(x,y) \otimes \mathrm{PSF}(x,y) \qquad (2)$$

where $\otimes$ denotes the convolution operation. Formulae (1) and (2) reveal that the image is a weighted sum of point spread functions emerging from every point of the object. Figure 1 illustrates the image formation and the influence of the PSF on the image quality in terms of sharpness.

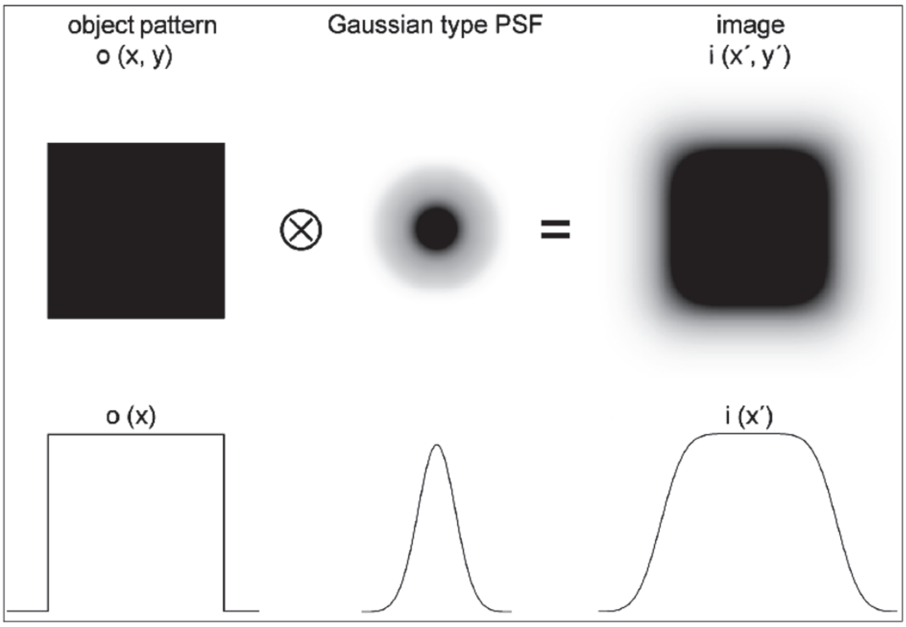

Figure 1 — Top: Imaging of a square simulated by the convolution of the square with a Gaussian PSF where ⊗ denotes the convolution operation. Bottom: X-cuts of object, PSF and image, respectively

In the example given in Figure 1 the dimension of the object and the PSF are of the same order of magnitude. However, for practical applications, two borderline cases of imaging are of particular interest:

1. If the FWHM of the PSF is small compared to the smallest details of the imaged object, then the convolution yields an image that is very similar to the original object. In that case the imaging process (Figure 2a) delivers sharp images of the object.
2. If the FWHM of the PSF is large compared to the imaged object, then the convolution yields the PSF (Figure 2b). The latter case can be exploited to determine the PSF without a deconvolution procedure.

   The PSF describes the performance of an imaging instrument with respect to lateral resolution and the sharpness of images obtained. The smaller the FWHM of the PSF the better is the lateral resolution.

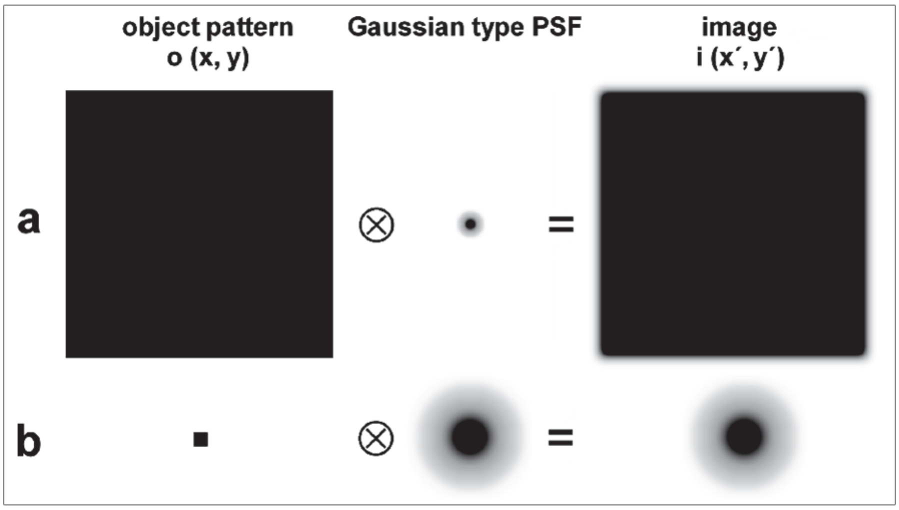

Figure 2 — Two borderline cases of imaging: a) The object is large compared to the FWHM of the PSF. This case is ideal for imaging. b) The object is small compared to the FWHM of the PSF. This case is ideal for the determination of the PSF

4.1.2 The line spread function (LSF)

The LSF is the normalized intensity distribution in the image of a narrow line and yields a one-dimensional description of image quality. According to the model of image formation described above (Figure 1) the LSF corresponds to the convolution of the PSF with an infinitely narrow line, mathematically described by the Dirac delta function δ(x):

$$\mathrm{LSF}(x)=\int_{-\infty}^{\infty}\int_{-\infty}^{\infty}\mathrm{PSF}(x',y)\delta(x-x')\mathrm{d}x'\mathrm{d}y \tag{3}$$

$$=\int_{-\infty}^{+\infty}\mathrm{PSF}(x,y)\mathrm{d}y \tag{4}$$

The LSF is generally different from a cross section through the two-dimensional PSF. In Figure 3 this is demonstrated for the top hat distribution. Only in the case of a PSF represented by a two-dimensional Gaussian distribution the LSF is identical to the corresponding one-dimensional distribution:

$$\mathrm{G}(x)=\frac{I_0}{\sigma\sqrt{2\pi}}\exp\left(-(x-x_0)^2/2\sigma^2\right) \tag{5}$$

The LSF approach is more often used for the determination of lateral resolution than the PSF approach and the full width at half maximum (FWHM) of the LSF is often used as a measure of lateral resolution. However, with the availability of well-defined nanoscaled pointlike objects, the PSF approach may become relevant in the future, too. When a narrow line is imaged, a considerable number of line scans can usually be added by appropriate software tools and the LSF information is obtained at reasonable signal-to-noise ratios.

Finally it should be mentioned that the LSF is not necessarily a Gaussian shaped function. Other shapes as Lorentzian, Voigt function, etc., are possible (cf. 4.2.1). Therefore two imaging instruments having LSFs with the same FWHM but with different shapes will differ in the lateral resolution which can be achieved (this effect will be demonstrated in 4.4.3.1).

4.1.3 The edge spread function (ESF)

The ESF is the intensity distribution in the image of an edge (step transition) measured in the direction perpendicular to that of the edge. The ESF is the integral of the LSF

$$\mathrm{ESF}(x)=\int_{-\infty}^{x}\mathrm{LSF}(x')\mathrm{d}x' \tag{6}$$

The ESF may be determined by a convolution of the PSF with a step function.

The distance between points of well defined relative intensity (e.g. 12 %–88 %, 16 %–84 %, 20 %–80 % or 25 %–75 %) in an ESF is often taken as a measure of lateral resolution. For a Gaussian LSF the distance between the 12 % and 88 % intensity points (indicated in Figure 4) corresponds to its FWHM.

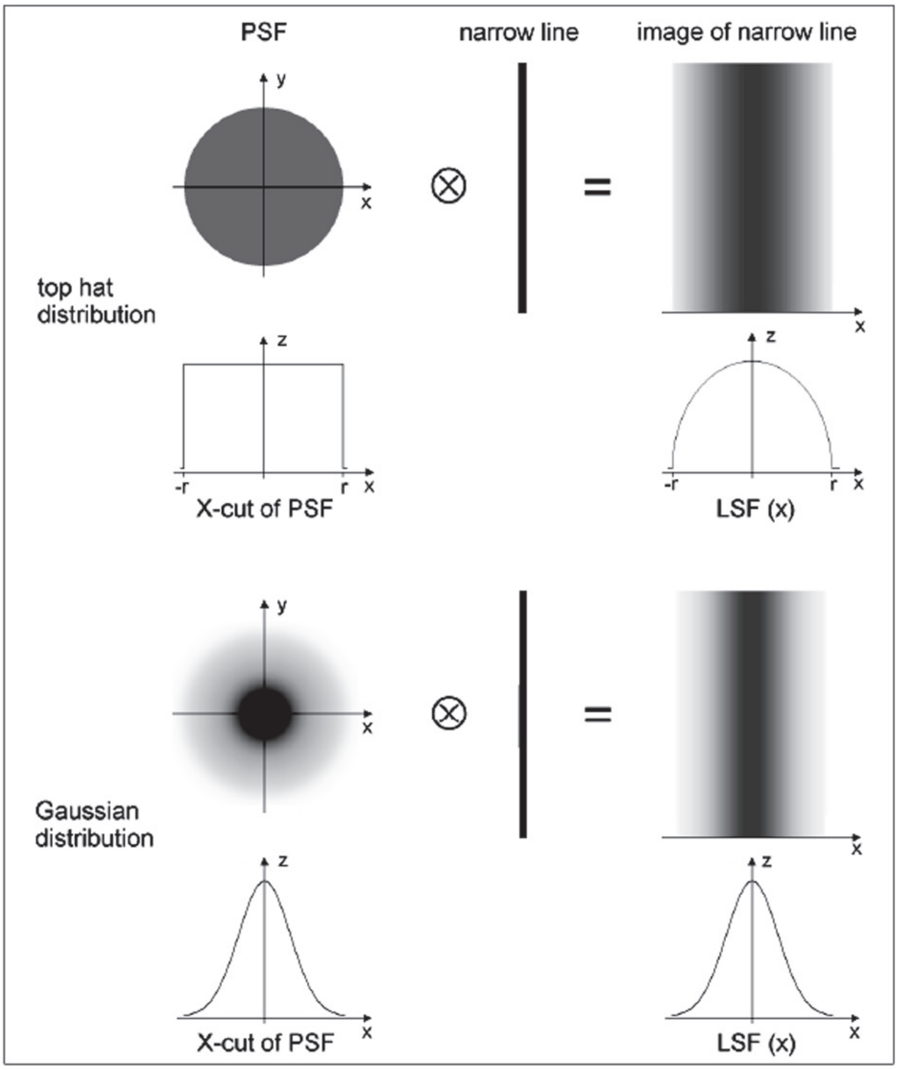

Figure 3 — Determination of the LSF by imaging of a narrow line. Different types of PSF were convoluted with a narrow line. The z-axis denotes the signal intensity within the images (from [9])

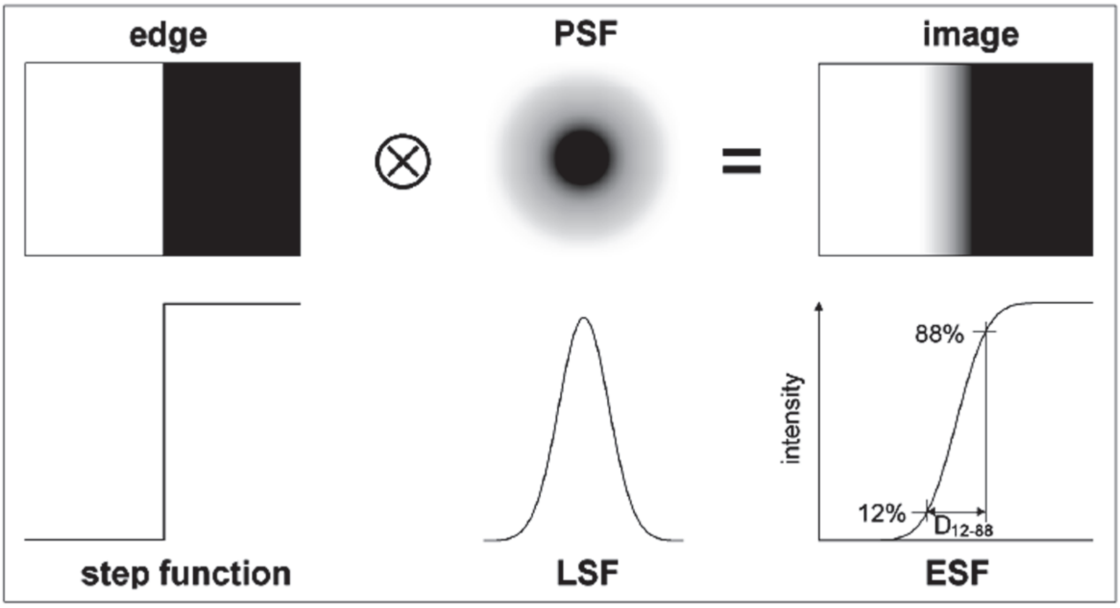

Figure 4 — Determination of the ESF by imaging of an edge. The value $D_{12\text{-}88}$ is used as a measure of lateral resolution

4.1.4 The modulation transfer function (MTF)

The concept of the optical transfer function (OTF) was developed to characterize the performance of imaging systems.[8,10] It was adapted from electronic and communication engineering to optical imaging and is based on the transfer of sinusoidal signals. “The optical transfer function (OTF) is the frequency response, in terms of spatial frequency (cf. terms and definitions), of an optical system to sinusoidal distributions of light intensity in the object plane”[10]. “The part of OTF describing the reproduction of contrast is called the modulation transfer function (MTF), while the phase component is called the phase transfer function (PTF)”[8]. Both parts of the OTF may be determined by imaging a sine wave grating. With respect to surface analytical methods, only the MTF is of interest.

The modulation of periodic patterns in objects and images is defined as

$$m=\left(I_{\max}-I_{\min}\right)/\left(I_{\max}+I_{\min}\right) \tag{7}$$

where $I_{\max}$ is the maximum value of a periodic structure and $I_{\min}$ is the minimum value between two maxima (cf. Figure 5).

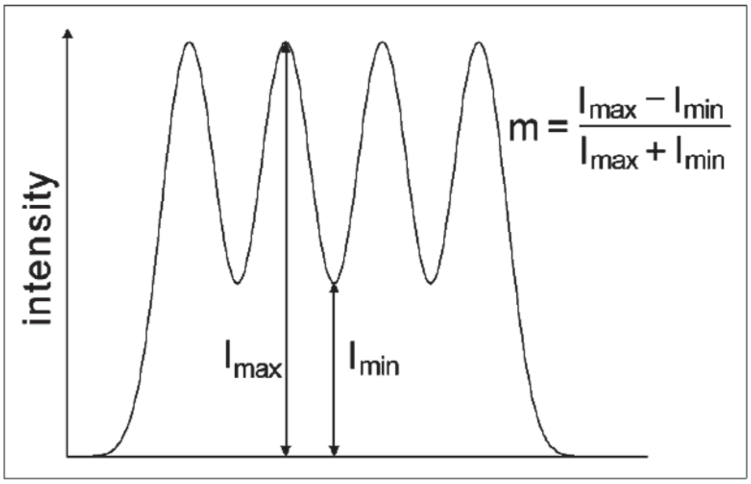

Figure 5 — Definition of modulation *m*

The MTF describes the transfer of the object modulation m_o to the image modulation m_i as a function of spatial frequency *k*

$$\mathrm{MTF}\ (k) = m_i/m_o \tag{8}$$

where k is the reciprocal of the period of a sine wave grating. The object modulation m_o is based, for instance, on differences in sample composition and it can be determined from the respective image profile as outlined in 4.4.1.3.

An ideal imaging instrument is characterized by $m_i = m_o$ and correspondingly MTF = 1 for all k values. In reality imaging is always characterized by a decreasing image modulation m_i vs. increasing spatial frequency (Figure 6). Therefore the MTF can be used to describe the performance of an imaging instrument. The MTF is directly related to its lateral resolution.

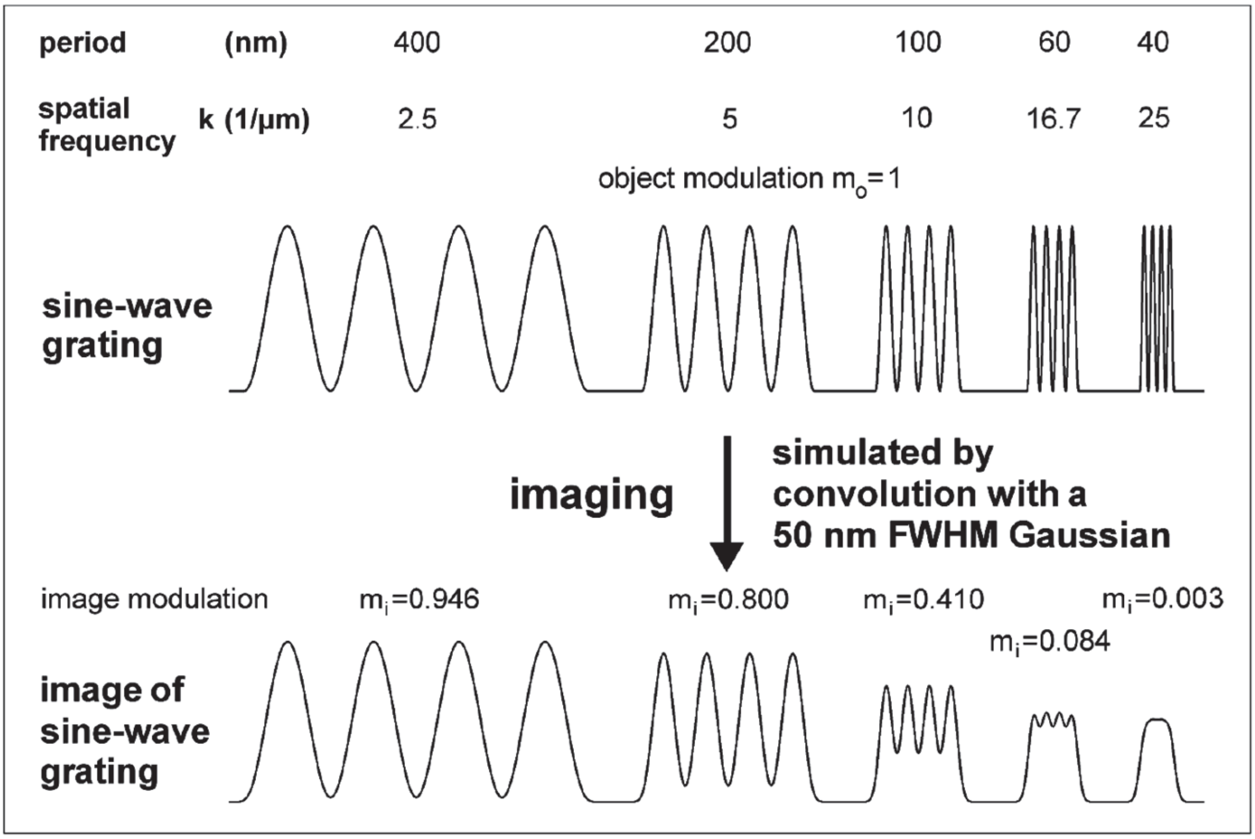

Figure 6 — Imaging of sine wave gratings with different periods and the transfer of modulation from object to image

Another definition of the optical transfer function OTF is based on the fact, that the OTF is the Fourier transform (FT) of the point spread function P

$$\mathrm{OTF}(k,l)=\mathrm{FT}[\mathrm{PSF}(x,y)]=\int_{-\infty}^{\infty}\int \mathrm{PSF}(x,y)\exp[-i2\pi(xk+yl)]\mathrm{d}x\mathrm{d}y \tag{9}$$

where k and l are spatial frequency variables associated with the space coordinates (*x,y*), respectively. The OTF is a complex function and the MTF is the normalized modulus of the OTF. For the one-dimensional case (and only this will be treated below) the MTF is given by the Fourier transform of the line spread function (LSF)

$$\mathrm{MTF}(k)=\left|\mathrm{OTF}(k)\right|=\int_{-\infty}^{\infty}\mathrm{LSF}(x)\exp(-i2\pi xk)\mathrm{d}x \Big/ \int_{-\infty}^{\infty}\mathrm{LSF}(x)\mathrm{d}x \tag{10}$$

A narrow LSF in position space yields a wide MTF in spatial frequency space, and vice versa. The Fourier transform of a Gaussian distribution is again Gaussian and therefore a Gaussian LSF yields a Gaussian MTF. Figure 7 demonstrates that both methods of calculating the MTF, Fourier transformation of the LSF and determination of m_i from the image of a sine wave grating, yield exactly the same values of the MTF.

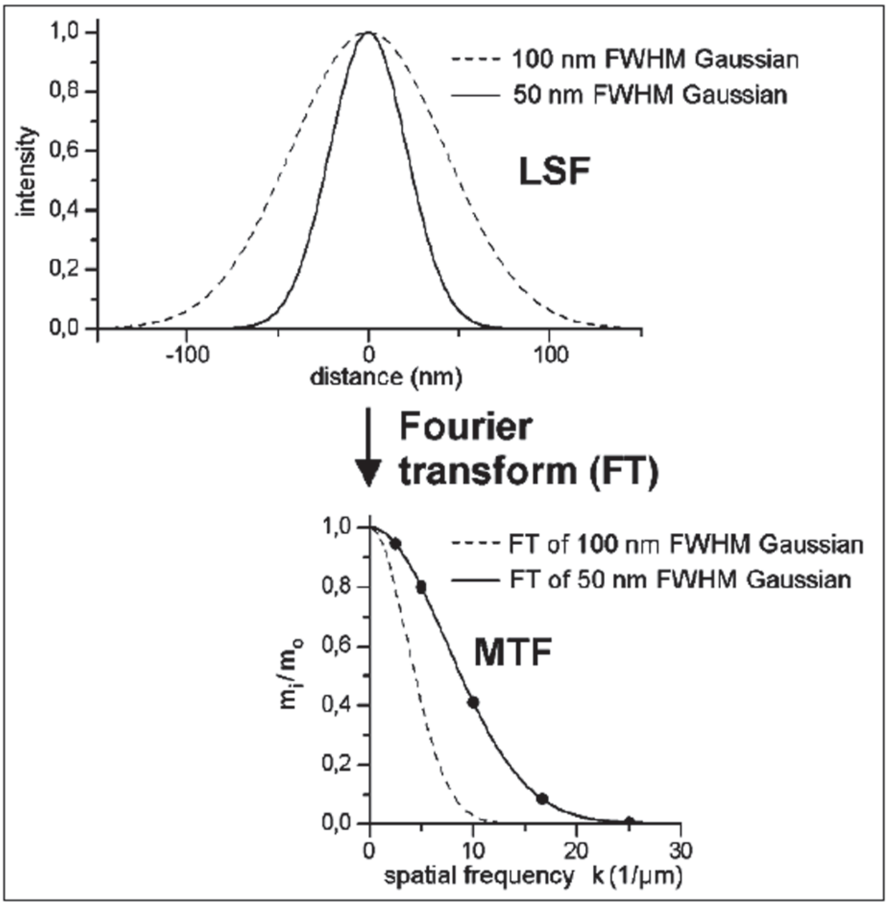

Figure 7 — Calculation of the modulation transfer function (MTF) by Fourier transform of the line spread function (LSF). The black dots are m_i / m_o values taken from Figure 6

4.1.5 The contrast transfer function (CTF)

Optimal samples for a determination of the lateral resolution of beam-based imaging methods of surface analysis have a flat surface and a high material contrast. In the sub-100 nm range, this requirement is fulfilled by square-wave gratings, whereas flat sine-wave gratings are not available. Furthermore, the sharp contrast at the edges of a square-wave grating enables the determination of the LSF and ESF. For this reason we describe the determination of lateral resolution (cf. 4.4) using this kind of grating.

In analogy to the modulation m of sine-wave gratings the contrast of square-wave gratings is defined by $c = (I_{\max} - I_{\min})/(I_{\max} + I_{\min})$. The variation of contrast with spatial frequency is described by the contrast transfer function

$$\mathrm{CTF}\ (\mathrm{k}) = c_i/c_o \tag{11}$$

where c_i and c_o are the contrast of image and object pattern, respectively (cf. terms and definitions). In Figure 8 simulation results of the imaging of square-wave gratings and sine-wave gratings are displayed for high and medium resolution and at the limit of resolution as well. The imaging system is represented here by a Gaussian LSF with 50 nm FWHM. In all cases the contrast c_i in the image of a square-wave grating is higher than the modulation m_i in the image of the sine-wave grating. If the grating period is large compared to the FWHM of the imaging system's LSF (300 nm period grating), the intensity in the image of the square-wave grating drops to zero between the strips of the grating providing $c_i = 1$, whereas this is principally not the case for the sine-wave grating. A plateau of the CTF ($c_i/c_o = 1$) at low spatial frequencies for square-wave gratings appears accordingly. Imaging of sine-wave gratings yields for a Gaussian LSF a Gaussian MTF (cf. Figures 7 and 9).

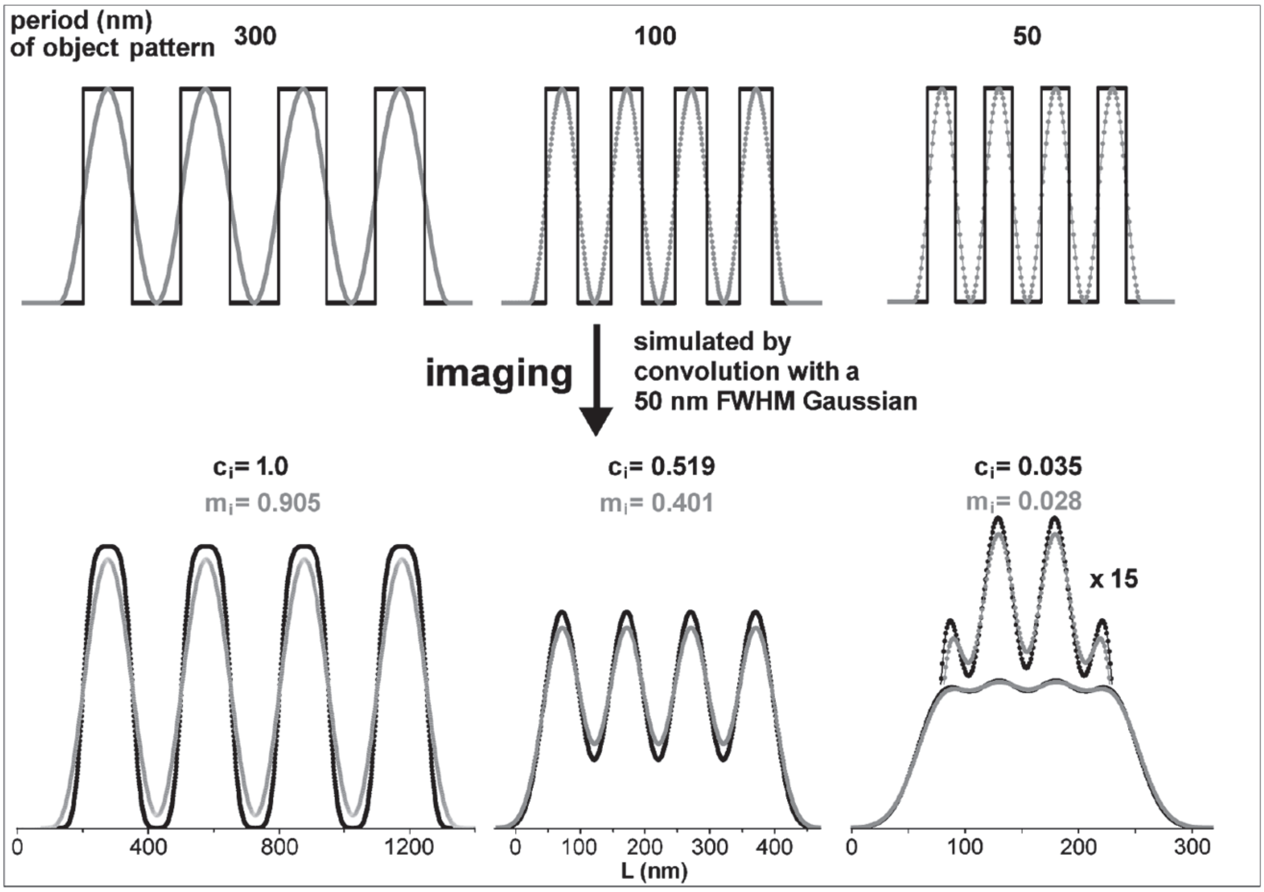

Figure 8 — Imaging of square-wave gratings (black lines) and sine-wave gratings (grey lines) of different periods. c_i and m_i are contrast and modulation in the image of a square-wave and sine-wave grating, respectively. Note the different length scales

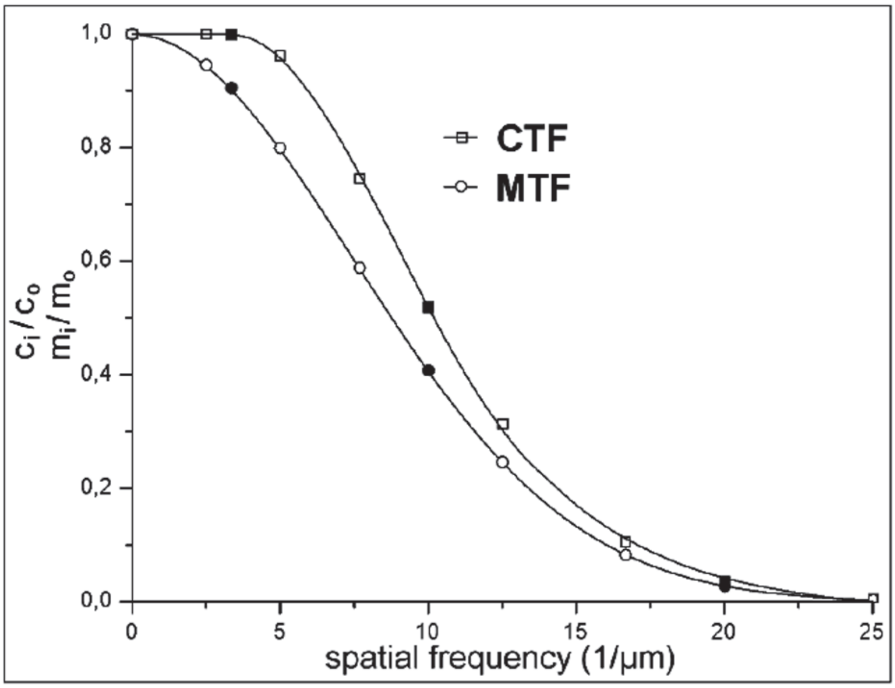

Figure 9 — CTF and MTF determined from images of square-wave gratings and sine-wave gratings, respectively. The imaging system is characterized by a 50 nm FWHM Gaussian LSF. The black symbols correspond to values taken from images displayed in Figure 8

4.1.6 Classical resolution criteria

The most commonly used resolution criterion in microscopy is the Rayleigh criterion: “Two point sources are just resolved if the central maximum of the intensity diffraction pattern produced by one point source coincides with the first zero of the intensity diffraction pattern produced by the other”[2]. It is an empirical estimate of resolution and corresponds to a decrease of intensity (dip) of 19 % (rectangular aperture) or 26.4 % (radial aperture) from the intensity of the two maxima. The threshold of resolution defined by the Rayleigh criterion reflects rather the performance of visual inspection than the sensitivity of modern instruments with sophisticated detectors. Because the Rayleigh criterion needs a rather clear separation of features (expressed by the depth of the dip), it leads to a resolution which is worse in comparison to resolutions obtained by more appropriate criteria.

The Sparrow criterion[7] defines the lowest resolution threshold that is possible in principle: the appearance of a dip between two maxima of signal intensity. In practical imaging noise prevents the detection of a very small dip between two maxima. As a consequence the resolution determined according to the Sparrow criterion is unrealistically high. Three grating profiles are resolved in Figure 10 according to the Sparrow criterion and only one grating profile is resolved according to the Rayleigh criterion.

The Rayleigh criterion, the Sparrow criterion and other so-called classical resolution criteria[11] are related to the pointspread function of the imaging instrument and do not take into account measurement conditions such as noise and sampling step width. All classical criteria do not cover object contrast issues. Therefore they give rather a theoretical limit of resolution and their application in imaging surface analysis is not straightforward. The application of the Rayleigh criterion and the Sparrow criterion in surface analysis has been discussed in Ref. [12] but they do not play a role in practical surface analysis.

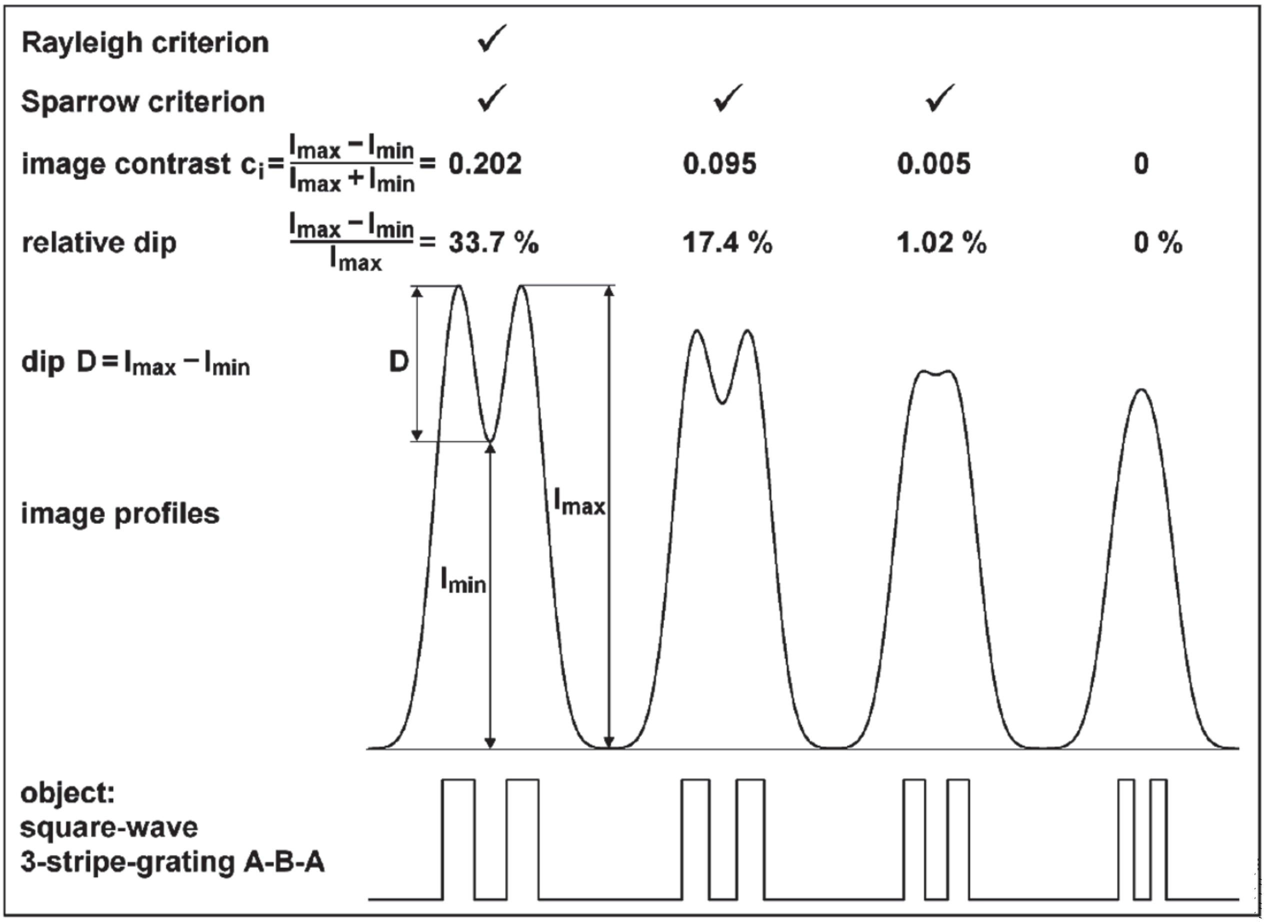

Figure 10 — Application of the Rayleigh criterion and the Sparrow criterion to simulated image profiles over square-wave gratings with different periods

4.1.7 Comparison of functions, parameters and methods related to effective lateral resolution and sharpness

See Tables 1, 2 and 3.

Table 1 — Summary of essential results of the methods related to effective lateral resolution

Feature or function	Method of determination	Relation to effective lateral resolution	Advantages	Disadvantages	Subclause
Effective lateral resolution, r_e	Visual determination of r_e from an image of a series of square-wave gratings	Period of the finest resolved grating corresponds to r_e	Real time procedure without any data treatment	Subjective decision whether a grating is resolved or not Large uncertainty of r_e at large values of the grading factor q	4.4.2 4.4.4
Effective lateral resolution, r_e	Determination of dip-to-reduced-noise ratios $R_{\mathrm{D/RN}}$ from a linescan over three square-wave gratings, calculation of r_e from the intersection of $R_{\mathrm{D/RN}}$ (P) with $R_{\mathrm{D/RN}} = 4$ according to Formula (39)	Calculated value of r_e is based on the resolution criterion (37)	Criterion-based calculation of r_e High accuracy of r_e also at large values of the grading factor ($q \leq 1.8$)	Numerical evaluation of noise and dips from a linescan over three gratings	4.4.2 4.4.4
Effective cut-off frequency of the CTF	Determination of the intersection between CTF and $(c_{\mathrm{i}} / c_{\mathrm{o}})_{\mathrm{ThR}}$	r_e corresponds to the reciprocal of the effective cut-off frequency of the CTF	Criterion based method for the determination of r_e	Time-consuming evaluation of noise and dips from a linescan over a series of gratings	4.4.3.3

Table 2 — Summary of essential results of the methods related to sharpness

Feature or function	Method of determination	Relation to sharpness	Advantages	Disadvantages	Sublause
CTF (contrast transfer function)	Linescan over a series of square-wave gratings, image contrast as function of spatial frequency	Describes sharpness over the whole range of spatial frequencies	Response of an imaging system over the whole range of spatial frequencies	Time-consuming numerical evaluation of noise and dips from a linescan over a series of gratings	4.1.5 4.4.3
LSF (line spread function)	Linescan over a narrow stripe	LSF describes the sharpness of an image	Simple procedure of measurement		4.1.2 4.2.1–4.2.5
FWHM of LSF, w_{LSF}	Linescan over a narrow stripe, determination of FWHM	Measure of sharpness of an image	Simple procedure	Shape of the LSF is not considered	4.2.1–4.2.5
MTF (modulation transfer function)	LSF from linescan over a narrow stripe MTF by Fourier transform of LSF	Describes sharpness over the whole range of spatial frequencies	Response of an imaging system over the whole range of spatial frequencies	Tails of LSF have to be measured with high accuracy Noise affects the spectrum of spatial frequencies	4.1.4 4.2.6
ESF (edge spread function)	Linescan over a straight edge (step transition) covering the 0% and 100% levels of signal intensity	ESF describes the sharpness of an image	Simple procedure	For long-tailed LSFs the 0% and 100% levels of ESF may be not covered by measurement	4.1.3 4.3
$D_{12–88}$, $D_{16\text{-}84}$, $D_{20–80}$ ESF rise parameters	Linescan over a straight edge (step transition) covering the 0% and 100% levels of signal intensity	Measure of sharpness of an image	Simple procedure	0% and 100% levels of ESF may be not covered by measurement, then $D_{\mathrm{x}\text{-}(1\text{-}\mathrm{x})}$ may be underestimated	4.1.3 4.3

Table 3 — Requirements for test samples

Feature	Method of determination	Type of sample	Required sample properties	Subclause
Effective lateral resolution r_e	Visual determination of r_e from an image of a series of square-wave gratings	Series of chemical square-wave gratings A–B–A (materials A and B) with graded grating periods P	Grading factor $q = P_{n+1}/P_n$ of grating periods P: Optimum: $1.2 \leq q \leq 1.5$ Calculation according to Formula (39): $q \leq 1.7$ Optimum distance d_{gr} between two consecutive gratings: General: $1.5\,P \leq d_{gr} \leq 3\,P$ Gaussian LSF: $P \leq d_{gr} \leq 2\,P$ Expanded (k=2) uncertainty of certified grating periods: $U(P) \leq 10\ \%$	4.4.1.1 4.4.1.2 4.4.4
	Calculation of r_e from the intersection of $R_{D/RN}(P)$ with $R_{D/RN} = 4$ according to Formula (39)			
	Determination of r_e as the reciprocal of the effective cut-off frequency of the CTF			
Line spread function, LSF FWHM of the LSF, w_{LSF} Modulation transfer function, MTF	Linescan over a narrow stripe	Narrow stripe	Stripe width w_s to ensure $\Delta w_{LSF} < 10\ \%$: Gaussian LSF: $w_s \leq 0.6\,w_{LSF}$ Lorentzian LSF: $w_s \leq 0.4\,w_{LSF}$ Stripe distance d to ensure $\Delta w_{LSF} < 6\ \%$: Gaussian LSF: $d \geq 2.5\,w_{LSF}$ Lorentzian LSF: $d \geq 5\,w_{LSF}$	4.2.2 4.2.7
Edge spread function ESF ESF rise parameters D_{12-88}, D_{1684}, D_{20-80}	Linescan over a straight edge (step transition) covering the 0% and 100% levels of signal intensity	Chemical edge: material A–material B with extended lower (A) and upper (B) plateaus Spatial edge: vacuum–material A	Plateau lengths L_{pl} to ensure $\Delta D_{x-(1-x)} < 10\ \%$: Gaussian LSF: $L_{pl} \geq 2\,w_{LSF}$ Lorentzian LSF: $L_{pl} \geq 40\,w_{LSF}$	4.3.3 4.3.5

4.2 Determination of the line spread function and the modulation transfer function by imaging of a narrow stripe

The line spread function (LSF) (cf. 4.1.2) determined by imaging a narrow stripe (defined in 4.2.2) may be used to characterize the quality of an image and the performance of an imaging instrument[13] because its width w_{LSF} and shape substantially determine the lateral resolution of the image (cf. 4.4.3.1). w_{LSF} is related to lateral resolution but in general it is not the lateral resolution. Its value may differ substantially from the lateral resolution (cf. 4.4.3.3). The LSF may be obtained directly from the measured profile over a narrow stripe or by fitting the measured profile with a model function as outlined in 4.2.3.

4.2.1 Model functions for the LSF

The transverse intensity distribution in light and particle beams can be described by different model functions.[14] The most frequently used function is the two-dimensional Gaussian function. According to Formula (4) and Figure 3 (cf. 4.1.2) the LSF is also a Gaussian function (normal distribution) for these probe beams

$$\mathrm{G}(x) = y_0 + \frac{I_0}{\sigma\sqrt{2\pi}} \exp\left(-(x - x_0)^2 / 2\sigma^2\right) \tag{12}$$

where σ is the standard deviation of the normal distribution, x_0 is the centre position, y_0 is the background intensity and I_0 is the total intensity expressed as the area under the curve. The full width at half maximum (FWHM) of G(x) is

$$w = [2\ln(2)]^{½} \times 2\sigma = 1.1774 \times 2\sigma \tag{13}$$

The Gaussian function describes the intensity distribution within a beam which is formed by an ideal lens system. However, in reality the LSF may deviate from Gaussian shape. Therefore other model functions are considered, too. One option is a combination of Gaussian functions with different widths (cf. 5.2.2 and[14-16]) as shown in Figure 11.

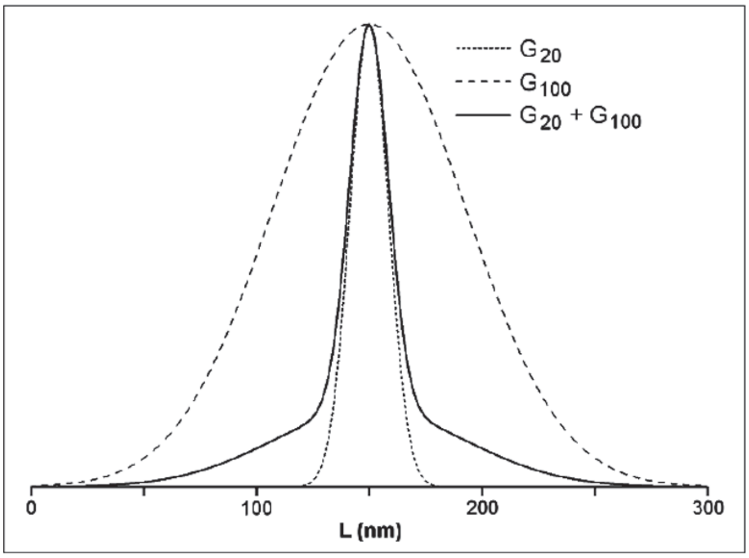

Figure 11 — Two Gaussian functions G with different widths and the sum of these functions. The functions are normalized to the same height. FWHM values in nm are given as indices

The Lorentzian function L(*x*) is well known in spectroscopy, because it is the resonance function of the harmonic oscillator and fits the shape of spectral lines of atoms. It can be used also for fitting LSFs with extended tails (Figure 12), which may occur due to lens aberration[17] and/or particle scattering within the sample. It is defined by

$$\mathrm{L}(x) = y_0 + \frac{2 \times I_0 \times w}{\pi[4(x - x_0)^2 + w^2]} \tag{14}$$

where w is the FWHM of the function, x_0 is the centre position, y_0 is the background intensity and I_0 is the total intensity (area under the curve).

The Pseudo-Voigt function is a weighted sum of Gaussian and Lorentzian functions. The type 1 Pseudo-Voigt function (cf. Figure 12) is a linear combination of a Lorentzian function and a Gaussian function with the same FWHM denoted by *w* and weighted by a factor *η*:

$$\mathrm{PSV1} = y_0 + I_0\left[\eta \mathrm{L}\left(x, x_0, w\right) + \left(1 - \eta\right) \mathrm{G}\left(x, x_0, w\right)\right] \tag{15}$$

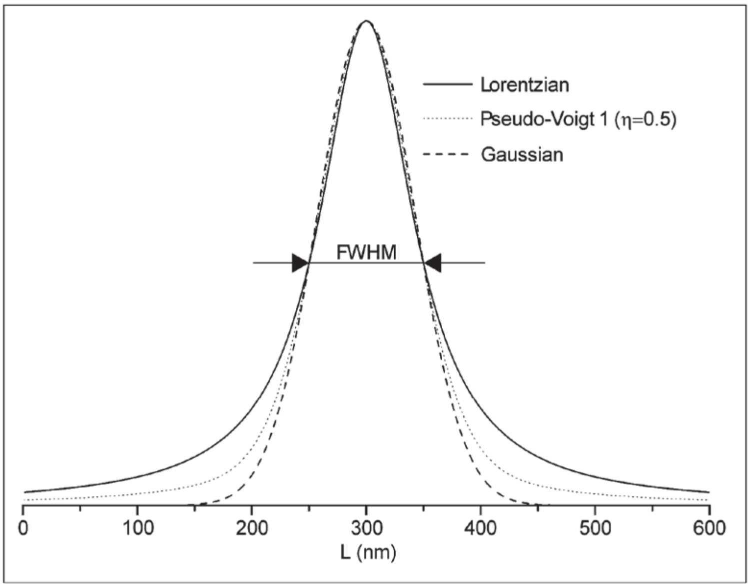

Figure 12 — Gaussian function, Lorentzian function and type 1 Pseudo-Voigt function having the same FWHM of 100 nm. The functions are normalized to the same height

The type 2 Pseudo-Voigt function is a linear combination of a Lorentzian function and a Gaussian function with different widths $\mathrm{w_L}$ and $\mathrm{w_G}$:

$$\mathrm{PSV2} = y_0 + I_0\left[\eta \mathrm{L}\left(x, x_0, w_{\mathrm{L}}\right) + \left(1 - \eta\right) \mathrm{G}\left(x, x_0, w_{\mathrm{G}}\right)\right] \tag{16}$$

A great variety of LSF shapes (Figure 13) can be simulated by a type 2 Pseudo-Voigt function.

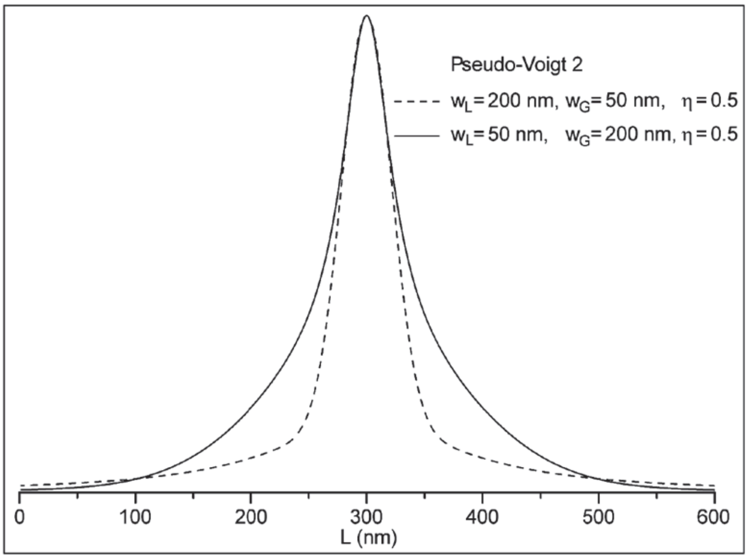

Figure 13 — Type 2 Pseudo-Voigt functions with different combinations of w_L and w_G. The functions are normalized to the same height

4.2.2 What is a narrow stripe?

A stripe may be called narrow if its width w_S is small compared to the full width at half maximum of the LSF w_{LSF} characterizing the imaging system used. In this case a profile across the image of the stripe reveals that LSF. If w_S is not small compared to w_{LSF}, then the FWHM of the image profile increases with increasing width of the stripe. This effect is demonstrated by a simulation displayed in Figure 14, where stripe images are simulated by convolution with a Gaussian LSF.

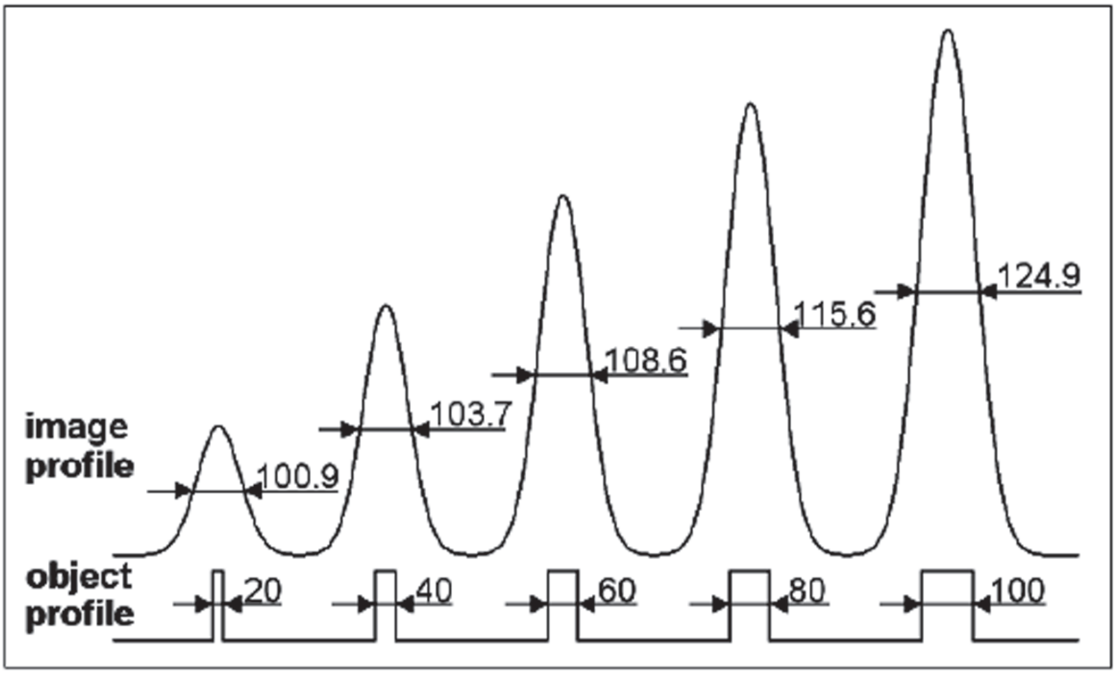

Figure 14 — Imaging of a series of stripes simulated by convolution with a Gaussian LSF with w_{LSF} = 100 nm. The values given in the image profiles are the FWHM in nm

The deviation of w_{LSF} taken from the image profile from the true value of $FWHM_{LSF}$ is displayed as a function of w_s/w_{LSF} in Figure 15.

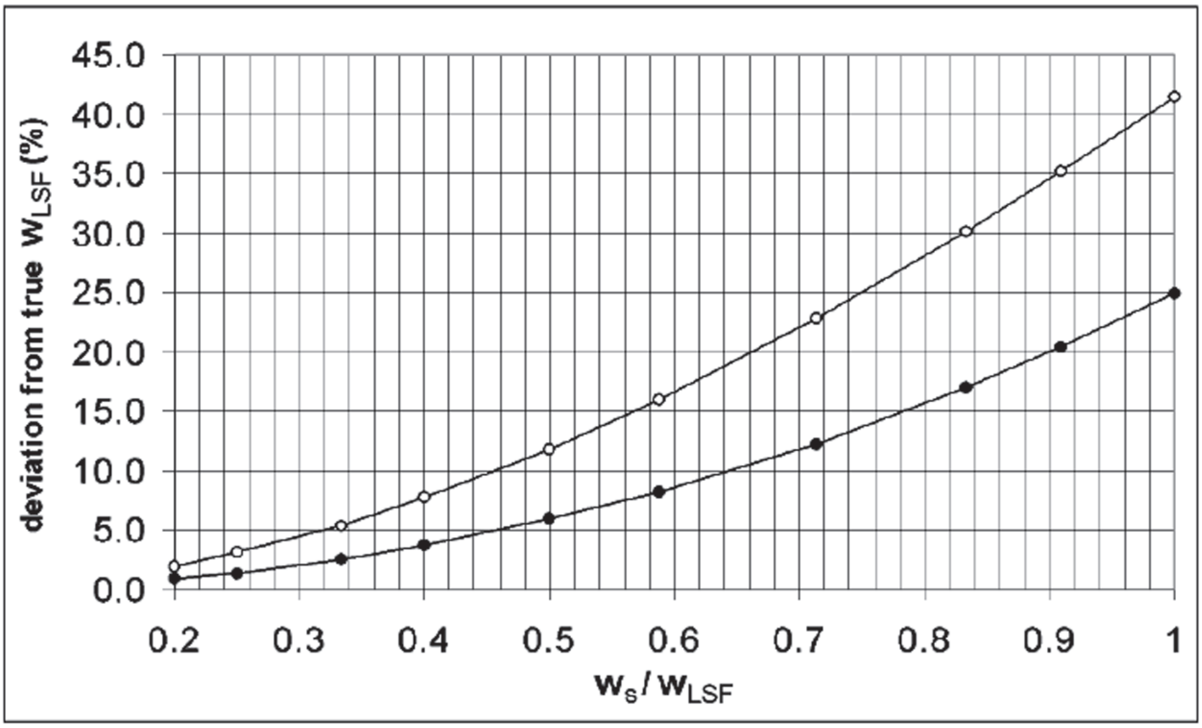

Figure 15 — Deviation of the FWHM of the profile of an imaged stripe from w_{LSF} as function of the ratio w_s/w_{LSF}. Black dots: Gaussian LSF; Open circles: Lorentzian LSF

The shape of the image profile is also influenced by the stripe width w_s. For small values of the ratio w_s/w_{LSF}, e.g. 0.2 as displayed by the left image profile in Figure 14, the image profile may be fitted by the LSF shape function with a slightly increased FWHM. For $w_s/w_{LSF} = 1$ as displayed by the right image profile in Figure 14, the shape of the image profiles differs from that of the LSF. Figure 16 shows the best fits of image profiles for the $w_s/w_{LSF} = 1$ case. The image profile created with a Gaussian LSF shows only a small deviation from Gaussian shape, whereas the profile created with a Lorentzian LSF deviates considerably from Lorentzian shape.

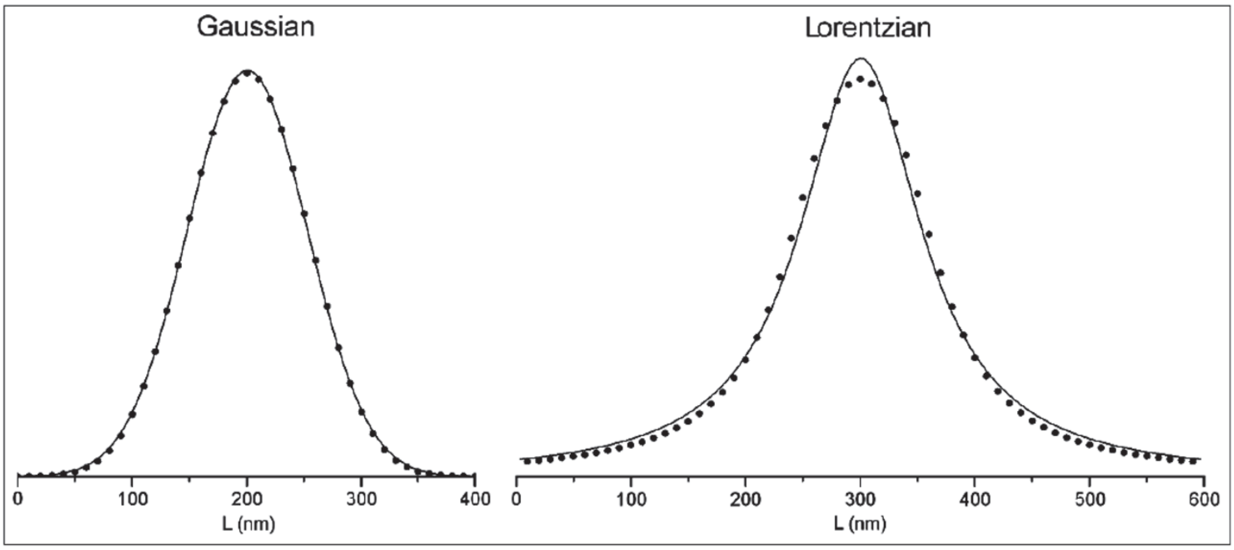

Figure 16 — Image profiles (black dots) over a 100 nm wide rectangular stripe simulated by convolution with 100 nm wide Gaussian and Lorentzian LSFs revealing the deviations from the principal shape of the LSF. Lines show the best fit with a Gaussian and Lorentzian, respectively

4.2.3 The effect of signal-to-noise ratio and sampling step width on LSF determination

For sufficiently high signal-to-noise ratios $R_{S/N}$ the LSF and its full width at half maximum w_{LSF} can be obtained directly from the measured profile over a narrow stripe. This simple situation is displayed in Figure 17, left panel, top. However, experimental data can be also analysed by fitting with more or less appropriate LSF model functions (Figure 17, left panel, middle and bottom).

The low $R_{S/N}$ case is given in Figure 17, right panel. Here shape and w_{LSF} have to be determined by fitting experimental data with a peak shape model function. Depending on the model function, the w_{LSF} can be taken either directly from the respective fit parameter results (Figure 17, middle row) or from the fitted curve (Figure 17, lower row). In any case the background signal y_0 must be determined carefully outside the stripe profile.

The profiles given in Figure 17 were created by the convolution of a narrow stripe with a type 2 Pseudo-Voigt function. Indeed, for the high $R_{S/N}$ case a fit with that type of function yields a better result (smaller χ^2) than a fit with a Lorentzian. In the low $R_{S/N}$ case the values of χ^2 are very similar for both functions but a fit with a Lorentzian yields a smaller deviation of w_{LSF} from the value of the implemented type 2 Pseudo-Voigt model function. The latter result is accidental and caused by noise which has broadened the stripe profile.

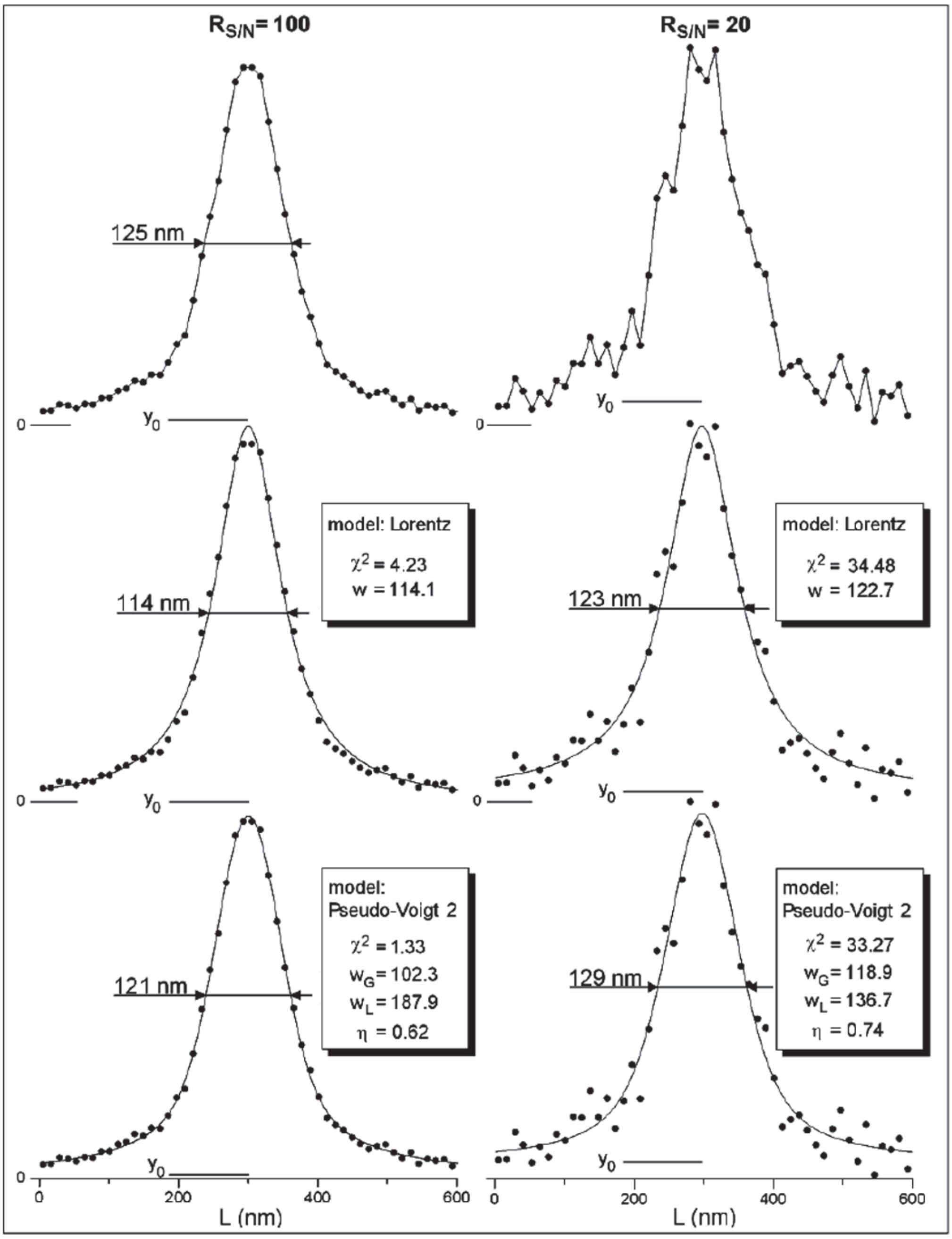

Figure 17 — Determination of w_{LSF} from a simulated image profile of a narrow stripe at different $R_{S/N}$ levels ($R_{S/N}$ = I_{max} /σ_N , where σ_N is the standard deviation of noise). Data points (black dots) represent a measured profile simulated by convolution of a 20 nm wide stripe with a type 2 Pseudo-Voigt function (PSV2, w_G = 100 nm, w_L = 200 nm, η = 0.6, cf. 4.2.1) and subsequent addition of two different noise levels. The FWHM of the PSV2 function is 118.4 nm, the FWHM of the convolution without noise is 119.7 nm. Upper row: raw data; Middle row: Profiles fitted with a Lorentzian; Lower row: Profiles fitted with a PSV2 function. y_0 is the background signal and χ^2 is a measure of the quality of the fit

The quality of the determination of the LSF and its width w_{LSF} depends on the sampling step width used for the measurement of the profile. Especially but not only at low signal-to-noise ratios $R_{S/N}$, the uncertainty of w_{LSF} increases with decreasing number of sampling points, i.e. increasing sampling step width. This effect is demonstrated by fitting LSFs for simulated image profile data at different $R_{S/N}$ levels. The random nature of noise was taken into account in this simulation by adding different sets of Gaussian noise to a Gaussian profile with w_{LSF} = 30 nm representing the image profile. To establish data sets with different sampling step widths the number of data points was reduced simply by removing data points.

All w_{LSF} values obtained by fitting Gaussian profiles with different sets of Gaussian noise ($R_{S/N}$ = 10) and a variation of sampling step widths are summarized in Figure 18. Step width and number of sampling points, both normalized to w_{LSF} = 30 nm of the original noise-free Gaussian profile are given at the abscissa.

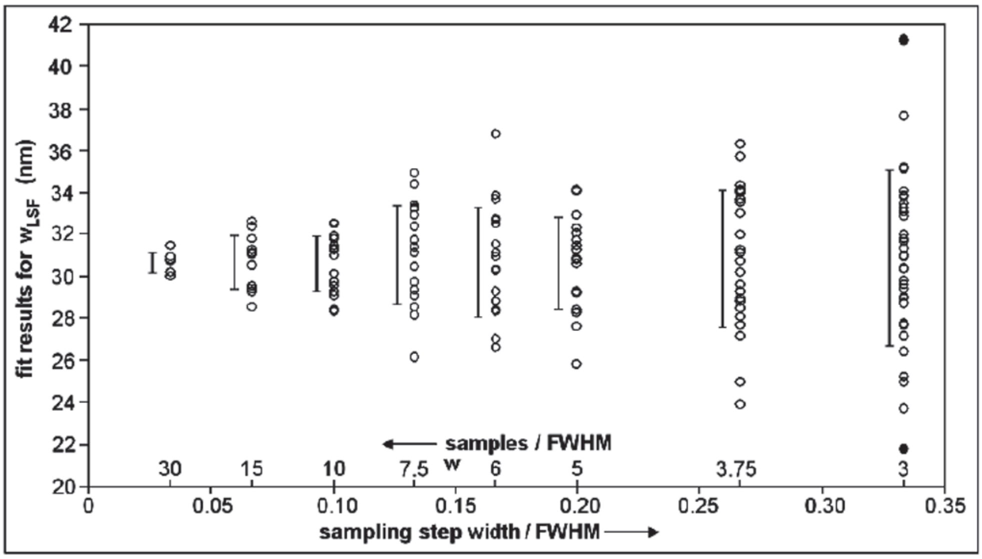

Figure 18 — Dispersion of w_{LSF} data determined for simulated Gaussian profiles at $R_{S/N}$ = 10 and different sampling step widths. The noise-free Gaussian profile has a FWHM of 30 nm. The bars denote the standard deviations. Both black dots at 3 samples/FWHM denote extreme values of w_{LSF} obtained from profiles which are displayed in the upper row of Figure 19

Figure 19 (top line) shows the largest positive and negative deviations, respectively, of fitted w_{LSF} data from the original FWHM = 30 nm noise-free Gaussian profile. Strong noise ($R_{S/N}$ = 10) and large step width (10 nm corresponding to only three data points per w_{LSF}) cause deviations up to 38 % in those cases.

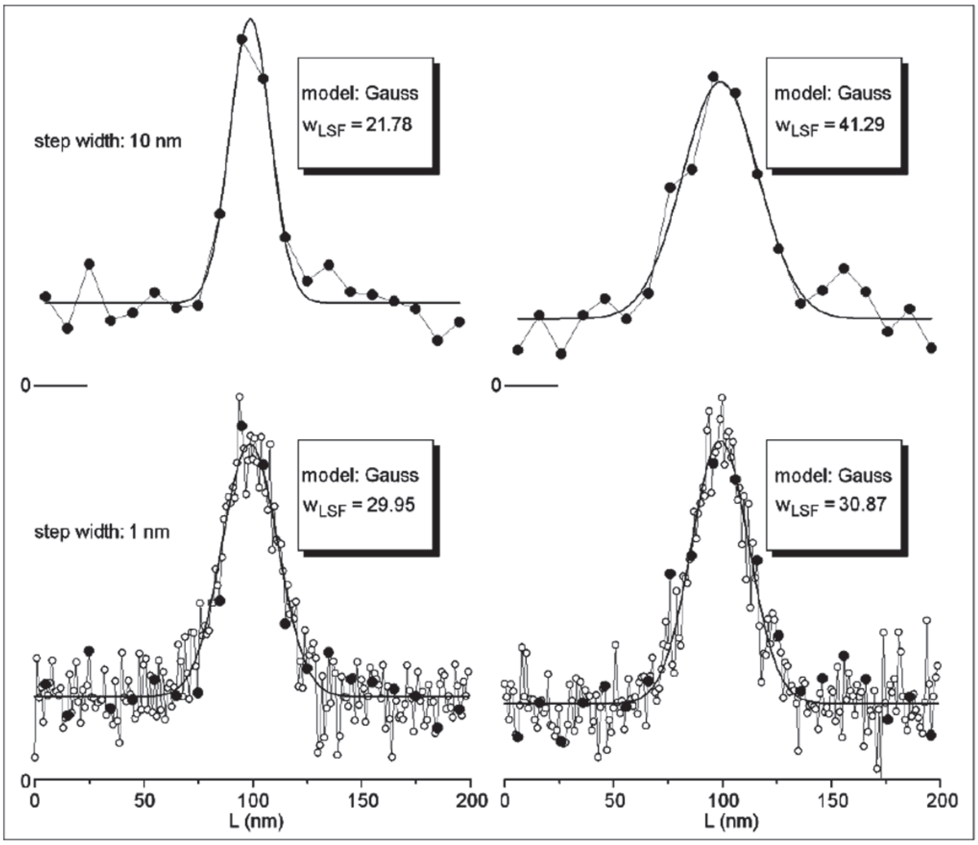

Figure 19 — Fits of Gaussian profiles (30 nm FWHM) superimposed by different sets of Gaussian noise providing $R_{S/N}$ = 10. Those profiles simulate an image profile across a narrow stripe at different step widths of sampling. Dots are data points (connected by a fine line). Fitted profiles are displayed by bold lines. w_{LSF} results are given in the boxes. Top: Narrowest and widest profile from 36 profiles at a sampling step width of 10 nm. Bottom: Profiles with a sampling step width of 1 nm which were created with the same sets of Gaussian noise as the profiles given in the upper row. The black dots denote the data points of the reduced data sets in the upper row

Figure 20 shows the largest deviations of w_{LSF} obtained from fitting of different profiles with different levels of noise and two sampling step widths. The variability of w_{LSF} data vs. sampling step width is much stronger for noisy profiles ($R_{S/N}$ = 10) than for those with medium ($R_{S/N}$ = 30) or low ($R_{S/N}$ = 100) levels of noise.

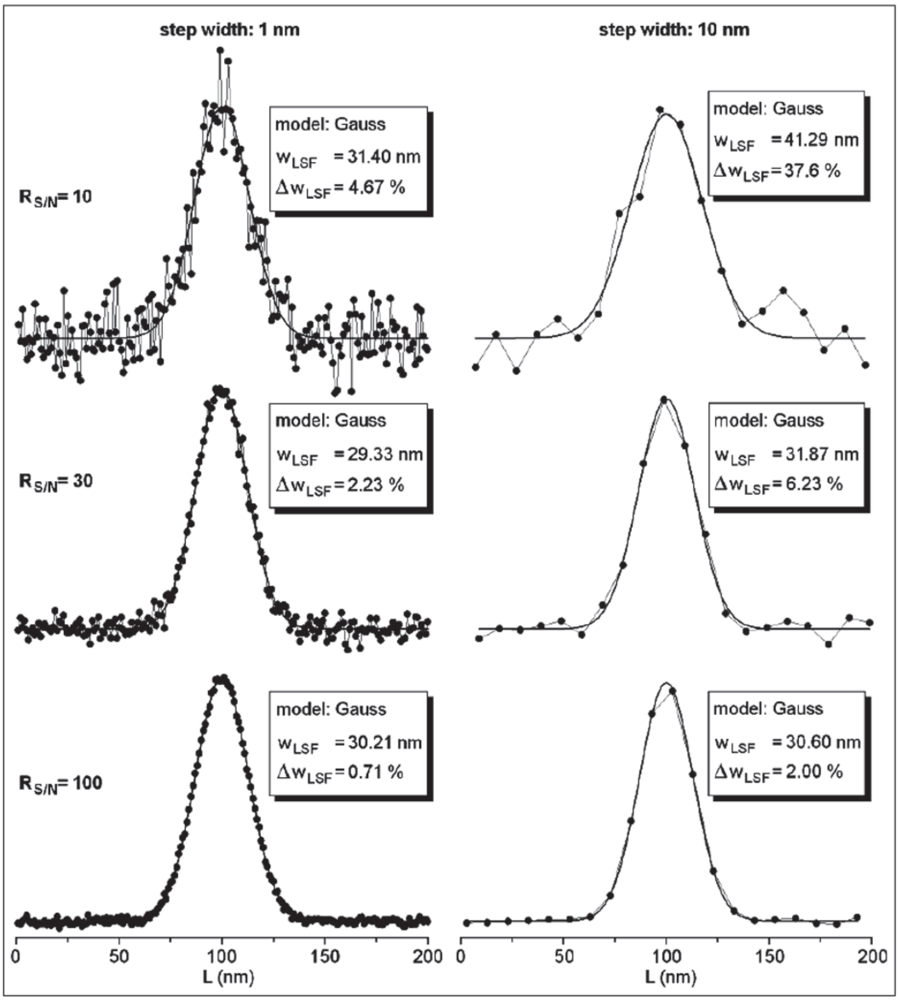

Figure 20 — Largest positive or negative deviations of fitted w_{LSF} from the FWHM of the original noise-free profile (30 nm) for different sampling step widths and $R_{\text{S/N}}$ levels

The accuracy of w_{LSF} determined by fitting of noisy stripe profiles depends on $R_{\text{S/N}}$ as well as sampling step width. As a measure of accuracy of the fitting procedure a mean deviation

$$s=\sqrt{\frac{1}{(n-1)}\sum_{i=1}^{n}\left[\left(w_{\text{LSF}}\right)_i-\left(w_{\text{LSF}}\right)_t\right]^2} \tag{17}$$

was calculated, where $(w_{\text{LSF}})_\text{i}$ is one of n results of the fitting procedure and $(w_{\text{LSF}})_\text{t}$ is the true FWHM of the noise-free Gaussian profile. The deviation s is a little different from the standard deviation given by bars in Figure 18 because the fitting results were related to the true value of $(w_{\text{LSF}})_\text{t}$ and not to the arithmetic mean of w_{LSF}. As a result s includes, besides the statistical error, also possible systematic deviations of the fitting procedure. Therefore it is a measure of precision and trueness of the fitting procedure. Figure 21 shows the relative deviation $\text{s}/(w_{\text{LSF}})_\text{t}$.

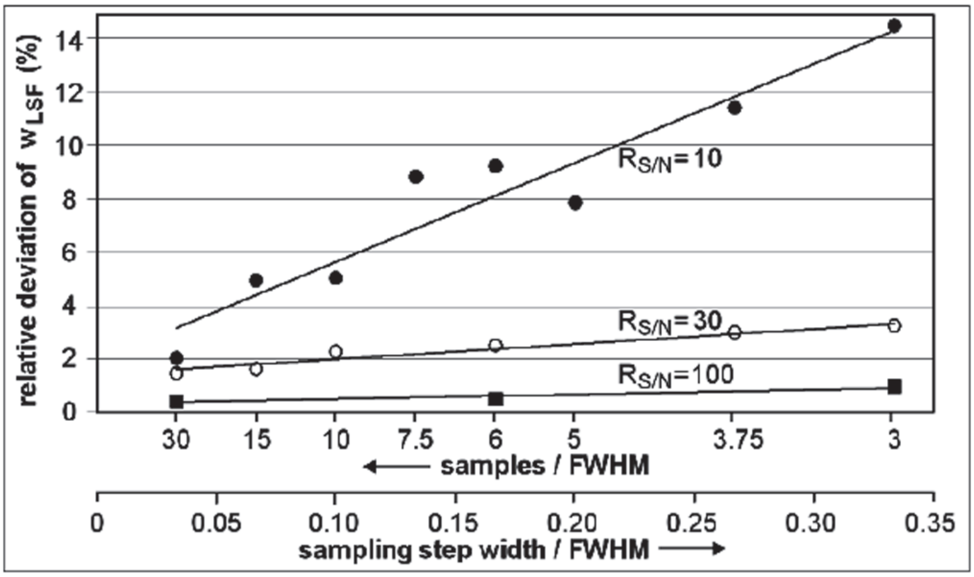

Figure 21 — Relative deviation $s \bullet 100/(w_{LSF})_t$ of fitted w_{LSF} data as a function of sampling step width for different values of $R_{S/N}$. The values for $R_{S/N} = 10$ are calculated from the values shown in Figure 18

4.2.4 The effect of smoothing on LSF determination from a noisy image profile

For low $R_{S/N}$ levels, the LSF and its width w_{LSF} cannot be taken directly from the measured profile over a narrow stripe (cf. 4.2.3). In many cases smoothing may be attractive to enable the simple direct approach of LSF and w_{LSF} determination. When the measured profile over the narrow stripe is formed by a sufficient number of sampling points different kinds of smoothing procedures may be applied. The application of such smoothing procedures has been discussed in detail with respect to spectroscopic data[18]–[20].

Figure 22 displays a noisy profile and its smoothing by three different methods which are implemented in the ORIGIN™ software.[21] An important smoothing parameter is the smoothing interval which determines the number of data points considered at one step of the smoothing routine. With increasing smoothing intervals noise will be reduced more efficiently, but the profile becomes flattened and broadened. Therefore, it is necessary to find the optimum smoothing interval. Figure 22 shows, that adjacent averaging has the lowest suitability for smoothing noisy profiles of imaged narrow stripes, because it broadens the profile more than the other methods. Better results can be obtained by using Savitzky-Golay smoothing and fast Fourier transform (FFT) filter smoothing. Results optimized in terms of smoothing intervals are displayed in Figure 23. w_{LSF} values obtained directly from the smoothed data points and those determined from a fit of the smoothed profile differ by less than 5 % from the value determined from a fit of the unsmoothed profile.

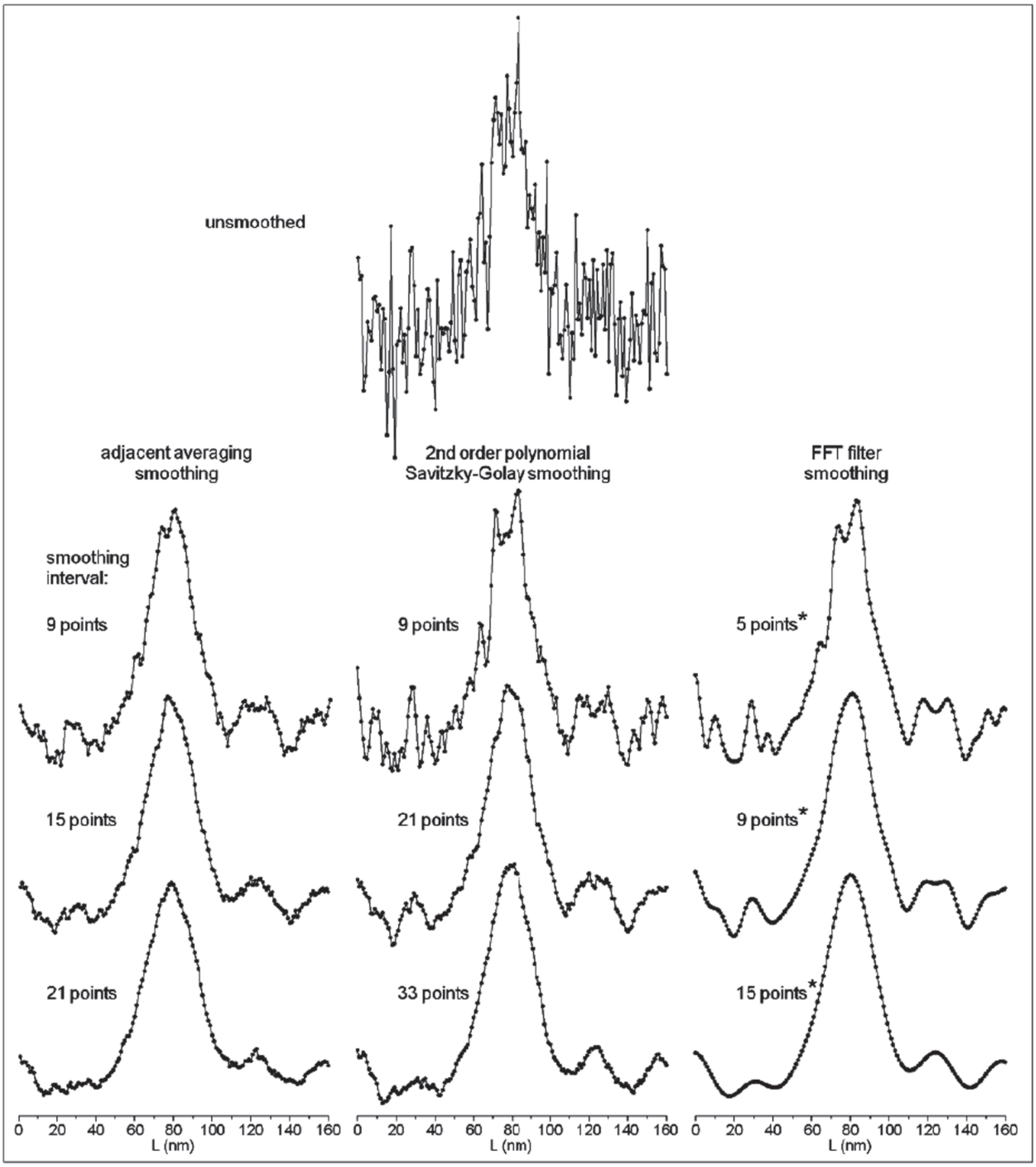

Figure 22 — Application of different smoothing procedures to a noisy ($R_{\mathrm{S/N}}$ = 5) profile. The profile was created by adding Gaussian noise to a Gaussian profile with FWHM = 30 nm and 1 nm sampling step width. *The number of points n in FFT filter smoothing is not comparable with the number of points for the other methods.

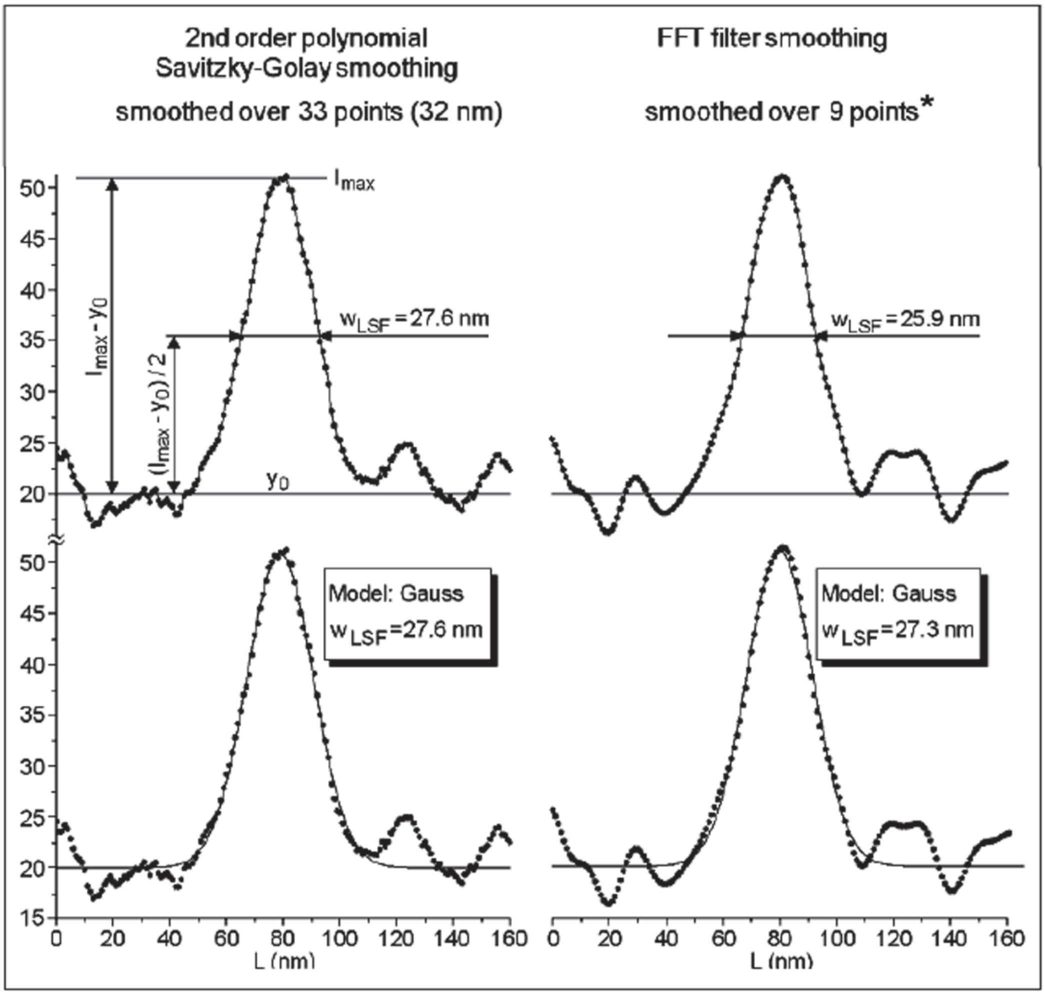

Figure 23 — Best smoothing results for a noisy ($R_{S/N}$ = 5) profile created by adding Gaussian noise to a Gaussian profile with FWHM = 30 nm and 1 nm sampling step width (cf. also Figure 22). Upper row: w_{LSF} directly taken from the smoothed profile. Lower row: Smoothed profile fitted with a Gaussian, with the w_{LSF} taken from the fit. A fit of the unsmoothed profile (not shown) gives a w_{LSF} of 26.4 nm. *The given number of points n in FFT filter smoothing is not comparable with the number of points for Savitzky-Golay smoothing

After smoothing with larger intervals of data the profiles become broadened and w_{LSF} data deviate too much from the w_{LSF} of the original profile to be acceptable. Figure 24 shows this effect for all three smoothing routines demonstrated in Figure 22 for one selected noise level ($R_{S/N}$ = 5). Here data are plotted vs. smoothing intervals normalized to the w_{LSF} of the original profile. Of course, the deviation of w_{LSF} depends also on $R_{S/N}$.

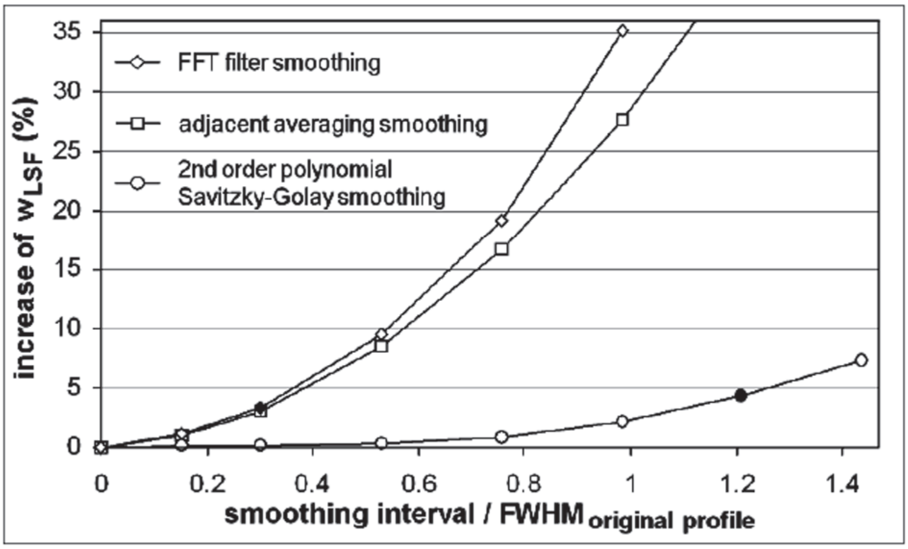

Figure 24 — Increase of w_{LSF} in dependence on the length of the smoothing interval. The values are taken from the example given in Figure 22 with $R_{\mathrm{S/N}} = 5$ and the black symbols denotes the two examples presented in Figure 23. The smoothing interval used in FFT filter smoothing is not comparable to the smoothing interval data for the other methods

Comparison of results of different smoothing routines reveals that, for 2nd order polynomial Savitzky-Golay smoothing, longer smoothing intervals can be used. The increase of obtained w_{LSF} values is smaller than for the other methods. For the given example, the increase of w_{LSF} in comparison to the FWHM of the original profile is about 2 % if the smoothing interval is equal to the FWHM of the original profile. This value and the particular suitability of Savitzky-Golay smoothing are in agreement with the results of Seah et al.[19][20]

4.2.5 Calculation of the MTF by Fourier transform of the LSF

There are principally two options for determining the MTF. One is based on imaging of sine-wave gratings. However, nanometre-scaled sine-wave gratings are not available. The alternative is the determination of the MTF by Fourier transform of the LSF (cf. 4.1.4). The LSF may be determined either by imaging a narrow stripe (cf. 4.2) or by differentiation of the edge spread function (ESF). The MTF is determined by the width (cf. Figure 7) and shape (cf. Figure 25) of the LSF.

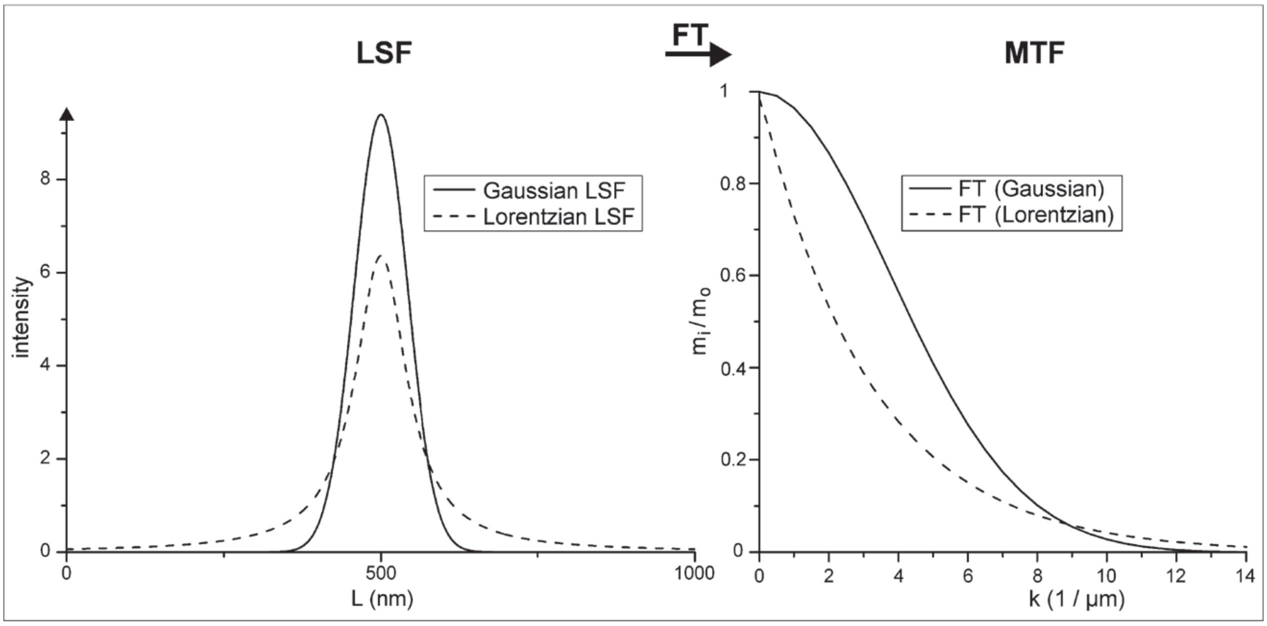

Figure 25 — Calculation of the MTF by Fourier transform (FT) of two LSF models. m_i and m_o are image and object modulations, respectively and k is the spatial frequency. The value of w_{LSF} is 100 nm both for the Gaussian and the Lorentzian LSF

The MTF is influenced by principal properties of the Fourier transform. The calculated MTF depends on the length range R_{LSF} where LSF data are used for the Fourier transform (shown in Figure 26). A short R_{LSF} cuts off the wings of the LSF [Figure 26 a)] and, as a consequence, the Fourier transform of the LSF deviates from the MTF calculated for a sufficiently long R_{LSF} [Figure 26 d)]. Furthermore, R_{LSF} determines the data distance D_{MTF} of the calculated MTF

$$D_{MTF} = 1/R_{LSF} \qquad (18)$$

If the measured length range M_{LSF} is limited by experimental conditions such as a noisy background signal or a superposition of signals from neighbouring patterns, the data distance D_{MTF} might be rather large [cf. Figure 26 a and d)]. To overcome this problem numerical extension of the length range R_{LSF} is helpful. The addition of “0”-values to the measured values expands R_{LSF} as shown in Figure 26 b) and reduces the data distance D_{MTF} [Figure 26 e)]. However, there will then be periodic structures in the MTF. The cut-off of the LSF wings corresponds to the application of a narrow slit and causes the well-known diffraction pattern. All of these problems are avoided when M_{LSF} does not fall below a certain minimum value. This minimum value depends on the width w_{LSF} and the shape of the LSF. Simulations revealed that, for a Gaussian LSF, M_{LSF} should be

$$M_{LSF} \geq 2.5\, w_G \qquad (19)$$

and for the long-tailed Lorentzian LSF

$$M_{LSF} \geq 5\, w_L \qquad (20)$$

where w_G and w_L are the FWHMs of the Gaussian and Lorentzian LSFs, respectively.

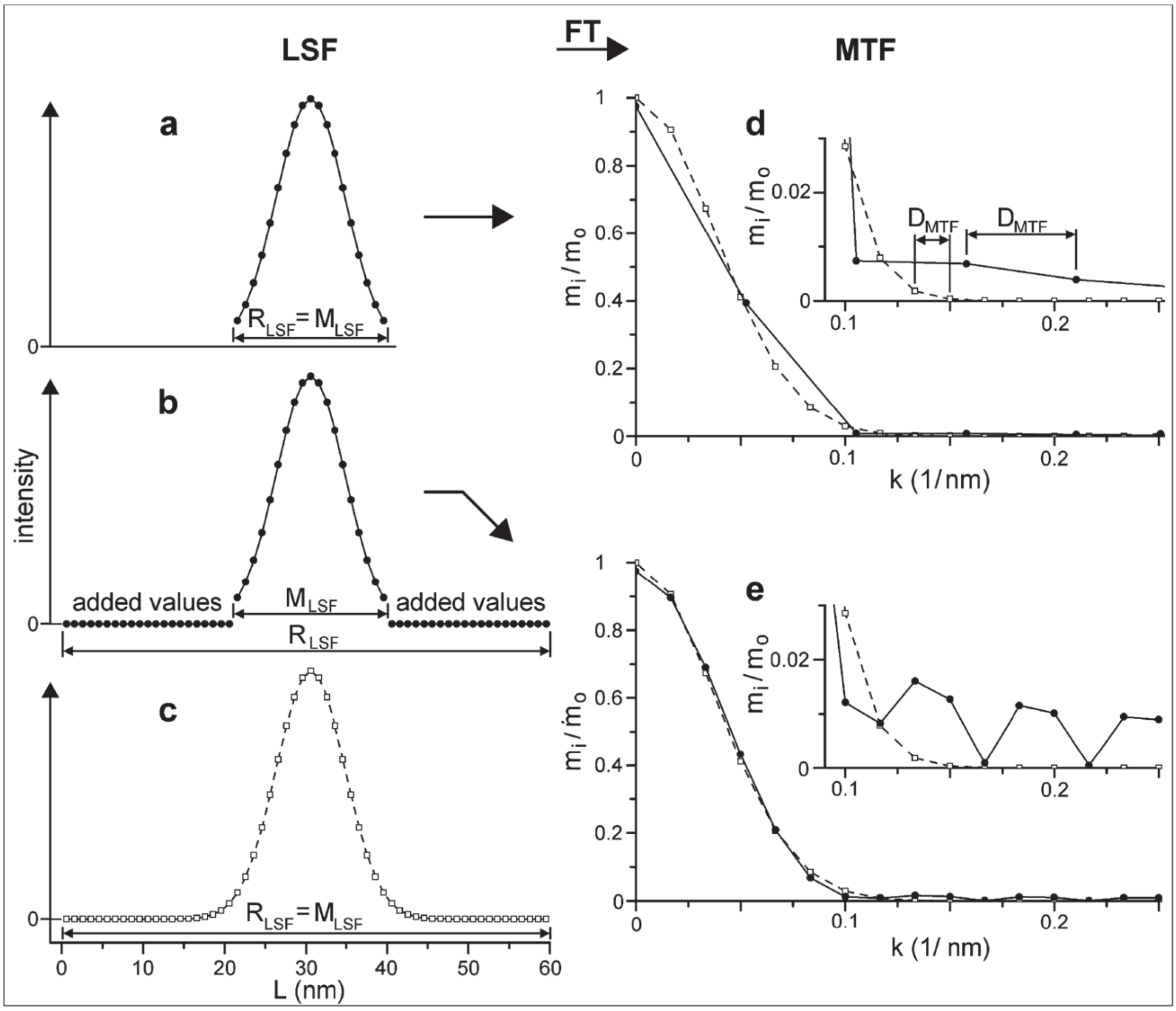

Figure 26 — The effect of length range R_{LSF} and measured length range M_{LSF} on the shape and data distance D_{MTF} of the MTF. The Gaussian LSF has a w_{LSF} value of 10 nm and a) $R_{LSF} = M_{LSF} = 19$ nm, b) $R_{LSF} = 60$ nm, $M_{LSF} = 19$ nm, and c) $R_{LSF} = M_{LSF} = 60$ nm. The MTF was calculated by Fourier transform (FT) of the LSF. The MTF calculated from case a) is given by black dots in d) and the MTF calculated from case b) is given by black dots in e). For comparison in d) and e) the MTF calculated from c) is given by open squares connected by a dashed line

Figure 27 shows that there is only a small difference in the high frequency range of the MTF between the case described by Formula (20) and the ideal case. The m_i / m_o value at $k = 0$ can be corrected to 1 because $k = 0$ corresponds to an infinite period of the sine-wave grating and therefore the complete object modulation is transferred to image modulation.

The maximum spatial frequency k_{max} of the MTF calculated by Fourier transform of the LSF is determined by the sampling step width S_w at which the LSF has been measured

$$k_{max} = 1/(2\,S_w) \tag{21}$$

where k_{max} is the upper interval limit of the highest calculated k value of the MTF (cf. Figure 27). A satisfying characterization of an imaging process requires a minimum range of spatial frequencies k for which the MTF is calculated. With Formula (21), a condition for the related sampling step width S_W is established which depends on the shape and width of the LSF. A Gaussian LSF requires

$$S_W \leq 0.4\, w_G \tag{22}$$

For a Lorentzian LSF, higher k-values of the MTF are of interest (cf. Figure 25) and correspondingly a smaller sampling step width S_W of the LSF is needed

$$S_W \leq 0.3 w_L \tag{23}$$

The calculation of the MTF for a Lorentzian LSF with a sampling step width of $0.3w_L$ is shown in Figure 27. The range of the MTF down to a value $m_i/m_o = 0.011$ is sufficient and confirms the limit given in Formula (23).

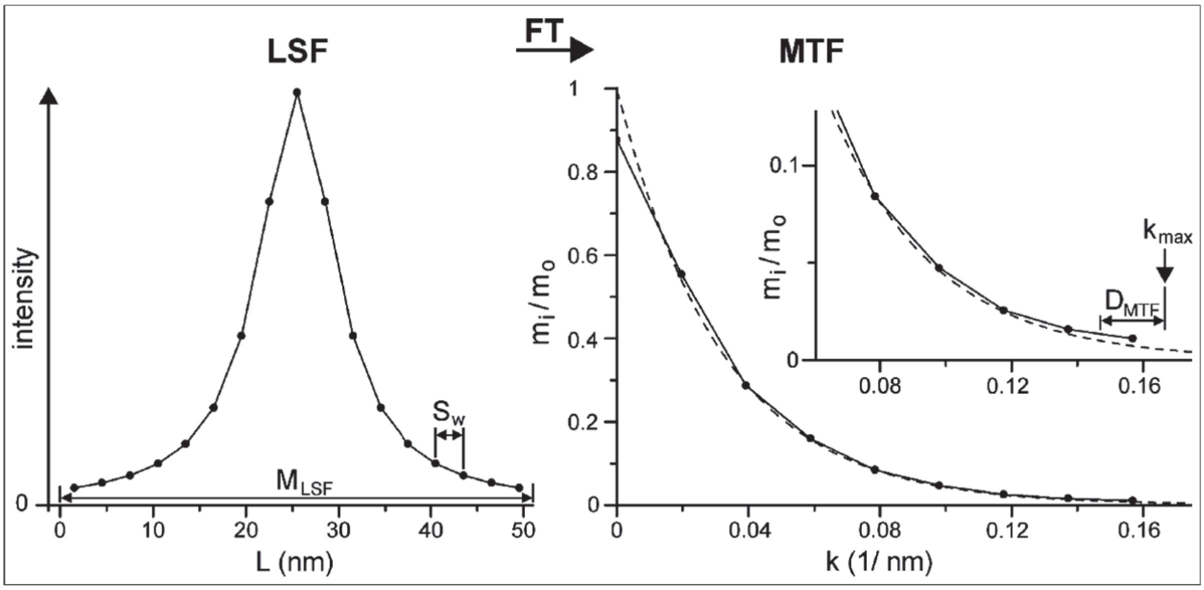

Figure 27 — Demonstration of the limits in M_{LSF} and S_W for the calculation of an MTF of sufficient accuracy and range from a Lorentzian LSF. The MTF denoted by black dots is calculated from the LSF given on the left side characterized by the following parameters: $M_{LSF} = 5w_{LSF}$ corresponds to the limit given in Formula (20) and $S_W = 0.3w_{LSF}$ corresponds to the limit given in Formula (23). The MTF denoted by the dashed line represents the ideal case and was calculated from a Lorentzian LSF with $M_{LSF} = 100w_{LSF}$ and $S_W = 0.1w_{LSF}$

It has been demonstrated that the MTF can be calculated by Fourier transform of the LSF. The accuracy and k range of the MTF depend on the length range over which the LSF is measured and the sampling step width, respectively. In particular, the measurement range must be large enough because a cut-off of the tails of the LSF causes deviations from the true shape of the MTF. The sampling step width does not limit the accuracy of the MTF in most cases because 2.5 to 3.5 measured values per FWHM of the LSF are enough for a sufficient k range of the calculated MTF.

4.2.6 Requirements for test samples and accuracy of measurement

Accuracy (trueness and precision) of measurements , depends on sample properties and measurement conditions. Therefore the requirements for test samples were derived from the needed accuracy.

Stripe width

It is advantageous to use a test sample which enables the determination of the LSF without a deconvolution procedure. For that reason the sample must have a narrow stripe whose width w_S is at most the half of the expected width w_{LSF} of the LSF. Then w_{LSF} can be taken from the measured profile over a narrow stripe and its deviation from the true value is below 6 % for a Gaussian profile and below 12 % for a Lorentzian profile, respectively (cf. Figure 15). This deviation can be reduced by the use of a narrower stripe, but also signal intensity and signal-to-noise ratio will be reduced by doing this. For that reason the recommended stripe width is $0.2\ w_{LSF} \leq w_s \leq 0.5\ w_{LSF}$.

Stripe distance

A sufficient distance d between the narrow stripe and neighboured features in the samples surface is an essential condition for the accurate measurement of the LSF. For a Gaussian LSF a distance of $d = 3\ w_{LSF}$ enables the determination of the LSF down to 0.5 % of its maximum intensity. For long tailed LSFs the distance between neighboured stripes must be larger. For a Lorentzian LSF a distance of $d = 10\ w_{LSF}$ is needed to measure the 3 % level of the LSF (cf. Figure 28).

The determination of w_{LSF} from the measured stripe profile is influenced by superposition of neighboured stripe profiles. The superposition has two effects on w_{LSF}:

1. The stripe profile is broadened and w_{LSF} is enlarged compared to its true value $(w_{LSF})_t$.
2. The background and therewith the 50 % level of intensity are shifted upwards and w_{LSF} is taken at a higher intensity level where the stripe profile is narrower (cf. Figure 29).

Both effects together result in a distance dependent reduction $(\Delta w_{LSF})_d$ of w_{LSF} compared to its true value $(w_{LSF})_t$ without superposition. The determination of w_{LSF} directly from the measured stripe profile results in a larger deviation $(\Delta w_{LSF})_d$ than the determination of w_{LSF} by fitting the measured profile with a model function. The higher accuracy of the fitting procedure is based on the variation of the baseline offset y_0 whose value determined by the fitting procedure is always smaller than the minimum intensity between two stripe profiles (cf. Figure 29).The deviation $(\Delta w_{LSF})_d$ as a function of stripe distance d is given in Figure 30.

As a consequence of the results presented above the following stripe distances d of the test sample are recommended for the determination of the width w_{LSF}:

$$\text{Gaussian LSF: } d \geq 2.5\ w_{LSF} \tag{24}$$

$$\text{Lorentzian LSF: } d \geq 5\ w_{LSF} \tag{25}$$

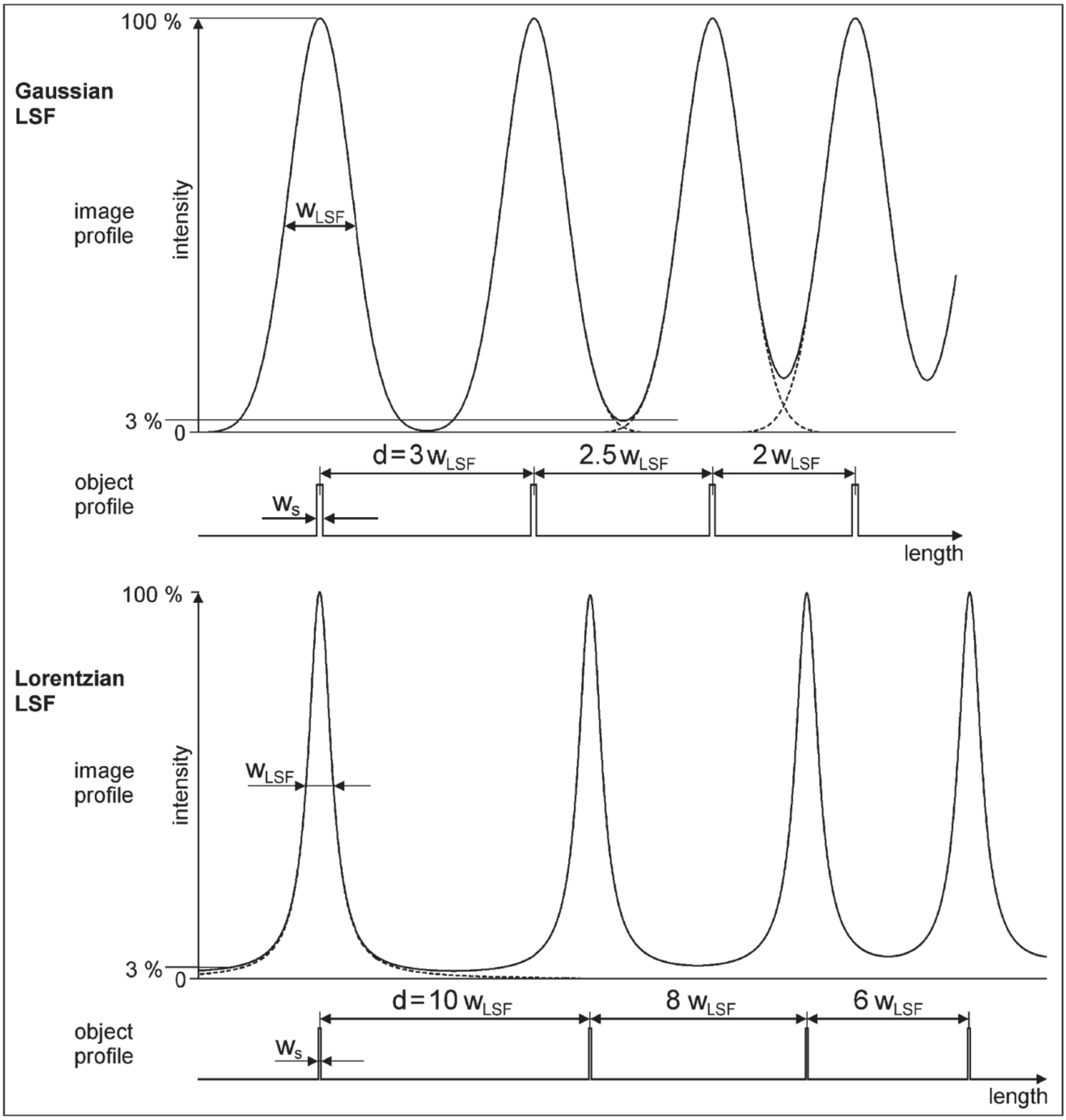

Figure 28 — The effect of stripe distance d on measurement of LSF tails. The image profile was simulated by convolution of narrow stripes (w_S = 10 nm) with a Gaussian LSF (top, w_{LSF} = 100 nm) and a Lorentzian LSF (bottom, w_{LSF} = 100 nm), respectively. Note the different length scales expressed in w_{LSF} units

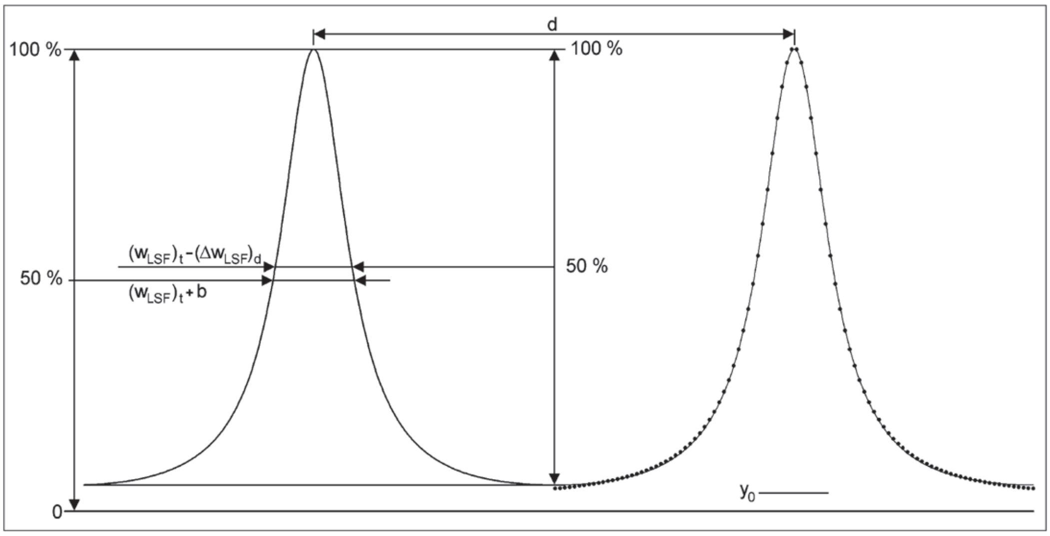

Figure 29 — The effect of superposition on the determination of w_{LSF} by measurement of profile width (left) and fitting (dots, right). The image profile was simulated by convolution of narrow stripes (w_s = 10 nm, d = 600 nm) with a Lorentzian LSF (w_{LSF} = 100 nm). $(w_{\mathrm{LSF}})_t$ is the true value of w_{LSF} without superposition, b is the value of w_{LSF} – broadening by superposition, $(\Delta w_{\mathrm{LSF}})_d$ is the reduction of w_{LSF} measured at 50 % from the background, y_0 is the baseline offset determined by the fitting procedure

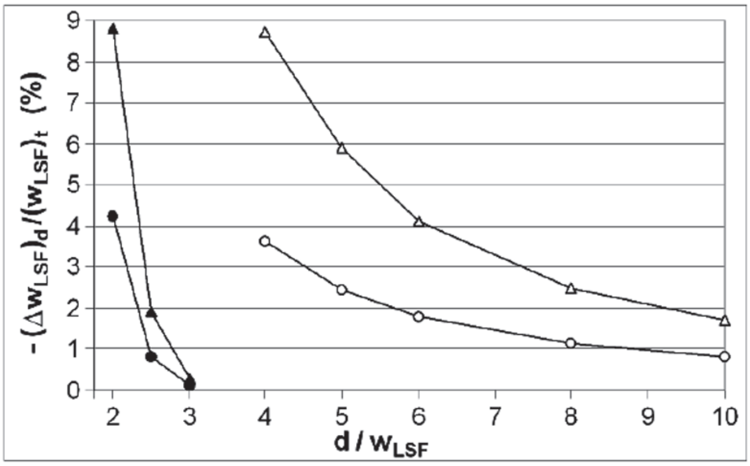

Figure 30 — The relative deviation $(\Delta w_{\mathrm{LSF}})_d/(w_{\mathrm{LSF}})_t$ in dependence on the normalized stripe distance d/w_{LSF} for Gaussian LSFs (closed symbols) and Lorentzian LSFs (open symbols). The triangles refer to the direct determination of w_{LSF} from profile width and the circles refer to the determination of w_{LSF} by fitting. The fitting interval was $(x-d/2, x+d/2)$ as shown in Figure 29. The deviation of w_{LSF} due to the finite width of the stripes (cf. Figure 15) is not included in $(\Delta w_{\mathrm{LSF}})_d$

All given values are related to the case that the neighboured features give the same signal intensity as the narrow stripe under consideration. The neighboured features may show higher signal intensities than the narrow stripe because their width and/or analyte concentration may be higher than that of the narrow stripe (cf. Figure 71). In this case the distance between the narrow stripe and the neighboured features must be greater than the values given above.

Object contrast

The object contrast between the narrow stripe and the surrounding area influences the signal-to-noise ratio, which is an essential factor for the precision of the determination of the LSF. Therefore the object contrast must be as high as possible because it enables a high precision of measurement and/or short measuring times.

Measurement uncertainty of w_{LSF}

The measurement uncertainty is a measure of the accuracy of a measurement method. It combines systematic deviations (trueness) and random deviations (precision). If a systematic deviation of w_{LSF} from its true value is known (e.g. from Figure 15), then the resulting value of w_{LSF} can be corrected. Without such a correction the systematic deviation is a part of measurement uncertainty as demonstrated below.

The combined relative measurement uncertainty of w_{LSF} is calculated for two examples:

Ex1: Gaussian LSF, stripe width $w_s = 0.5w_{LSF}$, stripe distance $d = 3w_{LSF}$, $R_{S/N} = 30$, $(\text{samples}/w_{LSF}) = 6$.

Ex2: Lorentzian LSF, stripe width $w_s = 0.25\,w_{LSF}$, stripe distance $d = 6w_{LSF}$, $R_{S/N} = 10$, $(\text{samples}/w_{LSF}) = 10$.

Systematic deviation

Systematic deviations of w_{LSF} from its true value $(w_{LSF})_t$ are caused by the finite width w_s of the stripes of the test sample (cf. Figures 14 and 15) and by superposition of neighbouring stripe profiles which depends on stripe distance d (cf. Figures 28, 29, 30). The deviations by the latter effect were taken for the determination of w_{LSF} by fitting because the random deviations (see below) were also determined for the fitting procedure.

Ex1: Broadening of w_{LSF} by finite stripe width w_s: $(\Delta w_{LSF})_{ws}/(w_{LSF})_t = +\,5.9\ \%$ (from Figure 15).

Reduction of w_{LSF} by superposition: $(\Delta w_{LSF})_d/(w_{LSF})_t = -\,0.12\ \%$ (from Figure 30).

Because the deviations have definitively opposite signs they have to be subtracted.

→ Systematic deviation: $\Delta w_{LSF}\,/(w_{LSF})_t = (\Delta w_{LSF})_{ws}\,/(w_{LSF})_t + (\Delta w_{LSF})_d\,/(w_{LSF})_t = 5.9\ \% - 0.1\ \% = 5.8\ \%$.

Ex2: Broadening of w_{LSF} by finite stripe width w_s: $(\Delta w_{LSF})_{ws}/(w_{LSF})_t = +\,3.1\ \%$ (from Figure 15)

Reduction of w_{LSF} by superposition: $(\Delta w_{LSF})_d/(w_{LSF})_t = -\,1.8\ \%$ (from Figure 30)

→ Systematic deviation: $\Delta w_{LSF}\,/(w_{LSF})_t = (\Delta w_{LSF})_{ws}\,/(w_{LSF})_t + (\Delta w_{LSF})_d\,/(w_{LSF})_t = 3.1\ \% - 1.8\ \% = 1.3\ \%$.

Random deviation

The precision of w_{LSF}, determined by fitting of a noisy stripe profile, depends on the measuring conditions, in particular signal-to-noise ratio $R_{S/N}$ and sampling step width. Deviations of w_{LSF} from the true value $(w_{LSF})_t$ of the noise-free profile were determined by fitting a great number of synthetic profiles with different $R_{S/N}$ and different sampling step widths (cf. 4.2.3). The deviation s, calculated according to Formula (17) and displayed in Figure 21, corresponds to the accuracy of w_{LSF} determined by a fitting procedure applied to *one* measured profile over a narrow stripe. It includes statistical errors as well as possible systematic errors[2] of the fitting procedure.

Ex1: Gaussian, $R_{S/N} = 30$, $\text{samples}/(w_{LSF}) = 6$ → $s/(w_{LSF})_t = 2.5\ \%$ (from Figure 21).

Ex2: Lorentzian, $R_{S/N} = 10$, $\text{samples}/(w_{LSF}) = 10$ → $s/(w_{LSF})_t = 5.6\ \%$[3].

---

[2] Other systematic deviations than those related to stripe width and stripe distance (treated above).

[3] The effect of noise and sampling step width on the accuracy of the determination of w_{LSF} was analyzed for a Gaussian LSF only (cf. 4.2.3). The resulting values for the deviation *s* will be similar for other model functions. Therefore the value $s\ /(w_{LSF})_t = 5.6\ \%$, calculated for a Gaussian LSF (cf. Figure 21), was taken for the Lorentzian LSF of example 2 too.

The deviation *s* (cf. Formula 17) is a measure of the dispersion of w_{LSF} and corresponds to the uncertainty u_r which is caused mainly[4] by random deviations. It is usual to give the expanded uncertainty

$$U_r = k\, u_r \qquad (26)$$

where k is the coverage factor.[22] With $k = 2$ (level of confidence = 95 %) we get

Ex1: $U_r/(w_{LSF})_t = 5.0$ %.

Ex2: $U_r/(w_{LSF})_t = 11.2$ %.

Combined uncertainty

According to the GUM approach[22] the quadratic addition of different components, here the systematic deviation and the random deviation, gives the combined uncertainty[5]

$$U_c = [U_r^2 + (\Delta w_{LSF})^2]^{½} \qquad (27)$$

Then the relative combined uncertainties of w_{LSF} are:

Ex1: Gaussian LSF, $w_s = 0.5 w_{LSF}$, $d = 3 w_{LSF}$, $R_{S/N} = 30$, samples/$(w_{LSF}) = 6$

$$U_c/(w_{LSF})_t = [(5.0\ \%)^2 + (5.8\ \%)^2]^{½} = 7.7\ \%$$

Ex2: Lorentzian LSF, $w_s = 0.25 w_{LSF}$, $d = 6\, w_{LSF}$, $R_{S/N} = 10$, samples/$(w_{LSF}) = 10$

$$U_c/(w_{LSF})_t = [(11.2\ \%)^2 + (1.3\ \%)^2]^{½} = 11.3\ \%$$

An uncertainty of 7.7 %, as calculated for example 1, seems to be sufficient in most cases. It includes a systematic deviation of +5.8 % which can be reduced by the use of a narrower stripe.

The uncertainty of 11.3 %, calculated for example 2, is nearly completely caused by the low signal-to-noise ratio $R_{S/N} = 10$. It can be improved by increasing the measurement time and/or the number of samples per w_{LSF}. Another possibility is to use a wider stripe of the test sample which increases signal (cf. Figure 14) and $R_{S/N}$, but the decrease in random deviation may be partly or completely compensated by an increased systematic deviation due to a stronger broadening of the measured stripe profile (cf. Figure 15).

If the measured LSF corresponds not to one of the known model functions the accuracy of the fit may be lower and the uncertainty U_c of w_{LSF} may be larger than in the given examples. For low noise levels (i.e. high $R_{S/N}$) w_{LSF} can be determined directly from the measured profile without a fitting procedure. Then its uncertainty is similar or slightly increased (by superposition of neighboured stripe profiles, cf. Figure 30) compared to that w_{LSF} determined by fitting the same profile.

4.3 Determination of the edge spread function (ESF) by imaging a straight edge

Imaging of a straight edge is the method most often used in nanoscale surface analysis to determine the lateral resolution of an imaging instrument. A line profile perpendicular to the edge gives the ESF, which is the integral of the line spread function LSF (cf. 4.1.3). The steepness of a line profile through the image of a straight edge or the steepness of a line scan over a straight edge corresponds to image sharpness. Distances $D_{x\text{-}(100\text{-}x)}$ between points of well-defined intensities *x* and 100-*x* (e.g. 20 % to 80 %) of the profile over a straight edge quantify the steepness (Figure 31) and can be taken as measures of sharpness.

---

[4] The difference in Formula (17) is calculated with the true value $(w_{LSF})_t$ in stead of the arithmetic mean and therefore *s* includes, besides the statistical error, also possible systematic deviations of the fitting procedure.

[5] The coverage factor has to be applied only to the random components of uncertainty and therefore Δw_{LSF} is not expanded.

The ideal straight edge in chemical surface analysis is a sharp chemical gradient (“step transition”) between two constant levels of concentration of a chemical constituent without height differences in the related topography. In practical analysis such a straight edge is called a “chemical edge”. The regions of constant concentration on both sides of the edge must be wide enough to reach 0 % and 100 % levels of intensity, respectively (cf. 4.3.3 and 4.3.5). However, it can be difficult to establish and control that prerequisite for real test samples.

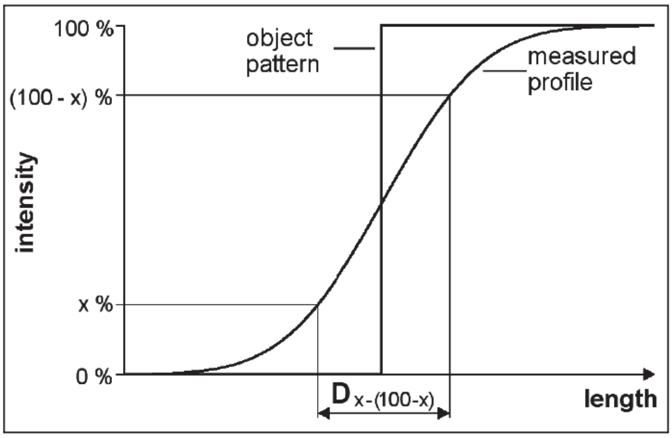

Figure 31 — Definition of parameters characterizing the steepness of a profile measured over a straight edge

4.3.1 Model functions for the ESF

The ESF is the integral of the LSF and correspondingly the ESF can be described by the integral of model functions for the LSF,[14] so called peak functions, as, e.g. a Gaussian function, a Lorentzian function and a combination of these functions (Pseudo-Voigt functions, cf. 4.2.1). The integration of those peak functions corresponds to a convolution of the peak function with a step function (cf. 4.1.3) and can be done by numerical integration. The integrated Gaussian function is also known as the error function

$$\operatorname{erf}(z) = \frac{2}{\sqrt{\pi}} \int_0^z \exp\left(-t^2\right) \mathrm{d}t \tag{28}$$

With the parameters used in Formula (12) it has the form

$$\operatorname{erf}(x/\sqrt{2}\sigma) = \frac{2}{\sqrt{2\pi}\sigma} \int_0^x \exp\left(-\frac{(x_1 - x_0)^2}{2\sigma^2}\right) \mathrm{d}x_1 \tag{29}$$

Figure 32 shows different kinds of ESFs calculated by numerical integration of model peak functions having the same FWHM. Figure 33 shows integrated type 2 Pseudo-Voigt functions (cf. 4.2.1). This figure demonstrates the high versatility of this type of function.

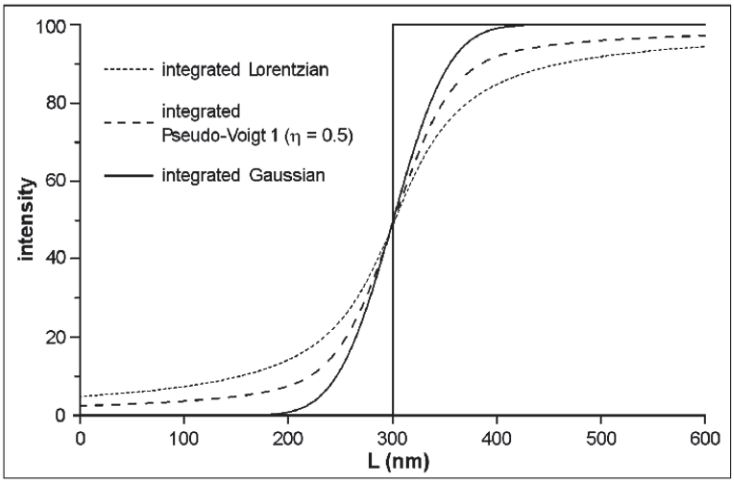

Figure 32 — ESFs calculated by integration of peak functions shown in Figure 11. All peak functions have the same w_{LSF} = 100 nm

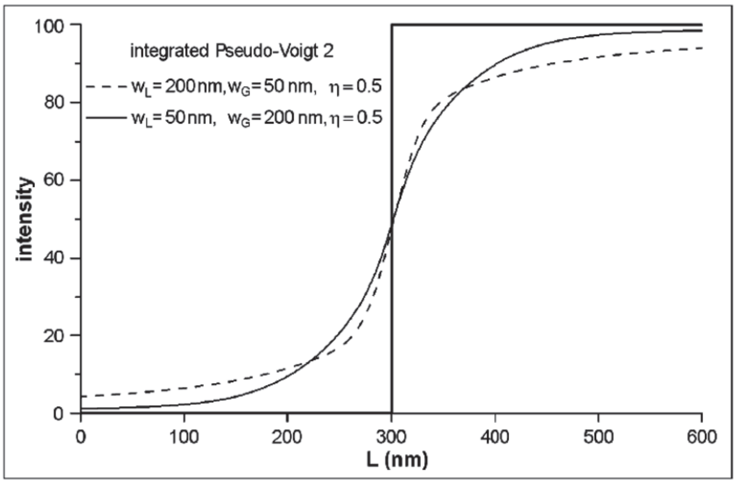

Figure 33 — ESFs calculated by integration of Pseudo-Voigt functions of type 2 shown in Figure 13

The ESF may also be described by different types of sigmoidal functions. The logistic sigmoid function

$$I(x) = a/\{1 + \exp[-k_S(x - x_0)]\} \tag{30}$$

where a is the upper limit, k_S determines the steepness and x_0 is the position of the inflection point, has a very similar shape in comparison to the integrated Gaussian function (cf. Figure 34). An extended version of the logistic function[23] enables the description of asymmetric profiles with a drift induced variation of the lower and upper level. This type of function was used to fit line scans across a chemical edge recently.[24] The software “Logistic Function Profile Fit” (LFPF) for conveniently fitting such profiles is available from the National Institute of Standards and Technology [25].

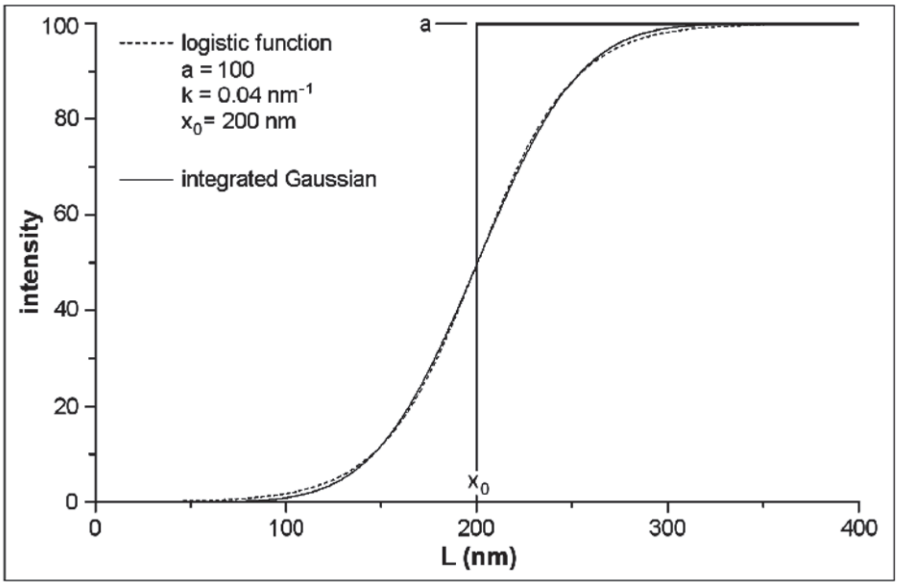

Figure 34 — Integrated Gaussian function (w_{LSF} = 100 nm) fitted by the logistic sigmoid function

If the ESF deviates considerably from an integrated Gaussian, a sum of logistic functions can be used for fitting. Figure 35 shows fits of an integrated Lorentzian. The sum of two logistic functions with different parameters fits better than the extended logistic function with additional drift parameters related to the lower and upper level of intensity. As a consequence the sum of two logistic functions is the most general method for the fit of an unknown ESF.

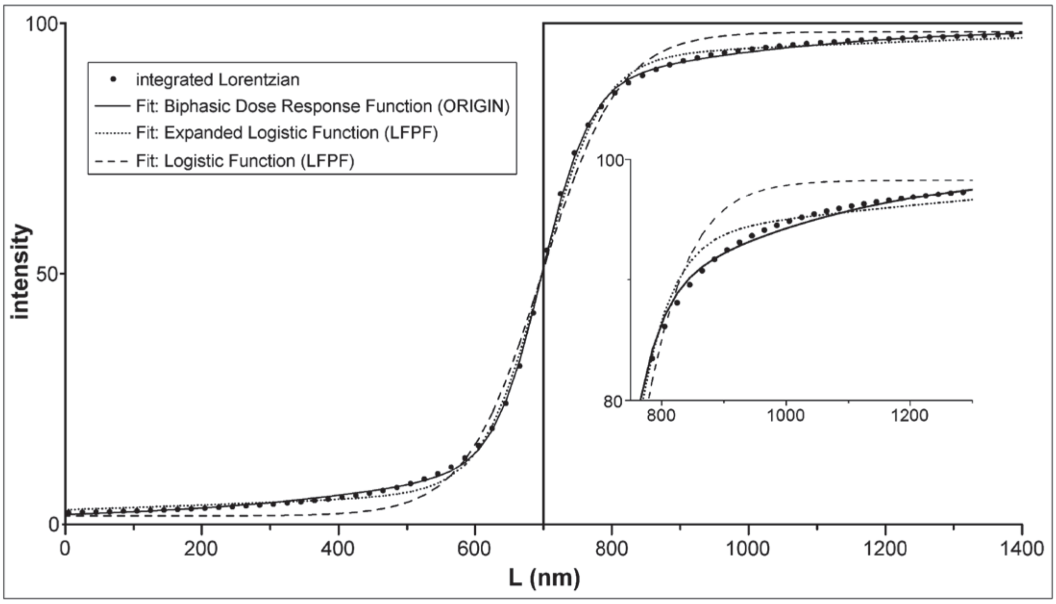

Figure 35 — Fits of an integrated Lorentzian function (w_{LSF} = 100 nm) with different sigmoid functions (fit range 5 000 nm). The insert shows the region of largest deviation of the fits with an expanded intensity scale. ORIGIN ™ and LFPF [25] are the programs used for fitting with the given functions

4.3.2 The relation of the ESF distance $D_{\mathrm{x}-(100\text{-}\mathrm{x})}$ to LSF models

ESF-parameters such as the distance $D_{\mathrm{x}-(100\text{-}\mathrm{x})}$ (Figure 31) depend both on the width and shape of the LSF which characterizes the quality of an image and the performance of an imaging instrument.

Figure 36 shows three ESFs simulated with LSFs of different $\mathrm{w}_{\mathrm{LSF}}$ but the same shape, a Gaussian peak function. Figure 37 shows two ESFs simulated with Gaussian and Lorentzian LSFs having the same $\mathrm{w}_{\mathrm{LSF}}$. Obviously the steepness of the ESFs is very different for these cases. The ESF simulated with a Gaussian LSF is much steeper in comparison to that simulated with a Lorentzian LSF. Correspondingly the ESF $\mathrm{D}_{\mathrm{x}\,-\,(100\text{-}\mathrm{x})}$ data resulting for the Lorentzian LSF model are much larger than for the Gaussian LSF. The linear relation between the ESF parameters $\mathrm{D}_{\mathrm{x}\,-\,(100\text{-}\mathrm{x})}$ and the $\mathrm{w}_{\mathrm{LSF}}$ is given in Table 4 (cf.[14]).

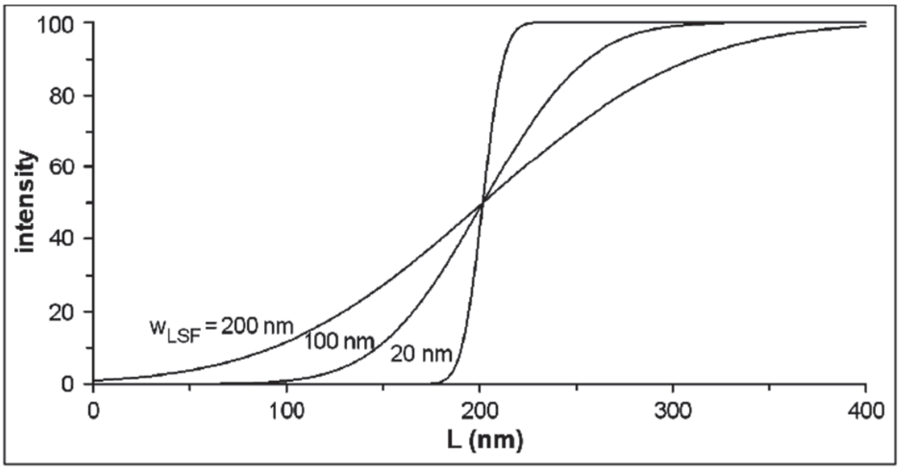

Figure 36 — ESFs simulated by convolution of a step transition with Gaussian LSFs of different w_{LSF}

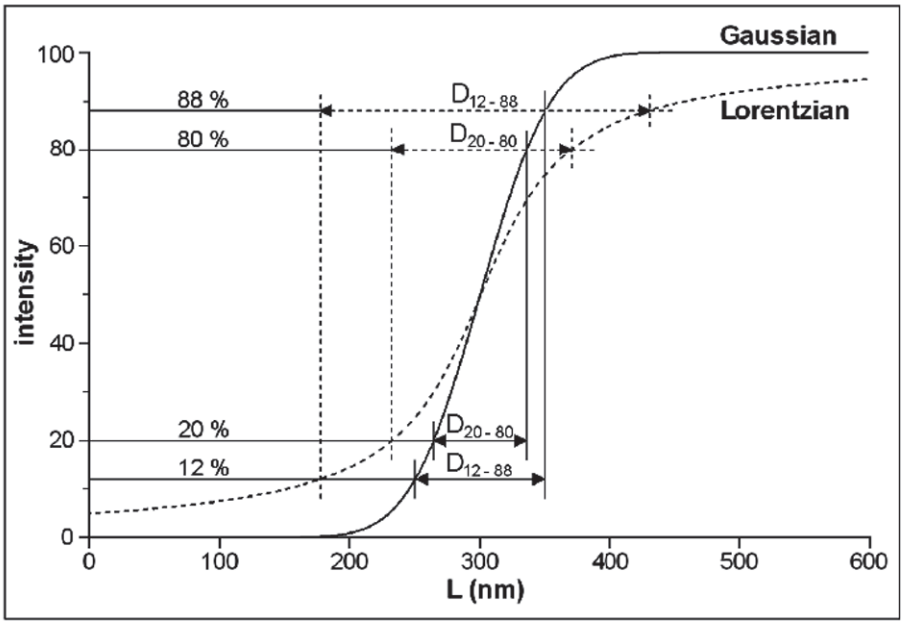

Figure 37 — ESFs simulated by convolution of a step transition by using Gaussian and Lorentzian LSFs with equal w_{LSF} of 100 nm

Table 4 — Relation of ESF-parameters to w_{LSF} (FWHM) for Gaussian and Lorentzian LSFs

ESF	Gaussian LSF		Lorentzian LSF
	σ	w_{LSF}	w_{LSF}
D_{12-88}	$2.35 \times \sigma$	$1 \times w_{\mathrm{LSF}}$	$2.54 \times w_{\mathrm{LSF}}$
D_{16-84}	$2 \times \sigma$	$0.849 \times w_{\mathrm{LSF}}$	$1.83 \times w_{\mathrm{LSF}}$
D_{20-80}	$1.68 \times \sigma$	$0.715 \times w_{\mathrm{LSF}}$	$1.38 \times w_{\mathrm{LSF}}$

4.3.3 Size of plateau regions and its effect on the ESF distance $D_{\mathrm{x}-(100\text{-}\mathrm{x})}$

As mentioned already, the widths of the two plateaus of constant concentration on both sides of the chemical edge must be large enough to avoid erroneous determination of the ESF distances $D_{\mathrm{x}-(100\text{-}\mathrm{x})}$. Particularly for the case of long-tailed LSFs, this condition may be not fulfilled and in that case the ESF distances $D_{\mathrm{x}-(100\text{-}\mathrm{x})}$ cannot be correctly determined. Consequently lateral-resolution data deduced from these erroneously small $D_{\mathrm{x}-(100\text{-}\mathrm{x})}$ values will be systematically underestimated. This erroneous underestimation is illustrated by simulations in Figure 38. This figure shows the effect of the length L_{pl} of the upper plateau of constant concentration on the shape of the ESF measured across the edge(s). In the case of a Gaussian LSF characterizing the performance of the imaging instrument the resulting ESF reaches the 100 % level if the length of the upper plateau is at least three times the w_{LSF}. In the case of the long-tailed Lorentzian LSF very long plateaus are needed to reach a level close to 100 % for the ESF.

A correct determination of ESF distances $D_{\mathrm{x}-(100\text{-}\mathrm{x})}$ is based on the existence of flat 0 % and 100 % intensity levels in the image or line scan of a step transition. For very noisy profiles, it may be difficult to verify the 0 % and 100 % intensity levels. Therefore, the accuracy of a determination of ESF distances $D_{\mathrm{x}-(100\text{-}\mathrm{x})}$ has to be analysed for noisy profiles. Unfortunately, the parameter $L_{\mathrm{pl}}/w_{\mathrm{LSF}}$ that was used to characterize the simulations in Figure 38 is not available in measurements across a step transition. However, the steepness of the profile expressed as the distance $D_{20\text{-}80}$ (cf. Figure 31) and the width of the image profile w_{im} (cf. Figure 38) are available from a measured profile across two step transitions. Therefore the parameter $w_{\mathrm{im}}/D_{20\text{-}80}$ may be used to estimate whether the length of a plateau of constant concentration is wide enough for a correct determination of ESF distances $D_{\mathrm{x}-(100\text{-}\mathrm{x})}$ or not. A relation between the $w_{\mathrm{im}}/D_{20\text{-}80}$ parameter and the accuracy of ESF parameters is valid only for defined shapes of the LSF and ESF, respectively.

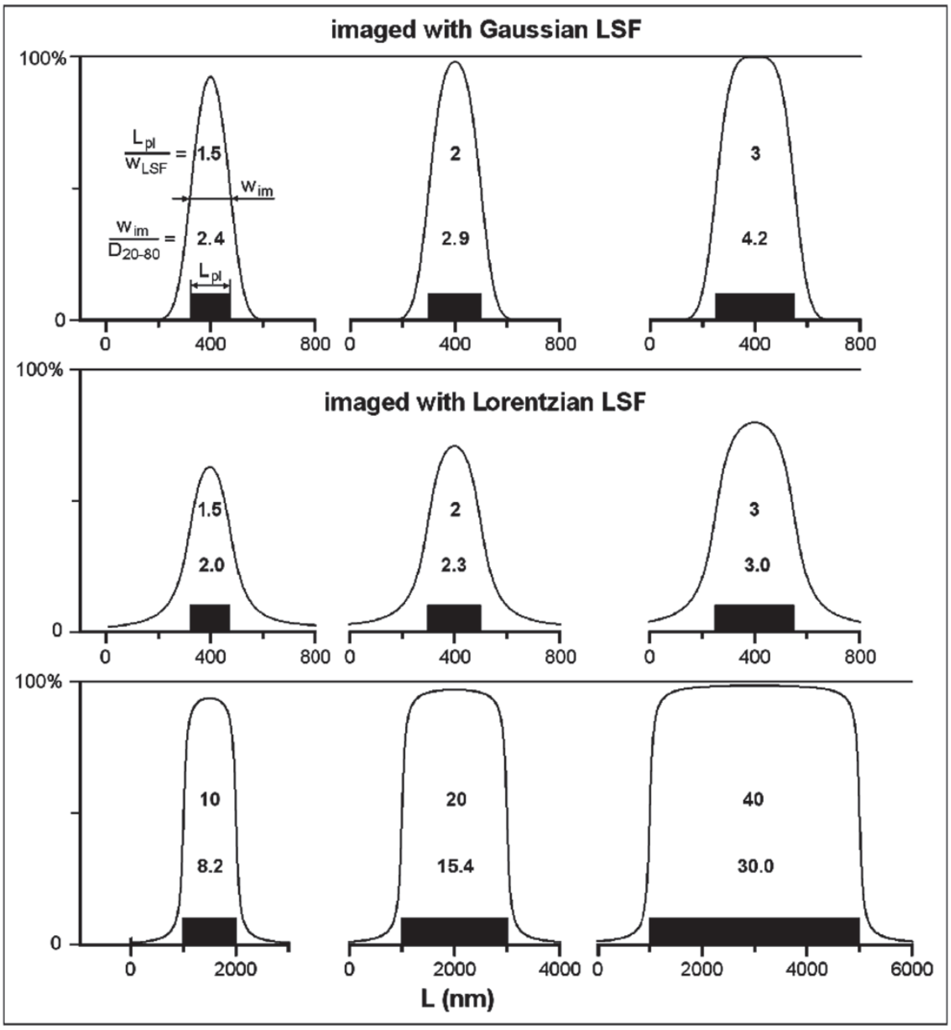

Figure 38 — Effect of the length of the upper plateau L_{pl} represented by a black rectangle on the shape of the resulting ESF. The ESF was simulated by convolution of rectangle profiles with Gaussian and Lorentzian LSFs with w_{LSF} = 100 nm. The width of the image profile w_{im} (top left) and the parameter $D_{20\text{-}80}$ (for definition cf. Figure 31) were taken from the simulated profile

In practice, this situation is a strong limitation of the applicability of the straight-edge method for the characterization of the lateral resolution. Imaging a step transition with a probe characterized by a Gaussian LSF gives the correct ESF distances $D_{x-(100-x)}$ for $w_{im}/D_{20\text{-}80} \geq 4$ whereas for a Lorentzian LSF much higher values are needed (cf. Figure 38).

The relative underestimation of the ESF distances $D_{12\text{-}88}$ and $D_{20\text{-}80}$ expressed as the deviation from their true value as function of the plateau length is given in Figure 39. It enables an estimation of accuracy of the ESF distances $D_{12\text{-}88}$ and $D_{20\text{-}80}$ for Gaussian and Lorentzian LSFs. For imaging with a Gaussian LSF the relative deviation of $D_{12\text{-}88}$ and $D_{20\text{-}80}$ from true values is nearly the same, whereas for long tailed LSFs (e.g. a Lorentzian) the deviation of $D_{12\text{-}88}$ is much higher than that of $D_{20\text{-}80}$.

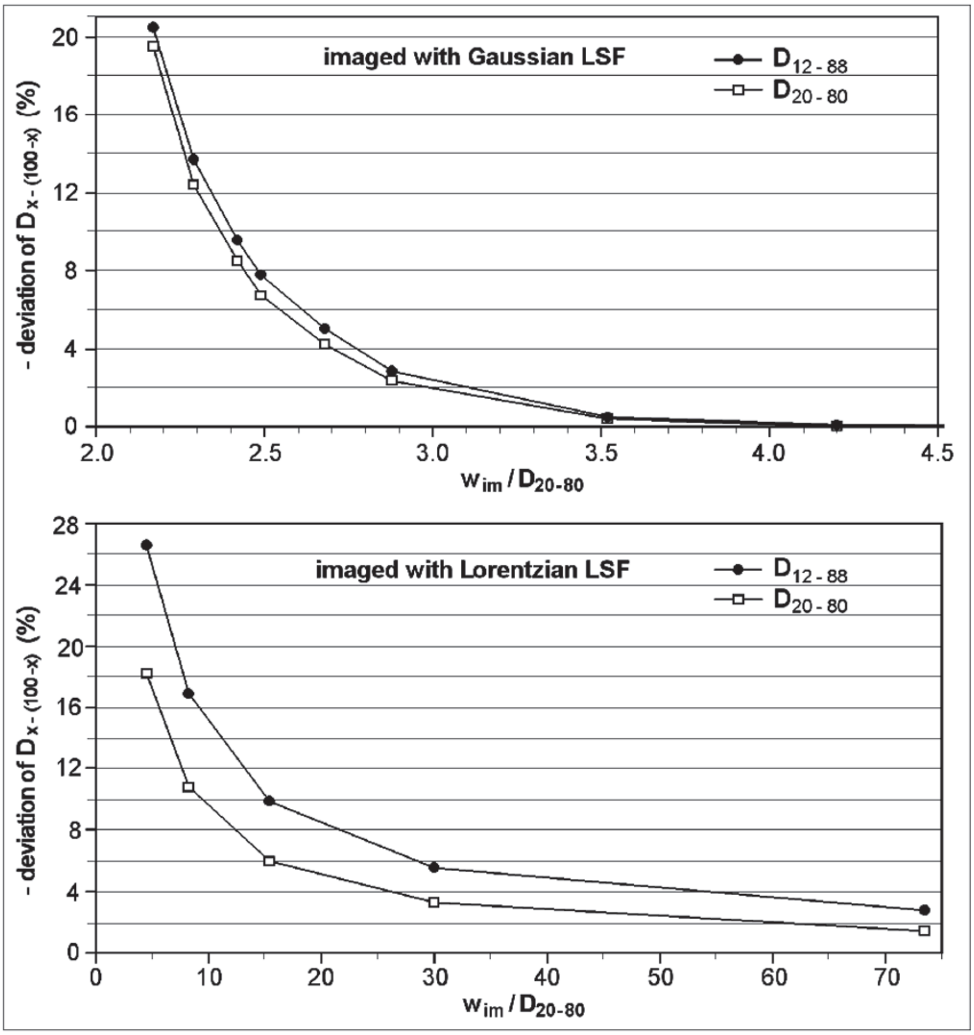

Figure 39 — Relative deviations of $D_{12\text{-}88}$ and $D_{20\text{-}80}$ from their true values as function of the length of the upper plateau of a step transition. The measured length of the plateau w_{im} (cf. Figure 38) is normalized to the measured steepness $D_{20\text{-}80}$. Note the rather different scales of normalized plateau length $w_{\mathrm{im}}/D_{20\text{-}80}$ for both kinds of LSF

4.3.4 The relation of the ESF distance $D_{\mathrm{x}\,-\,(100\text{-x})}$ to effective lateral resolution

In principle lateral resolution is defined as the minimum spacing at which two features of the image can be recognized as distinct and separate. Therefore it can be determined only by the imaging of at least two features. In real imaging of those features effective lateral resolution depends on the width and shape of the LSF, the signal-to-noise ratio $R_{\mathrm{S/N}}$ and the number of sampling points per grating period as outlined later in 4.4.2. Correspondingly, the relation between effective lateral resolution and the ESF distances $D_{\mathrm{x}\,-\,(1\text{-x})}$ can be found by the calculation of these values for different types of LSF with different $\mathrm{w}_{\mathrm{LSF}}$ and different levels of noise.

Figure 40 shows four different ESFs which all correspond to an effective lateral resolution of 100 nm. They were calculated by convolution of different LSFs with a step function and subsequent addition of noise. The values of $\mathrm{w}_{\mathrm{LSF}}$ were determined in such a way (cf. Figure 62), that the corresponding CTFs and the noise-dependent functions $(c_{\mathrm{i}}\,/c_{\mathrm{o}})_{\mathrm{ThR}}$ [cf. Formula (49)] yield an effective cut-off frequency of 10 µm^{-1}.

Figure 40 demonstrates that the values of ESF distances $D_{\mathrm{x}-(100\text{-x})}$ deviate considerably from the effective lateral resolution r_{e}. The often-used parameter $D_{20\text{-}80}$ is much smaller than r_{e} for Gaussian LSFs and much larger than r_{e} for a long-tailed Lorentzian LSF measured with a high signal-to-noise ratio (e.g. $R_{S/N} = 100$). ESF distances $D_{x\,-\,(100\text{-}x)}$ are rather a measure of sharpness than a measure of effective lateral resolution.

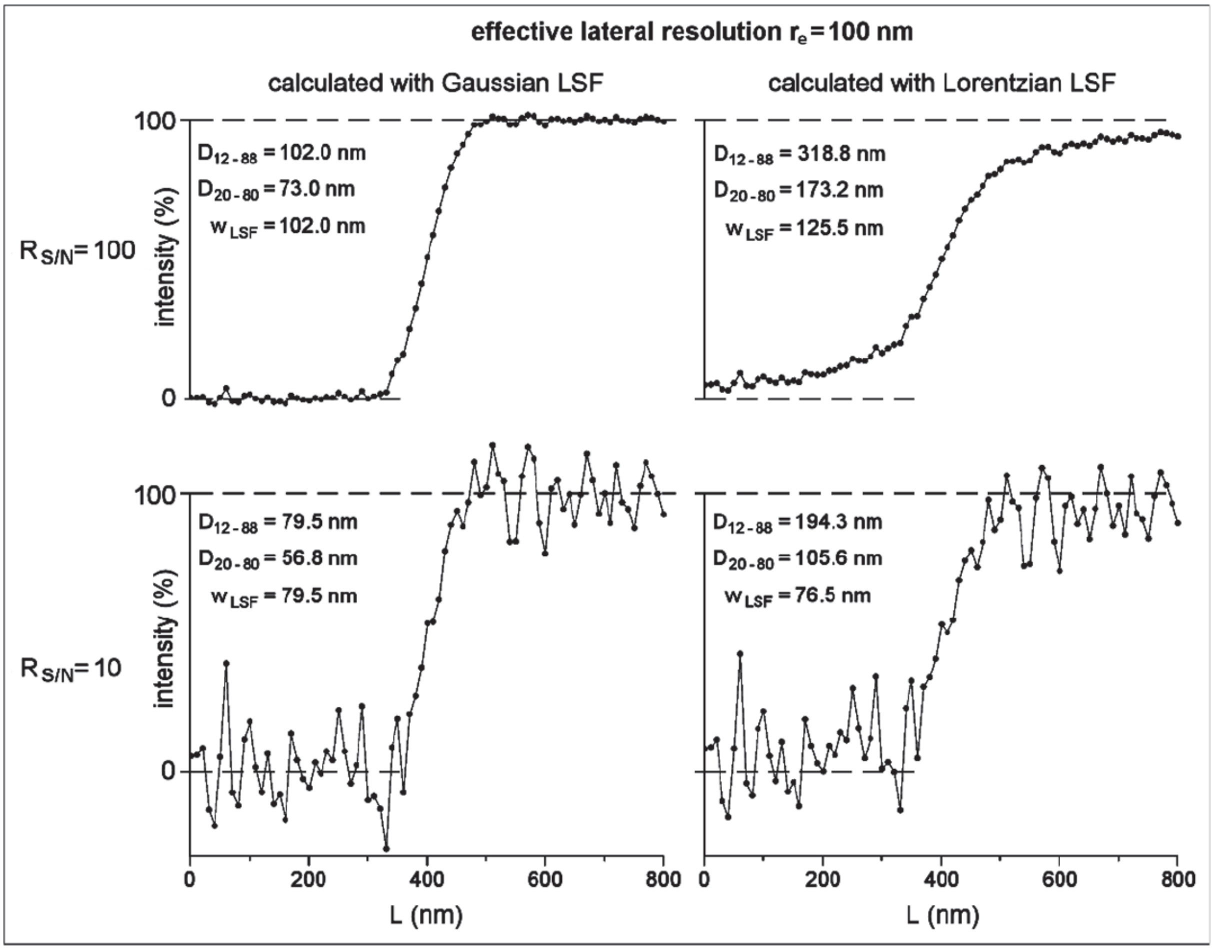

Figure 40 — ESFs calculated with different LSFs and different values of $R_{S/N}$. The values of w_{LSF} were chosen in such a way, that all ESFs correspond to a lateral resolution of 100 nm. The details of calculation are given in the text. The ESF-parameters $D_{12\text{-}88}$ and $D_{20\text{-}80}$ are calculated from w_{LSF} with the factors given in Table 4, and these values agree within the limits of accuracy with values determined from the curves

4.3.5 Requirements for test samples and accuracy of measurement

Accuracy (trueness and precision) of measurements, depends on sample properties and measurement conditions. Therefore the requirements for test samples were derived from the needed accuracy. The accuracy of the ESF and steepness parameters $D_{x\,-\,(100\text{-}x)}$ taken from the ESF (cf. 4.3.2) sensitively depends on sample properties as the steepness of the edge and the length of the plateau regions. Here the estimation of accuracy is demonstrated for $D_{12\text{-}88}$ because for a Gaussian LSF this parameter corresponds to the full width at half maximum w_{LSF}.

Steepness of the edge

The ESF is the convolution of the point spread function of an imaging system with a step transition (cf. Figure 4). It can be determined experimentally by imaging a sharp edge, but in contrast to the step transition model, real edges have a finite steepness which flattens the measured profile. This finite steepness may be due to the 3D-topography of the sample (edge of a slot, mesh bar of a grid, edge of a gold-island) or to a transition zone between areas of different chemical composition. Unfortunately in most cases the steepness of the edge is not known. As a result, the deviation of the measured profile from the exact ESF cannot be estimated. This is a fundamental disadvantage of the "edge method" compared to the “narrow stripe method”, where certified stripe widths enable an estimation of the deviation between measured stripe profile and exact LSF (cf. 4.2.6). Because of the lack of information on edge steepness its contribution to the uncertainty $D_{\mathrm{x}\,-\,(100\text{-}\mathrm{x})}$ parameters is not taken into account.

Length of plateau regions

The lengths of the two plateaus of constant concentration on both sides of the chemical edge must be large enough to avoid erroneous determination of the ESF distances $D_{\mathrm{x}\,-\,(100\text{-}\mathrm{x})}$. Particularly for the case of a long-tailed LSF, this condition may be not fulfilled and as a consequence $D_{\mathrm{x}\,-\,(100\text{-}\mathrm{x})}$ will be underestimated. This effect is demonstrated in Figure 41 for a Lorentzian LSF. An increased level of minimum intensity and a decreased level of maximum intensity is clearly visible in the image profile of a square-wave grating with a plateau length L_{pl} = 10 $\mathrm{w}_{\mathrm{LSF}}$. As a result also the 12 % and 88 % levels are shifted and the steepness parameter $D_{12\text{-}88}$ is reduced compared to that determined from a plateau of appropriate length L_{pl} = 40 w_{LSF}.

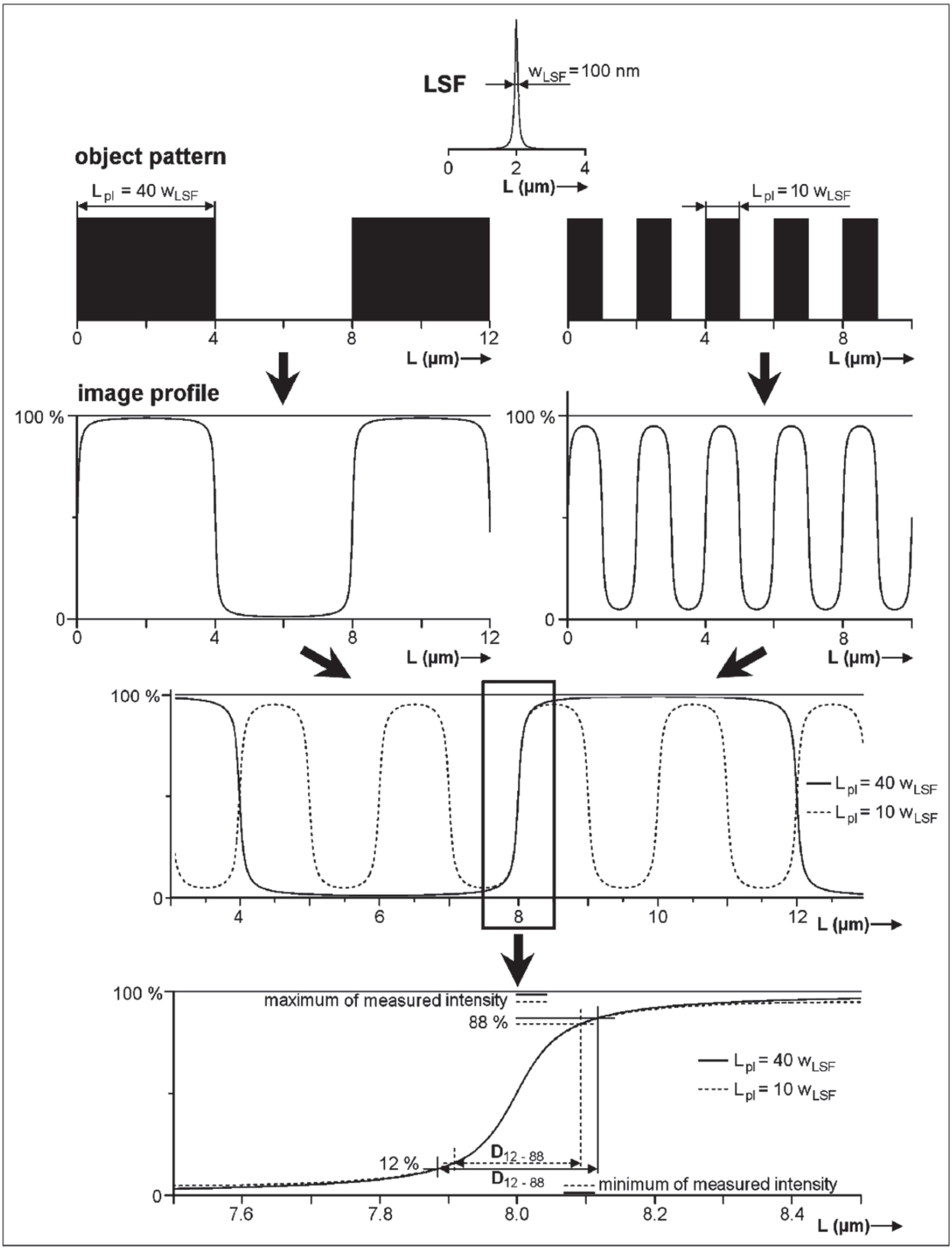

Figure 41 — The effect of plateau length L_{pl} on the ESF parameter D_{12-88}. The image profile was simulated by convolution of two square-wave gratings of different periods with a Lorentzian LSF (w_{LSF} = 100 nm)

The deviation of $D_{12\text{-}88}$ from its true value $(D_{12\text{-}88})_t$ as a function of the normalized plateau length L_{pl}/w_{LSF} is given in Figure 42 6). Plateau lengths of $L_{pl} \geq 2$ w_{LSF} (for a Gaussian LSF) and $L_{pl} \geq 40$ w_{LSF} (for a Lorentzian LSF), respectively, are recommended because in these cases the deviation of $D_{12\text{-}88}$ from its true value is smaller than 10 %.

The parameters $D_{x-(100\text{-}x)}$ can be determined either directly from the measured ESF or by fitting the measured ESF with a logistic function. In the latter case the parameter $D_{x-(100\text{-}x)}$ is explicitly given by the software (e.g. Logistic Function Profile Fit [25]) or it can be calculated from the exponent of a logistic function ($D_{12\text{-}88} = 1.73\ p$, where p is the exponent of the ORIGIN™ Dose Response Function). Figure 42 a) shows that $D_{12\text{-}88}$ deviates not more than +6 % from the true value if the edge is imaged with a Gaussian LSF and the fit is done with a logistic function. The systematic overestimation of $D_{12\text{-}88}$ -values taken from the fit is due to the facts that the minimum intensity of the fit curve is always smaller and the maximum intensity is always greater than the corresponding intensities of the measured edge profile for the case of a Gaussian LSF.

Figure 42 b) shows that for non-Gaussian LSFs the logistic function gives a poor fit of the ESF and therefore the calculated values of $D_{12–88}$ deviate more from the true value than values which were determined from the measured profile directly. Figure 35 (in 4.3.1) shows that ESFs resulting from a non-Gaussian LSF can be better fitted by a sum of two logistic functions (e.g. the Biphasic Dose Response Function). In this case no simple relation between $D_{x-(100\text{-}x)}$ and the parameters of the Biphasic Dose Response Function exists and therefore $D_{x-(100\text{-}x)}$ must be determined graphically from the fit curve. Fitting with a Biphasic Dose Response Function is useful only in the case of a noisy profile, which does not allow the determination of $D_{x-(100\text{-}x)}$ directly from the measured curve without a fit.

---

6) The results shown in Figures 41 and 42 are calculated by the variation of length of both plateaus related to a step transition whereas the results shown in Figures 38 and 39 are calculated by variation of the length of the upper plateau only.

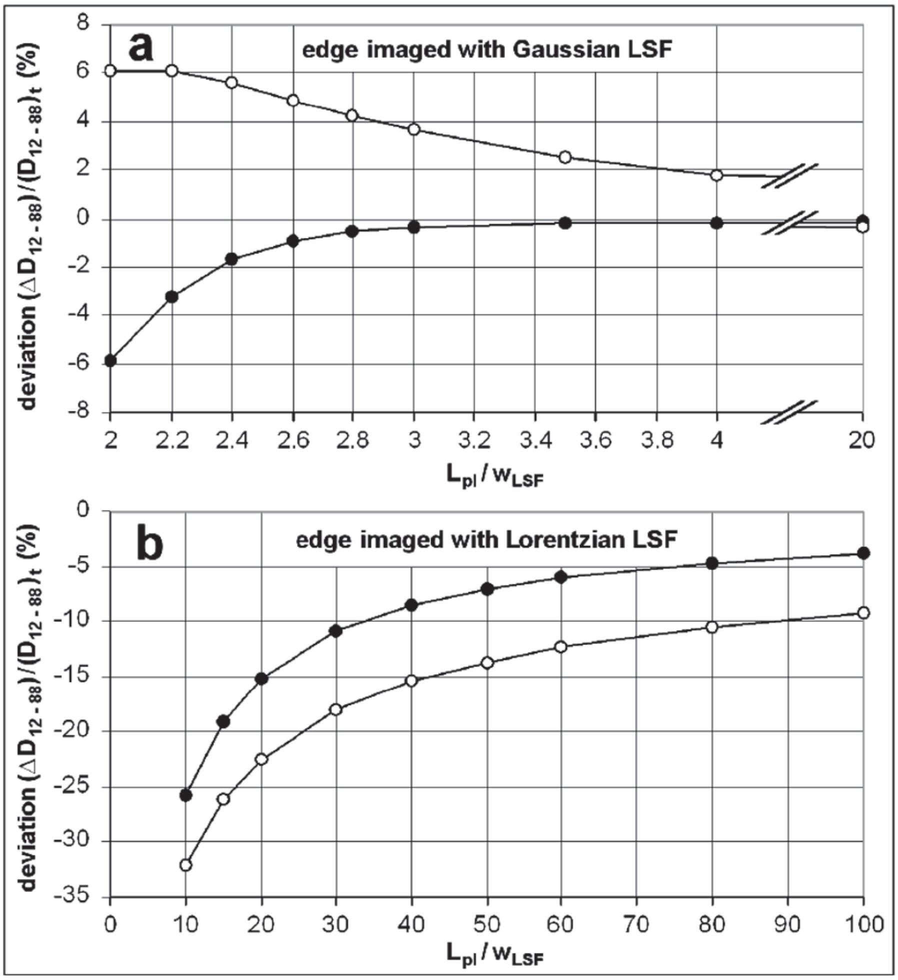

Figure 42 — The relative deviation ($\Delta D_{12\text{-}88}$) /($D_{12\text{-}88}$)$_t$ from the true value ($D_{12\text{-}88}$)$_t$ as a function of the normalized plateau length L_{pl}/w_{LSF}. Black dots: $\Delta D_{12\text{-}88}$ determined directly from the simulated profile; open circles: $\Delta D_{12\text{-}88}$determined by fitting the simulated profile with the Logistic Function Profile Fit [25]. Note the different length scales for profiles simulated by convolution with a) Gaussian and b) Lorentzian LSFs, respectively

The effect of noise on the accuracy of $D_{x\text{-}(1\text{-}x)}$

A noisy profile over a chemical edge must be fitted or smoothed because it is not possible to determine $D_{x\text{-}(1\text{-}x)}$ directly from a noisy profile. Fitting procedures give better results than smoothing procedures because smoothing flattens the profile and as a result $D_{x\text{-}(1\text{-}x)}$ will be increased. Another advantage of a fitting procedure is the possibility to get $D_{x\text{-}(1\text{-}x)}$ directly from the fitting program (e.g. Logistic Function Profile Fit [25]) or it can be calculated from the exponent of a logistic function (e.g. $D_{12\text{-}88} = 1.73/p$, where p is the exponent of the ORIGIN™ Dose Response Function). For that reason the accuracy of $D_{12\text{-}88}$ was determined by fitting simulated profiles with different sets of Gaussian noise. The accuracy of $D_{12\text{-}88}$ depends on signal-to-noise ratio $R_{S/N}$ as well as on the fit range on length scale and sampling step width. Here the effect of noise is only analysed for additive noise (cf. Figure 52). In this case, the signal-to-noise ratio $R_{S/N}$ is the ratio of the difference between the intensity plateaus to the standard deviation of noise. For shot noise (cf. Figure 52) the lower level of intensity may be zero without any noise. Therefore the accuracy of $D_{12\text{-}88}$ determined from an image profile with shot noise is higher than that determined from image profiles with additive noise at the same value of $R_{S/N}$. For three values of $R_{S/N}$ and different measurement conditions (cf. Figure 43) the accuracy of $D_{12\text{-}88}$ is given in Table 5.

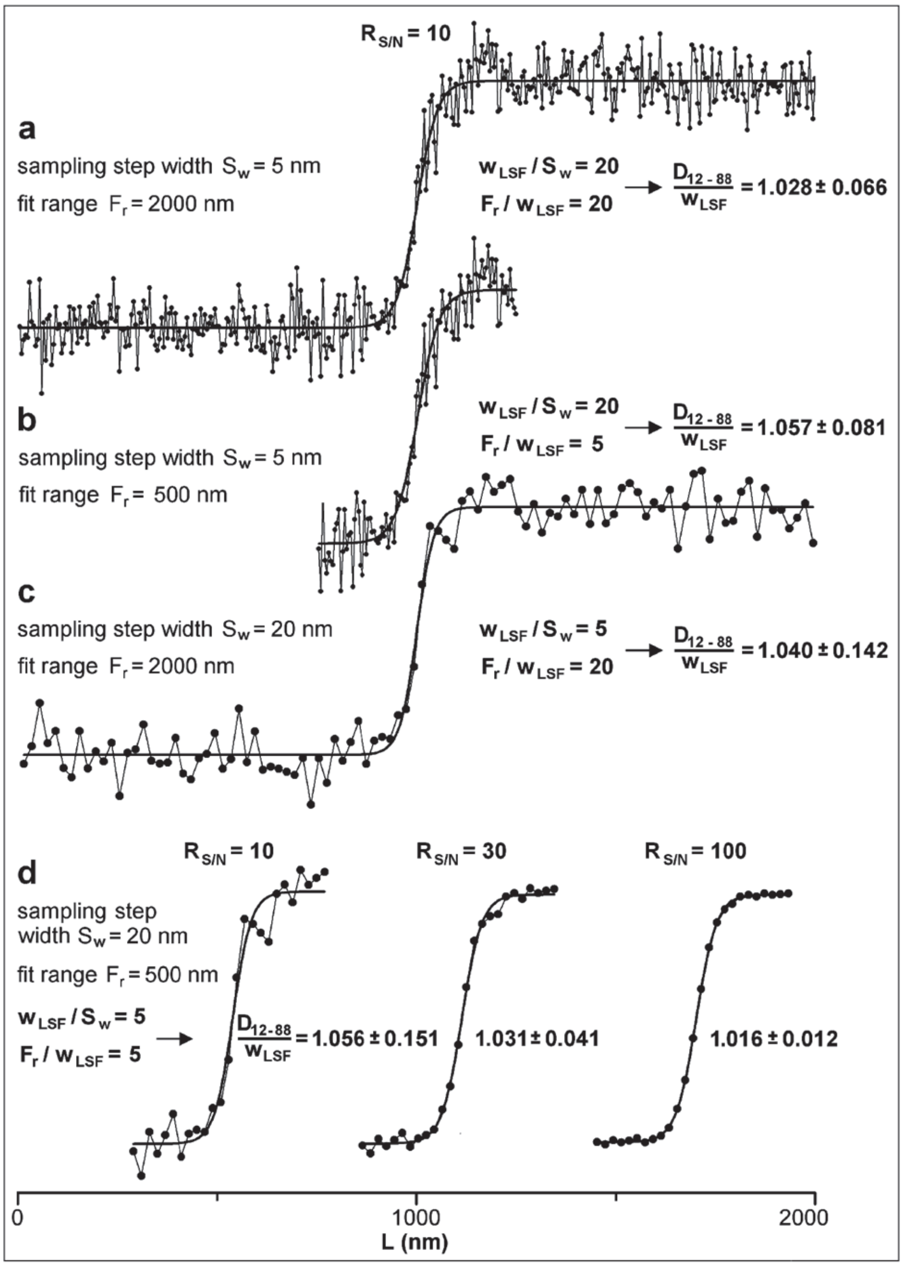

Figure 43 — Simulated determination of $D_{12\text{-}88}$ from a noisy profile over a chemical edge under different measurement conditions. The simulated profiles (black dots) were calculated by convolution of a step function (L_{pl} = 15 µm, cf. Figure 41, top) with a Gaussian LSF (w_{LSF} = 100 nm → $D_{12\text{-}88}$ = 100 nm) and the subsequent addition of Gaussian noise. $D_{12\text{-}88}$ was determined by a fit (bold line) with a logistic function. The measurement conditions written in thin letters are related to the given example (w_{LSF} = 100 nm) whereas the conditions and results written in bold letters are normalized to w_{LSF} and therefore valid for Gaussian LSFs of each width w_{LSF}. The values of $D_{12\text{-}88}/w_{\text{LSF}}$ are means and standard deviations of 20 values determined by fitting simulated profiles with different sets of noise (cf. Table 5)

Table 5 — Means and standard deviations of $D_{12\text{-}88}$ normalized to the halfwidth w_{LSF} of a Gaussian LSF. Each value has been calculated from 20 fits of simulated profiles which differ in the added Gaussian noise. The profiles were simulated by convolution of a step function (L_{pl} = 15 µm, cf. Figure 41, top) with a Gaussian LSF (w_{LSF} = 100 nm → $D_{12\text{-}88}$ = 100 nm) and the subsequent addition of different sets of Gaussian noise. The fits were done with the Logistic Function Profile Fit [25] which calculates the value $D_{12\text{-}88}$ automatically. Different measurement conditions with respect to samples per length (reciprocal of sampling step width S_{w}) and range of fitted samples F_{r} are shown in Figure 43

noise	samples	$D_{12\text{-}88}$ / w_{LSF}			
	per w_{LSF}	fit range		fit range	
$R_{\mathrm{S/N}}$	w_{LSF} / S_{w}	F_{r} / w_{LSF} = 5		F_{r} / w_{LSF} = 20	
		mean	st. dev.	mean	st. dev.
100	**5**	1.016	0.012	1.001	0.010
30	**5**	1.031	0.041	1.012	0.036
10	**5**	1.056	0.151	1.040	0.142
10	**20**	1.057	0.081	1.028	0.066

Table 5 shows that the mean value of $D_{12\text{-}88}$ increases with decreasing $R_{\mathrm{S/N}}$. This systematic overestimation of $D_{12\text{-}88}$ between 1.6 % ($R_{\mathrm{S/N}}$ = 100) and 5.7 % ($R_{\mathrm{S/N}}$ = 10) can be reduced by increasing the fit range from 5 w_{LSF} to 20 w_{LSF}, whereas a reduction of sampling step width has no significant effect. The standard deviation of $D_{12\text{-}88}$ can be halved by a reduction of the sampling step width whereas an increase of the fit range has no significant effect.

Measurement uncertainty of $D_{x\text{-}(1\text{-}x)}$

The measurement uncertainty is a measure of the accuracy of a measurement method. It combines systematic deviations (trueness) and random deviations (precision). If a systematic deviation of $D_{x\text{-}(1\text{-}x)}$ from its true value is known (e.g. from Figure 42), then the resulting value of $D_{x\text{-}(1\text{-}x)}$ can be corrected. Without such a correction the systematic deviation is part of measurement uncertainty as demonstrated below. Here $D_{12\text{-}88}$ is an example for all parameters $D_{x\text{-}(1\text{-}x)}$ taken from the ESF.

The combined relative measurement uncertainty of $D_{12\text{-}88}$ is calculated for two examples:

Ex1: Gaussian LSF, plateau length (L_{pl}/w$_{\mathrm{LSF}}$) = 3, $R_{\mathrm{S/N}}$ = 10, (samples per w$_{\mathrm{LSF}}$) = 20, fit range (F_{r}/w_{LSF}) = 5. This example is shown in Figure 43b.

Ex2: Lorentzian LSF, plateau length (L_{pl}/w_{LSF}) = 30, $R_{\mathrm{S/N}}$ = 100, (samples per w$_{\mathrm{LSF}}$) = 5.

$D_{12\text{-}88}$ has been determined directly from the profile as shown in Figure 41.

Systematic deviation

Systematic deviations of $D_{12\text{-}88}$ from its true value $(D_{12\text{-}88})_{\mathrm{t}}$ are caused by the finite length of the plateaus L_{pl} on both sides of the step transition (cf. Figures 41 and 42) and by the determination of $D_{12\text{-}88}$ from the fit (cf. Table 5).

Ex1: Deviation of $D_{12\text{-}88}$ by finite plateau length L_{pl}: $(\Delta D_{12\text{-}88})/(D_{12\text{-}88})_{\mathrm{t}}$ = + 3.7 % (from Figure 42a)

Deviation of $D_{12\text{-}88}$ by the fitting procedure: $(\Delta D_{12\text{-}88})/(D_{12\text{-}88})_{\mathrm{t}}$ = + 5.7 % (from Table 5)

Because both deviations are positive they have to be added linearly

→ Systematic deviation: $(\Delta D_{12\text{-}88})/(D_{12\text{-}88})_{\mathrm{t}}$ = 3.7 % + 5.7 % = 9.4 %.

Ex2: Deviation of $D_{12\text{-}88}$ by finite plateau length L_{pl}: $(\Delta D_{12\text{-}88})/(D_{12\text{-}88})_{\mathrm{t}}$ = −11 % (from Figure 42a).

Random deviation u_r

The uncertainty of $D_{12\text{-}88}$ depends on the measuring conditions, particularly on signal-to-noise ratio $R_{S/N}$, sampling step width and, if a fit has been performed, fit range. The uncertainty can be characterized by the standard deviation of $D_{12\text{-}88}$ determined by fitting a set of simulated profiles (Ex1, cf. Table 5) or at high $R_{S/N}$ by the estimated uncertainty of $D_{12\text{-}88}$ directly determined from the measured profile (Ex2).

Ex1: $u_r/(D_{12\text{-}88})_t = 8.1\ \%$ (from Table 5).

Ex2: $u_r/(D_{12\text{-}88})_t = 5\ \%$ (estimated maximum error)

For standard deviations it is used to give the expanded uncertainty, $U_r = k\ u_r$, given in Formula (26), where k is the coverage factor.[22] With $k = 2$ (level of confidence = 95 %) we get

Ex1: $U_r/(D_{12\text{-}88})_t = 16.2\ \%$.

Ex2: $U_r/(D_{12\text{-}88})_t = u_r/(D_{12\text{-}88})_t = 5\ \%$[7].

Combined uncertainty

According to the GUM approach[22] the quadratic addition of different components, here the systematic deviation and the random deviation, gives the combined uncertainty[8]

$$U_c = [U_r^2 + (\Delta D_{12\text{-}88})^2]^{½} \tag{31}$$

Then the relative combined uncertainties of w_{LSF} are:

Ex1: Gaussian LSF, $(L_{pl}/w_{LSF}) = 3$, $R_{S/N} = 10$, (samples per w_{LSF}) = 20, $(F_r/w_{LSF}) = 5$,

$$U_c/(D_{12\text{-}88})_t = [(16.2\ \%)^2 + (9.4\ \%)^2]^{½} = 18.7\ \%$$

Ex2: Lorentzian LSF, $(L_{pl}/w_{LSF}) = 30$, $R_{S/N} = 100$, (samples per w_{LSF}) = 5,

$$U_c/(D_{12\text{-}88})_t = [(5\ \%)^2 + (11\ \%)^2]^{½} = 12.1\ \%$$

The uncertainty of 18.7 % for example 1 is mainly due to the uncertainty of fitting a noisy profile. It can be reduced by a longer acquisition time which improves signal-to-noise ratio.

The uncertainty of 12.1 % for example 1 seems to be sufficient in most cases. It is mainly due to the limited length of the plateaus on both sides of the step transition which is the dominating source of deviation for long-tailed LSFs like the Lorentzian.

$D_{x\text{-}(1\text{-}x)}$ values of edge profiles measured with a short-tailed LSF (e.g. Gaussian) and a high signal-to-noise ratio have a lower uncertainty, whereas $D_{x\text{-}(1\text{-}x)}$ values of edge profiles measured with a long-tailed LSF (e.g. Lorentzian) and a low signal-to-noise ratio have a higher uncertainty than the given examples.

4.4 Determination of lateral resolution by imaging of square-wave gratings

Imaging of square-wave gratings is a method which enables a “real time” estimation of lateral resolution in the nanometre range without any numerical treatment of data as well as an accurate determination of lateral resolution by numerical methods (cf. 4.4.2.4 and 4.4.3.3). It is directly related to the primary definition of resolution, which refers to the “minimum spacing at which two features of the image can be recognised as distinct and separate”[3]. The stripes of a chemical square-wave grating are optimal for the determination of this minimum spacing.

---

[7] The estimated uncertainty $u_r / (D_{12\text{-}88})_t = 5\%$ for Ex2 is a maximum error and therefore it is not expanded.

[8] The coverage factor has to be applied only to the random components of uncertainty and therefore $\Delta D_{12\text{-}88}$ is not expanded.

4.4.1 Properties of square-wave gratings and their importance for the determination of lateral resolution

4.4.1.1 Number of stripes

In the mathematic theory, periodic functions are commonly thought to be infinitely extended. However a physical representation of periodic functions can be only given by gratings with a finite number of periods. Practically relevant gratings as a part of a test pattern for the determination of lateral resolution must be restricted to a small number of periods because it is rather useful to image simultaneously gratings with different periods. For square-wave gratings the effect of the number of stripes on lateral resolution by model calculations has been analysed. Figure 44 shows the simulated imaging of a 3-stripe grating (A-B-A), a 5-stripe grating and a 7-stripe grating all with a period of 200 nm and after convolution with Gaussian LSFs of different FWHM. For medium resolution (w_{LSF} = 100 nm) the image contrast c_i (cf. 4.1.5) does not depend on the number of stripes. Near the limit of resolution (w_{LSF} = 200 nm and 220 nm) the image contrast between the inner stripes of the 7-stripe grating is greater than the image contrast between the outer stripes.

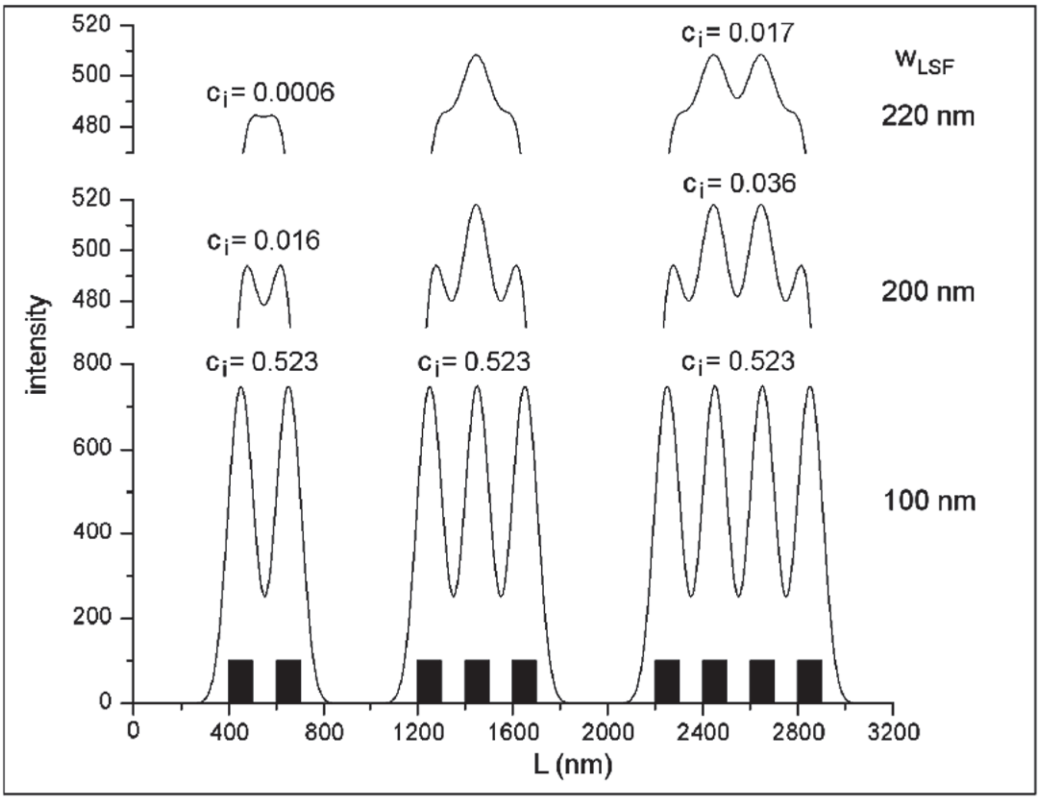

Figure 44 — Imaging of gratings (period 200 nm) with 3, 5 and 7 stripes, respectively. Imaging is simulated by convolution with Gaussian LSFs of different FWHM. The values of image contrast c_i (for definition, see Figure 46) are determined for the inner stripes. Note the 6 times expanded intensity scale for both image profiles in the upper part of the figure

This effect is due to the fact that the images of outer stripes are superimposed at the inner side only. In images of 3-stripe gratings, this superposition shifts the maxima of intensity together (Figure 44, left, middle and top and Annex A) and, as a consequence, the image contrast is smaller than that of gratings with at least 7 stripes. The image contrast of a 5-stripe grating is a special case because, near the limit of resolution, it cannot be determined (cf. situation given in Figure 44, middle, top).

From the practical point of view, 3-stripe gratings as given on the left in Figure 44 are the most suitable stripe patterns for the determination of lateral resolution, because they enable the simultaneous imaging of a maximum number of gratings within the field of view of the imaging instrument. Furthermore only

3-stripe gratings represent the “two features” said in the definition of image resolution. For that reason, all further evaluations are limited to 3-stripe gratings.

4.4.1.2 Stripe distance and grating period

In almost all definitions, the lateral resolution is defined as the “minimum spacing at which two features of the image can be recognised as distinct and separate”[3]. But the question arises as to what is meant by “spacing” in relation to square-wave gratings? In general, there are two possibilities to describe that spacing for a 3-stripe square-wave grating by using (i) the distance G (gap) between the inner edges of the outer stripes or (ii) the centre-to-centre distance between the outer stripes which is the grating period P. Figure 45 shows the effect of variations of G and P on the image of the respective grating. It is obvious that the variation of the grating period P at a fixed gap G strongly influences the lateral resolution of the grating image. The effect is visualized in Figure 45 by variations of the image contrast at medium resolution (w_{LSF} = 15 nm) and at the limit of resolution (w_{LSF} = 20 nm). On the other hand variation of the gap G at a fixed grating period P has only a small influence on resolution. Therefore, the grating period P expressed as the centre-to-centre distance between neighbouring stripes is the appropriate parameter of spacing to be used for the definition of the lateral resolution. All further simulations are made using square-wave gratings with a fixed ratio P/G = 2, i.e. black and white (gap) stripes are of the same width.

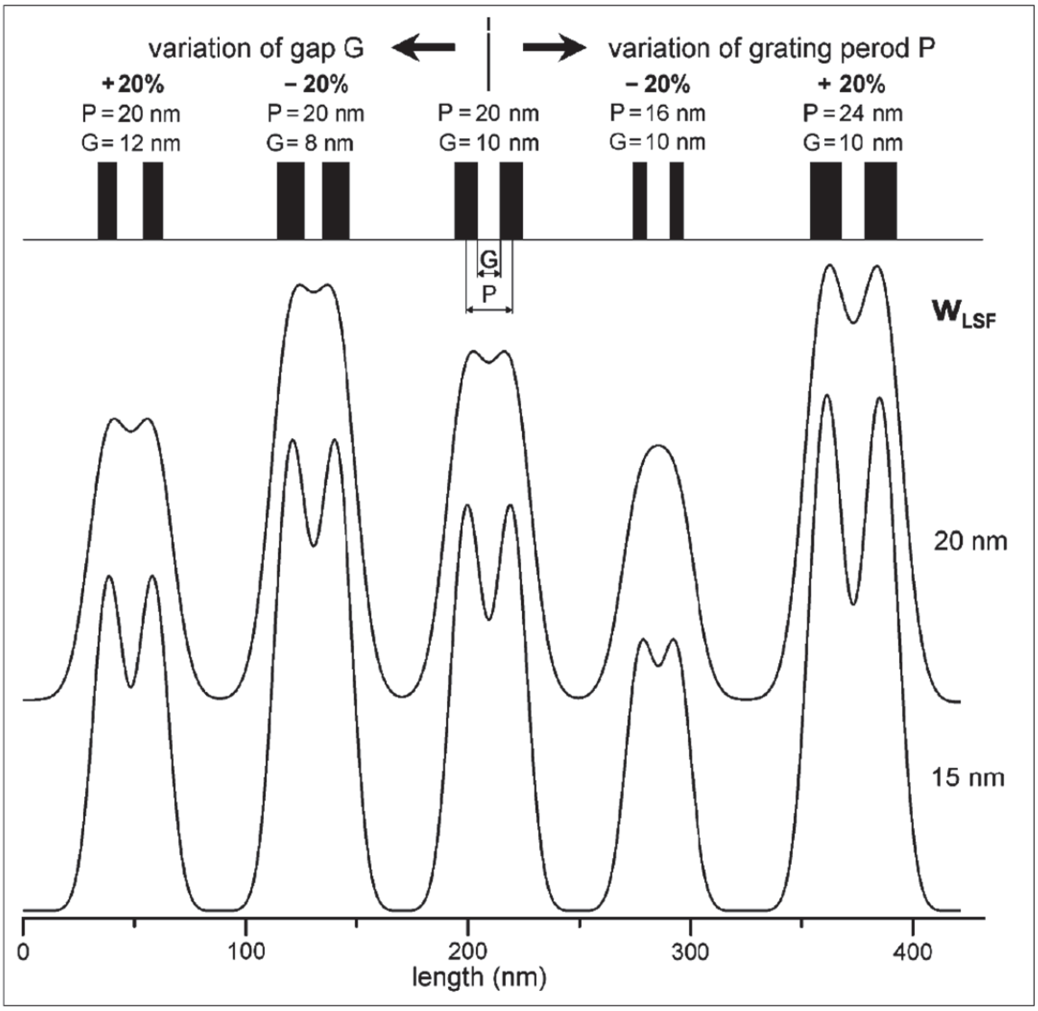

Figure 45 — The effect of gap G and grating period P on the lateral resolution of images of square-wave gratings. Imaging is simulated by convolution with Gaussian LSFs of different width w_{LSF}

4.4.1.3 Object contrast

The object contrast c_o of the imaged sample is determined both by the spatial variation of composition and/or other material properties of the sample (object pattern) and the imaging method applied. For instance the object contrast between $Al_{0.7}Ga_{0.3}As$ and GaAs is 100 % (c_o = 1) for Al mapping, or 70 % (c_o = 0.412) for Ga mapping by using SIMS and it is much smaller for mapping with a scanning electron microscope using secondary electrons.

Figure 46 demonstrates the effect of the object contrast c_o on the image contrast c_i and the contrast transfer function CTF = c_i / c_o as well. The image contrast is defined as $c_i = (I_{max} - I_{min})/(I_{max} + I_{min})$. Object contrast and image contrast are proportionally correlated. Correspondingly the CTF is not affected by object contrast variations. If noise is taken into consideration lateral resolution is determined by image contrast and noise (cf. 4.4.2.). Therefore object contrast also influences lateral resolution as is demonstrated in Figures 46 and 49. It can be shown that the object contrast relates to lateral resolution, represented by the effective cut-off frequency of the CTF (cf. 4.4.3.3).

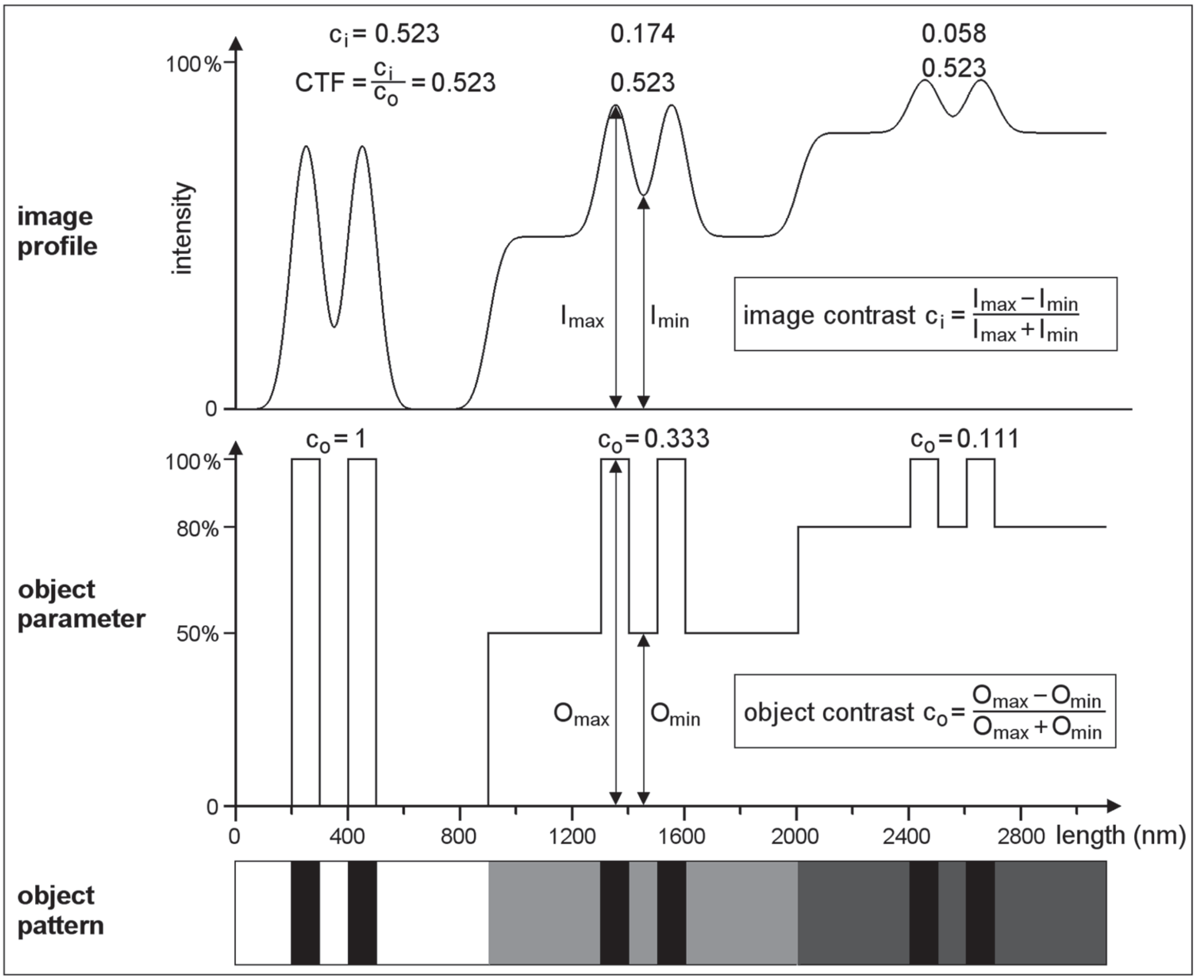

Figure 46 — The effect of object contrast c_o on image contrast c_i and contrast transfer function CTF. Imaging of square-wave gratings with a period of 200 nm is simulated by convolution with a Gaussian LSF (w_{LSF} = 100 nm)

The object contrast c_o between two regions of the test sample may be determined from the image. For sufficiently wide patterns c_o is identical to c_i and correspondingly c_o can be determined from two plateaus in the image as shown in Figure 47a.

If there is no upper plateau available, then the CTF can be determined from the relative image contrast $c_{i\,rel}$ as shown in Figure 47b. In this case the lower plateau I_{pll} is taken as baseline for the determination of $I_{\mathrm{min\ rel}}$ and $I_{\mathrm{max\ rel}}$. The shift of baseline increases the image contrast by a factor which corresponds to the reciprocal object contrast

$$c_{\mathrm{i\ rel}} = c_{\mathrm{i}}/c_{\mathrm{o}} = \mathrm{CTF} \tag{32}$$

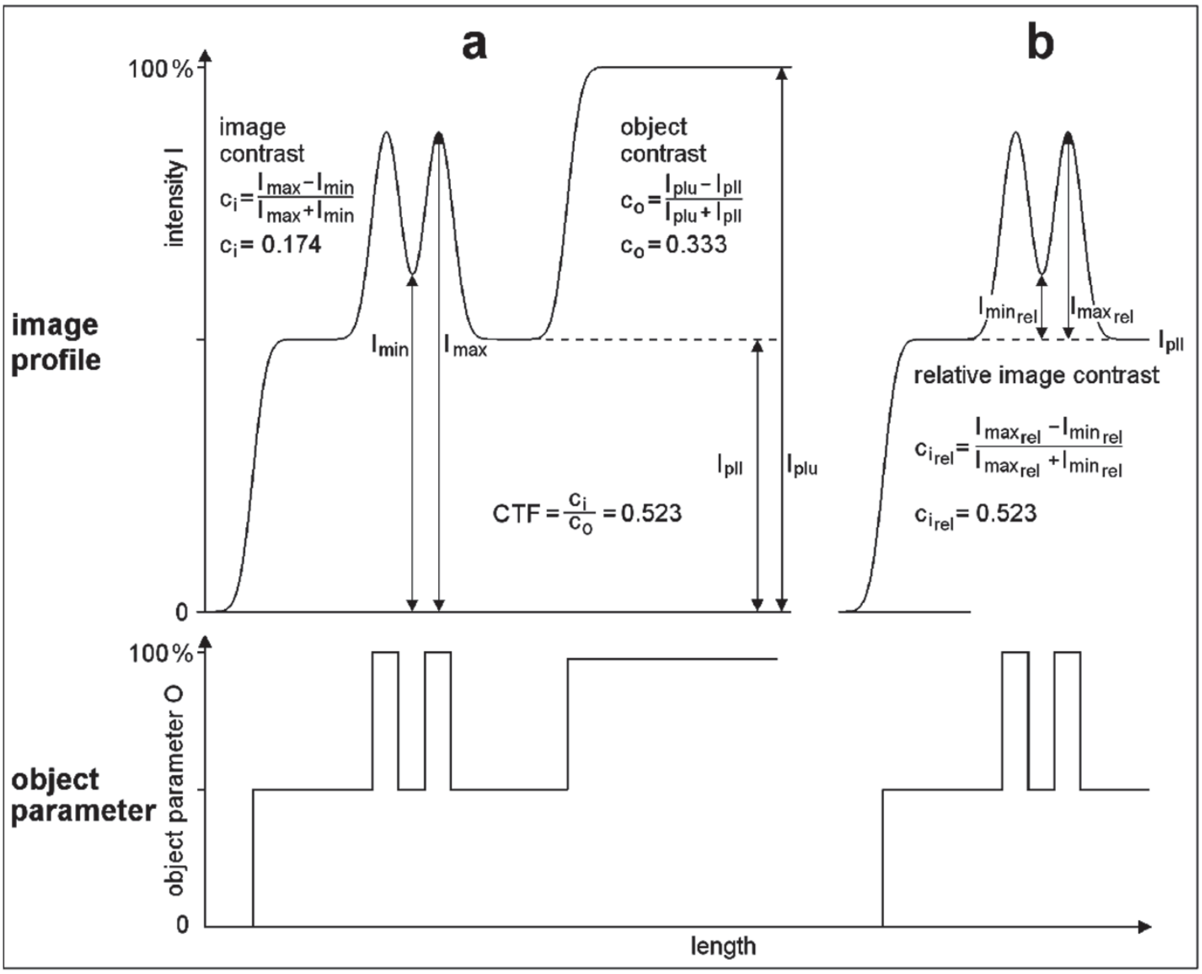

Figure 47 — Two possibilities for the determination of the CTF: a) Determination of object contrast c_{o} from the intensities of the upper plateau I_{plu} and the lower plateau I_{pll} and subsequent calculation of CTF = $c_{\mathrm{i}}/c_{\mathrm{o}}$. b) Determination of the relative image contrast $c_{\mathrm{i\ rel}}$ with respect to the lower plateau I_{pll}. $c_{\mathrm{i\ rel}}$ is equal to the CTF

4.4.2 The effect of noise on lateral resolution: The effective lateral resolution

Figure 48 shows an image of a series of six 3-stripe gratings taken by a Secondary Ion Mass Spectrometer (SIMS). Obviously, four gratings are resolved. The resolution criterion is the appearance of a dark stripe between two bright stripes. The resolution of the fifth grating may be prevented by noise but without a quantitative criterion it is difficult to decide whether the grating is resolved or not. For that reason it is necessary to consider the effect of noise quantitatively.

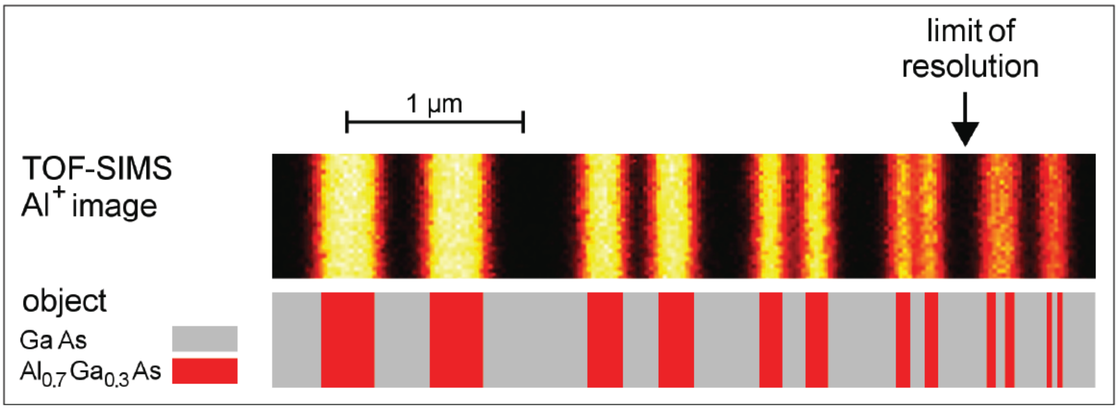

Figure 48 — The limit of resolution in a TOF-SIMS image of a series of square-wave gratings with different periods

The SIMS image in Figure 48 shows a high contrast between regions of the test sample's surface with and without aluminium. However there may be cases (other test samples, other imaging methods) where object and image contrast are not so high. For these cases contrast enhancement by image processing might be useful. Effects of contrast enhancement are demonstrated by simulations of imaging displayed in Figure 49. The image of the low contrast object in the second row of Figure 49 shows a very small contrast and correspondingly it is very difficult to decide whether or not individual stripes are resolved. The image contrast varies by 2 units of the 8-bit greyscale (0–255) for the narrow stripes and by 8 units for the wide stripes, respectively. After contrast enhancement these contrasts vary by 39 units for the narrow stripes and by 157 units for the wide stripes, respectively and all stripes are obviously resolved. This situation substantially changes if noise is added to the image. With increasing noise it is more and more difficult to resolve the stripes in the image. This holds true also for contrast enhanced images because noise is enhanced, too. The fact that at first the narrow stripes disappear in the noisy images clearly supports the assumption, that lateral resolution of an image is principally limited by the ratio of the intensity variation in the image and the level of noise. For that reason the lateral resolution which includes the effect of noise is called "effective lateral resolution" further on. The concept of effective lateral resolution is quite different from the traditional concept of image resolution, which is restricted to the properties of the imaging system and does not include effects of noise and object contrast.

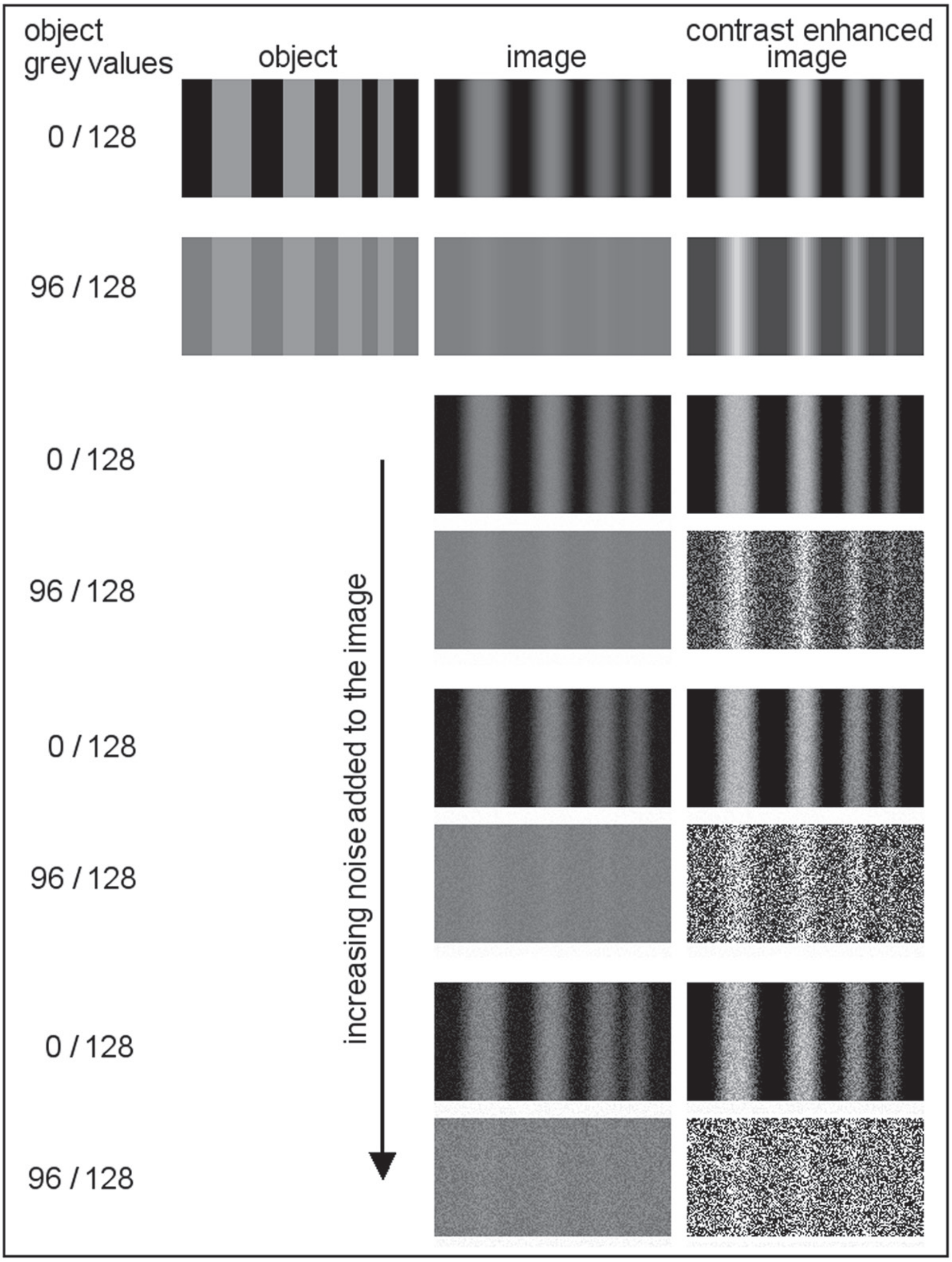

Figure 49 — The effect of noise and contrast on effective lateral resolution in images

Near the limit of resolution it is not always clear whether an image of a grating is resolved or not. In this case it is convenient to improve the signal to noise ratio. This may be done by increasing the recording time, but this is time consuming and possibly limited by the stability of the instrument parameters (drift). An improved signal to noise ratio makes it more easy to decide whether an image of a grating is resolved or not, but nevertheless an objective and quantitative resolution criterion is needed.

In the following paragraphs an option for a quantitative analysis of the image of a square-wave grating is undertaken. It is based on numerical simulations of linescans over 3-strip gratings (A-B-A, cf. 4.4.1.1) with a fixed ratio $P/G = 2$ (cf. 4.4.1.2).

Figure 50 shows image profiles (line scans) which are simulated by the convolution of a square-wave grating with a Gaussian line spread function (LSF). Figure 50a represents a case without noise where a very small dip appears between the two maxima. This small dip may be successfully increased by contrast enhancement leading to clearly resolved peaks. However, for a more realistic case with some noise on the profile (Figure 50b) contrast enhancement fails because the dip between the peaks and the amplitude of noise increase by the same factor. The conclusion is that the Dip-to-Noise Ratio (DNR) has to be considered as an issue limiting the lateral resolution.

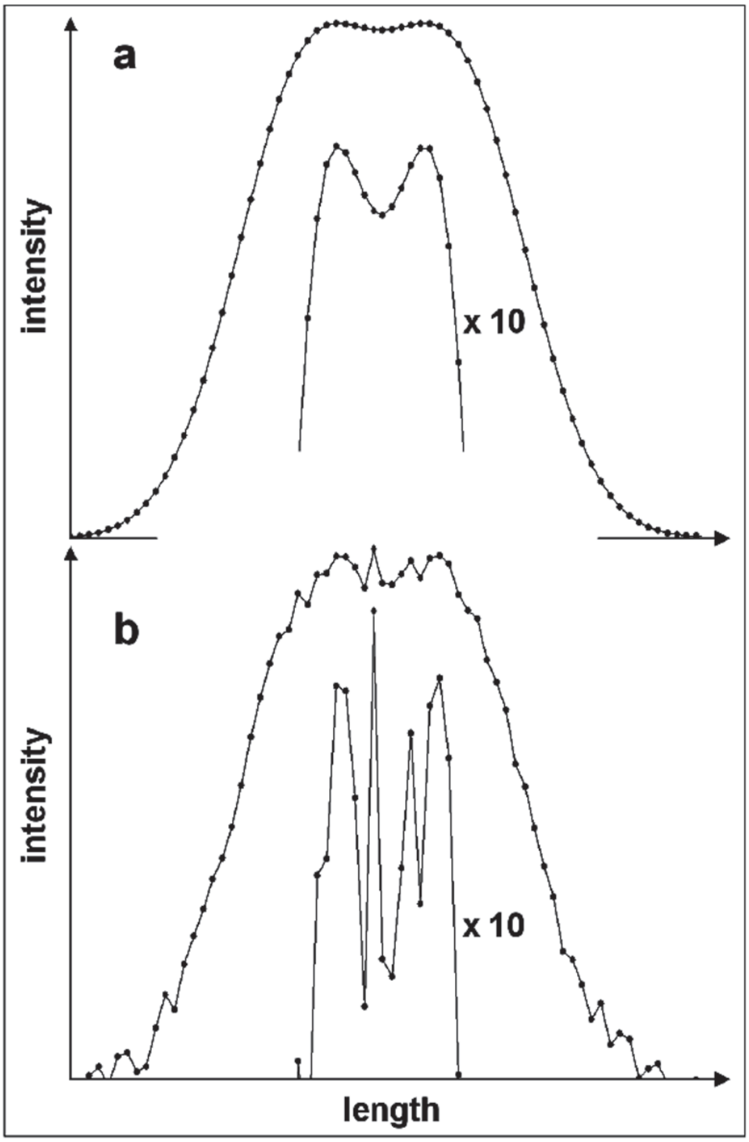

Figure 50 — Image profiles calculated by the convolution of a square-wave grating (period 48 nm) and a Gaussian (w_{LSF} = 50 nm): a) without noise; b) noise added to the calculated profile. A section of the profile is additionally shown on a stretched intensity scale. Contrast enhancement corresponds to a multiplication of intensity data by 10

4.4.2.1 Quantification of the dip

The dip D is the difference between the intensity of the maxima and the intensity of the minimum in between in a line scan across the image of the grating. In the presence of noise the dip D is defined as

$$D = [(I_{\text{max l}} + I_{\text{max r}})/2] - I_{\text{min}} \tag{33}$$

where $I_{\text{max l}}$, $I_{\text{max r}}$ and I_{min} are the signal intensities of the left maximum, the right maximum and the minimum in between, respectively. For a small number of sampling points per period S_{PP}, for instance only four, these values are to be taken directly from the measured line scan (Figure 51a).

$I_{\text{max l}}$, $I_{\text{max r}}$ and I_{min} may be obtained by averaging over a selected range of the length scale (Figure 51b). At first the regions for averaging must be defined. Because all stripes of the imaged grating have the same width it makes sense to set up both maximum regions symmetrically to the minimum region. The width of the three regions must be appropriately selected with careful consideration of the period of the image profile and the strength of the noise. It must be wide enough to reduce the effect of noise by averaging and it must be narrow enough that averaging does not reduce the dip artificially. Therefore it must be assumed that the widths of the maximum and minimum regions should not exceed one-third of the period in the image. In a second step the median values $I_{\text{max l}}$, $I_{\text{max r}}$ and I_{min} will be determined for each of the three intervals. The median is less sensitive to outliers than the arithmetic mean and therefore the effect of noise on the values $I_{\text{max l}}$, $I_{\text{max r}}$ and I_{min} is handled more appropriately.

Another possibility to determine $I_{\text{max l}}$, $I_{\text{max r}}$ and I_{min} and subsequently D is to smooth the whole line scan (Figure 51c). Different smoothing procedures may be applied. Savitzky-Golay smoothing is favourable for smoothing of noisy profiles, because it conserves the shape of the profile, characterized by the dip D, better than adjacent averaging smoothing and FFT filter smoothing. To prevent a flattening of the profile and a reduction of DNR an upper limit of smoothing points $n_{\text{max}} = S_{\text{PP}}$ is recommended.

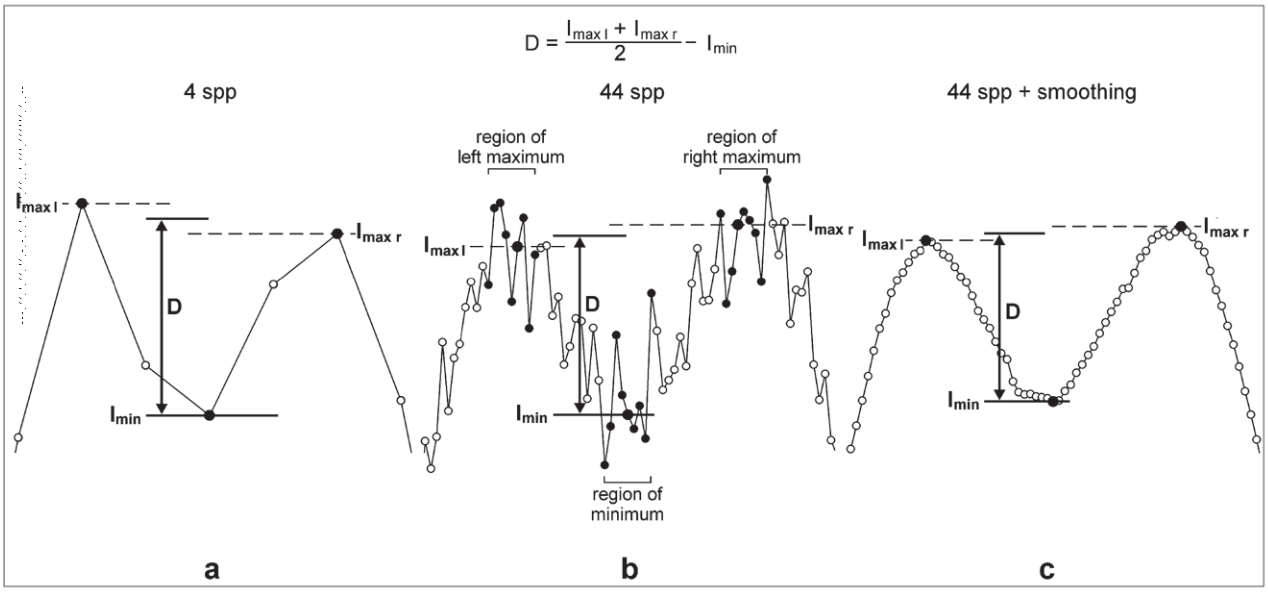

Figure 51 — Different methods for the determination of dip D. All examples were calculated by the convolution of a square-wave grating (period 48 nm) and a Gaussian (w_{LSF} = 40 nm) with subsequent addition of noise ($R_{\text{S/N}}$ = 25). a) Direct determination of $I_{\text{max l}}$, $I_{\text{max r}}$ and I_{min} for small values of sampling points per period S_{PP} (here 4 spp)[9]. b) $I_{\text{max l}}$, $I_{\text{max r}}$ and I_{min} calculated as medians (large black dots) from regions with 9 data points represented by black dots each. c) Noise of b) was reduced by Savitzky-Golay smoothing over 21 points. Subsequently the values $I_{\text{max l}}$, $I_{\text{max r}}$ and I_{min} have been determined.

---

[9] spp is the dimension unit of the variable S_{PP}.

4.4.2.2 Quantification of noise and noise reduction

We have stated before (cf. 4.4.2), that the dip-to-noise ratio is limiting the lateral resolution. Therefore a quantitative measure of noise is needed. According to the definition of noise (cf. terms and definitions) noise can be quantified by its standard deviation σ_N (N for noise).

The noise in a line scan across the image of a grating is composed of components with different characteristics:

— Additive noise, often called dark noise, is independent from signal intensity (Figure 52, top).

— The stochastic nature of particle counting causes so called shot noise (Figure 52, middle). This scatter of values can be described by the Poisson distribution and the corresponding standard deviation is equal to the square root of signal intensity.

— Fluctuations of the primary beam and mechanical instabilities of parts of the instrument cause noise which is proportional to signal intensity.

Often signals are superimposed by different types of noise (Figure 52, bottom). If the appearance of intensity dependent noise cannot be excluded it is necessary to determine the standard deviation of noise at a level of intensity which corresponds to the peak intensity of the two stripes.

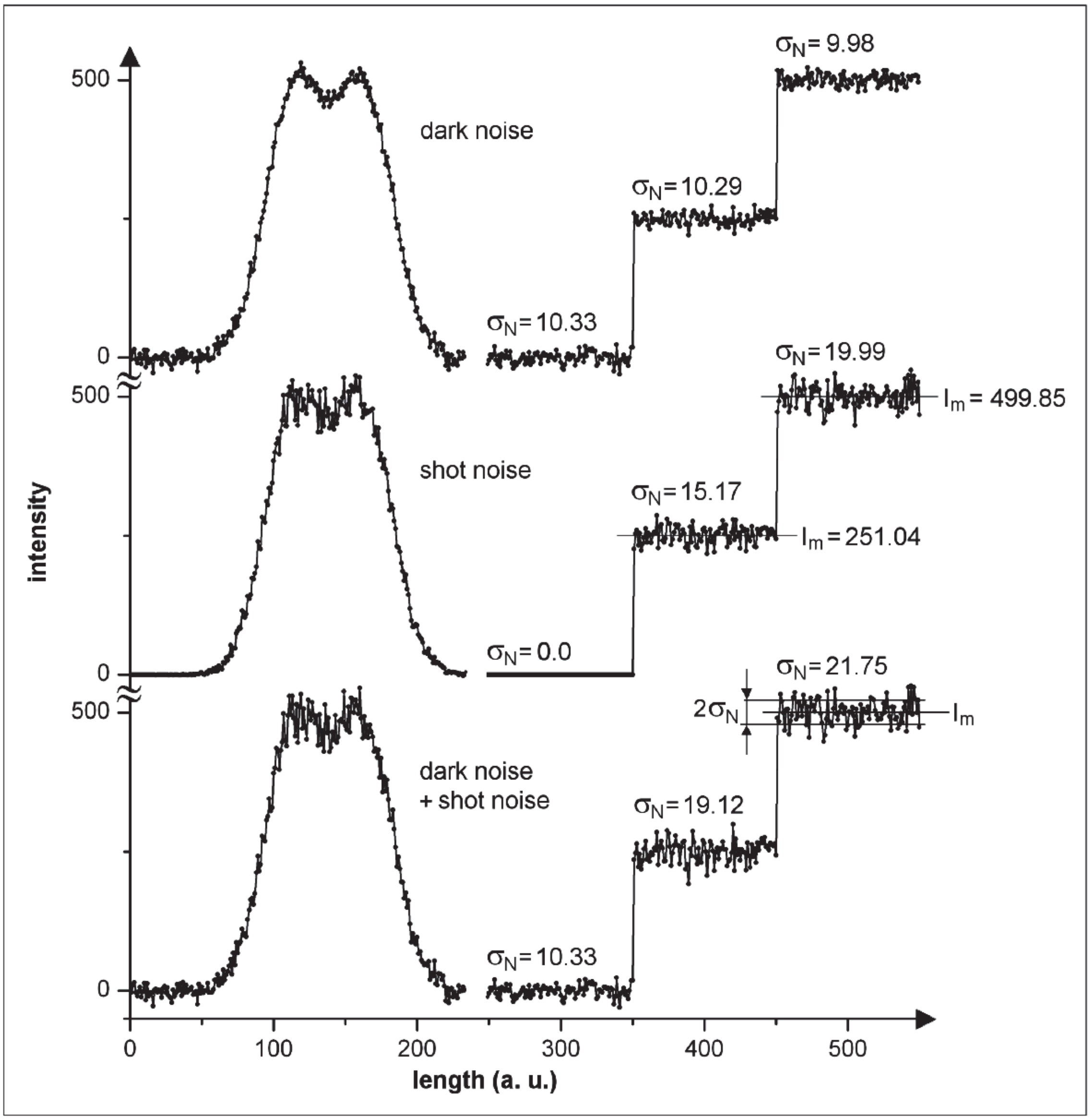

Figure 52 — Dark noise and shot noise on a simulated image profile over a square wave grating (left) and at different levels of mean signal intensity I_m (right). The noise was generated with random numbers from a normal (Gaussian) distribution. The standard deviations of noise σ_N are calculated for intervals with 100 values

Total noise may be quantified in a region of the image without any image structures where the standard deviation of signal intensity is determined by noise only. If noise is normally distributed (Gaussian noise), then about 68 % of the intensity values in the selected region are within the $2\sigma_N$ interval. This is true only for an infinite number of measured values. In practice the standard deviation of noise must be determined from a finite number n of values. Figure 53 shows the statistical spread of σ_{Nn} for intervals with $n = 30$ samples. It reflects the uncertainty of σ_{Nn} which may be characterized by the standard deviation σ_n of σ_{Nn}. This standard deviation decreases with an increasing number of samples n within the analysed interval. Figure 54 shows, that the standard deviation σ_n of σ_{Nn} is inversely proportional to $n^{1/2}$, where n is the number of values per interval. The scatter of values around the straight line reflects the limited number of intervals for which σ_n of σ_{Nn} was calculated. From Figure 54 the minimum number n of samples within the analysed interval can be determined if a certain accuracy for σ_{Nn} is required. For a standard deviation < 10 %, the value of σ_N must be determined from at least 40 samples.

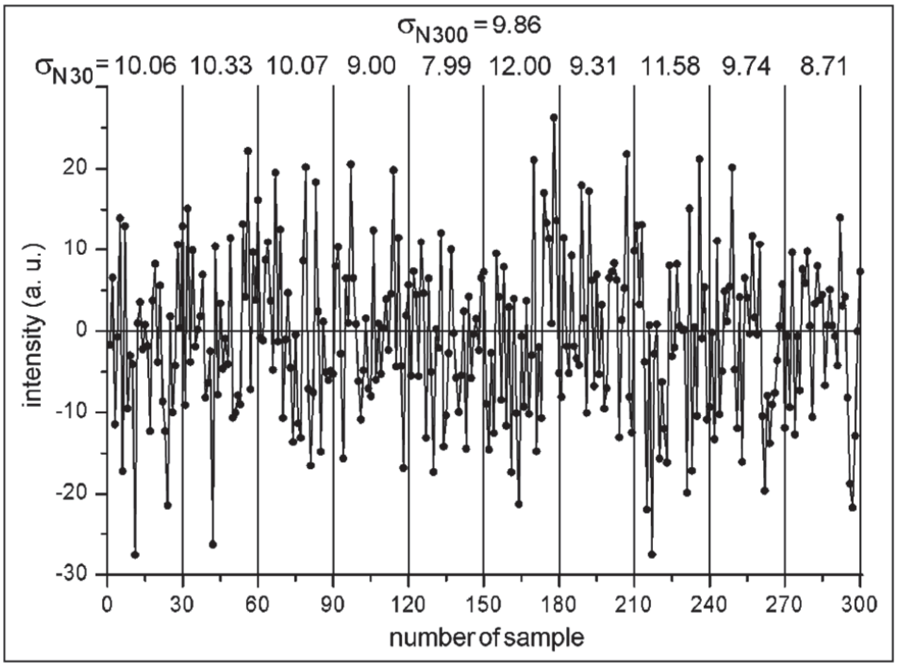

Figure 53 — The variation of σ_N for intervals with n = 30 samples

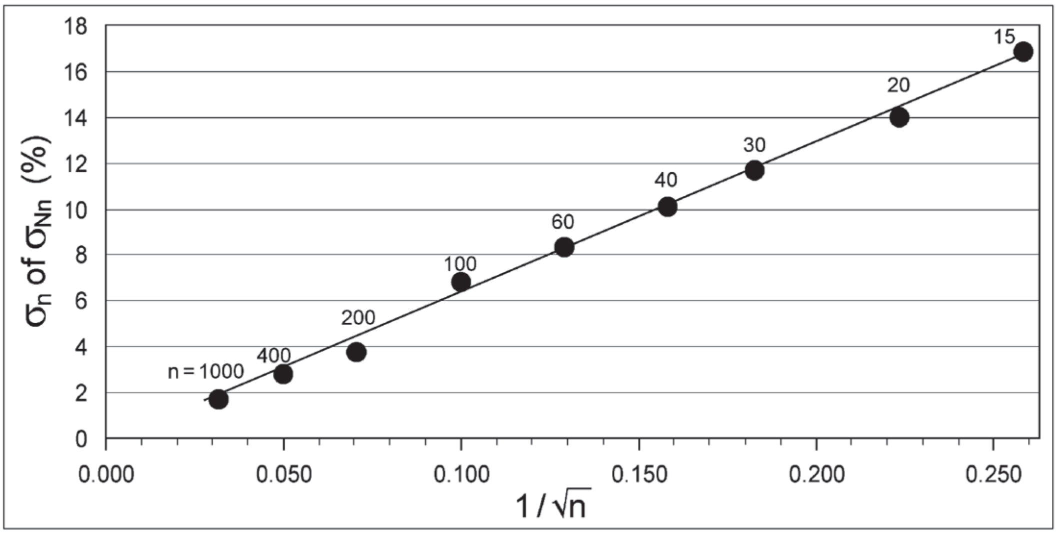

Figure 54 — The relative standard deviation σ_n of σ_{Nn} as a function of the number of samples n per interval. σ_n (%) = ($\sigma_n/\sigma_{N\infty}$) × 100

Using the quantitative definition of the dip D in a line scan across the image of a grating **[**Formula (33)], the dip to noise ratio is defined as

$$D/\sigma_N = [(I_{\max\,l} + I_{\max\,r})/2 - I_{\min}]/\sigma_N \tag{34}$$

where σ_N is the standard deviation of noise. However this definition suffers from the fact that the number of sampling points per period has to be considered, too. A large number of sampling points per period S_{PP} allows the summation over neighbouring sampling points (channel pooling) and therewith a reduction of noise. The summation over n sampling points, which corresponds to an n-fold increase of the width of the measuring channel, leads to an increase of $R_{S/N}$ and D/σ_N by a factor of $n^{1/2}$. This possibility for improving D/σ_N can be taken into account by replacing σ_N by the standard deviation of the reduced noise[26]

$$\sigma_{NR} = (4/S_{PP})^{1/2}\sigma_N \tag{35}$$

The number 4 is an estimate of the minimum S_{PP} for a reasonable determination of D as demonstrated in 4.4.3.4. At 4 spp the deviation of D due to the phase mismatch between sampling points and a noise-free imaged grating profile is smaller than 30 % (cf. Figure 66).

The reduction of noise by the summation over sampling points is demonstrated in Figure 55. Summation over 11 sampling points and subsequent division by 11 reduces σ_N by a factor of 3.67 which is close to the predicted value $11^{1/2} = 3.32$, whereas D is only slightly changed. As a result D/σ_N increases considerably and the resolution is improved. For comparison the same profile sampled with 4 spp is shown (Figure 55, right). The profile is strongly influenced by noise and therefore the values of D vary over a wide range. In the given example both values of D/σ_N are greater than the corresponding values in the 44 spp profile. Nevertheless the visual impression of resolution is better in the 44 spp profile, where the two stripes of the grating are clearly separated whereas in the 4 spp profile the dip between the stripes could be caused by noise. This result confirms that the ratio of dip to reduced noise, given by

$$R_{D/RN} = D/\sigma_{NR} = D/\left(\sigma_N\left(4/S_{PP}\right)^{1/2}\right) \tag{36}$$

is the right value for the decision whether the stripes of a square-wave grating are separated and therewith resolved or not. Calculation of reduced noise by taking into account the number of sampling points per period reflects the potential of noise reduction. As a consequence it is not necessary to carry out an averaging procedure, because numerical treatment does not increase the information content of a measured grating profile.

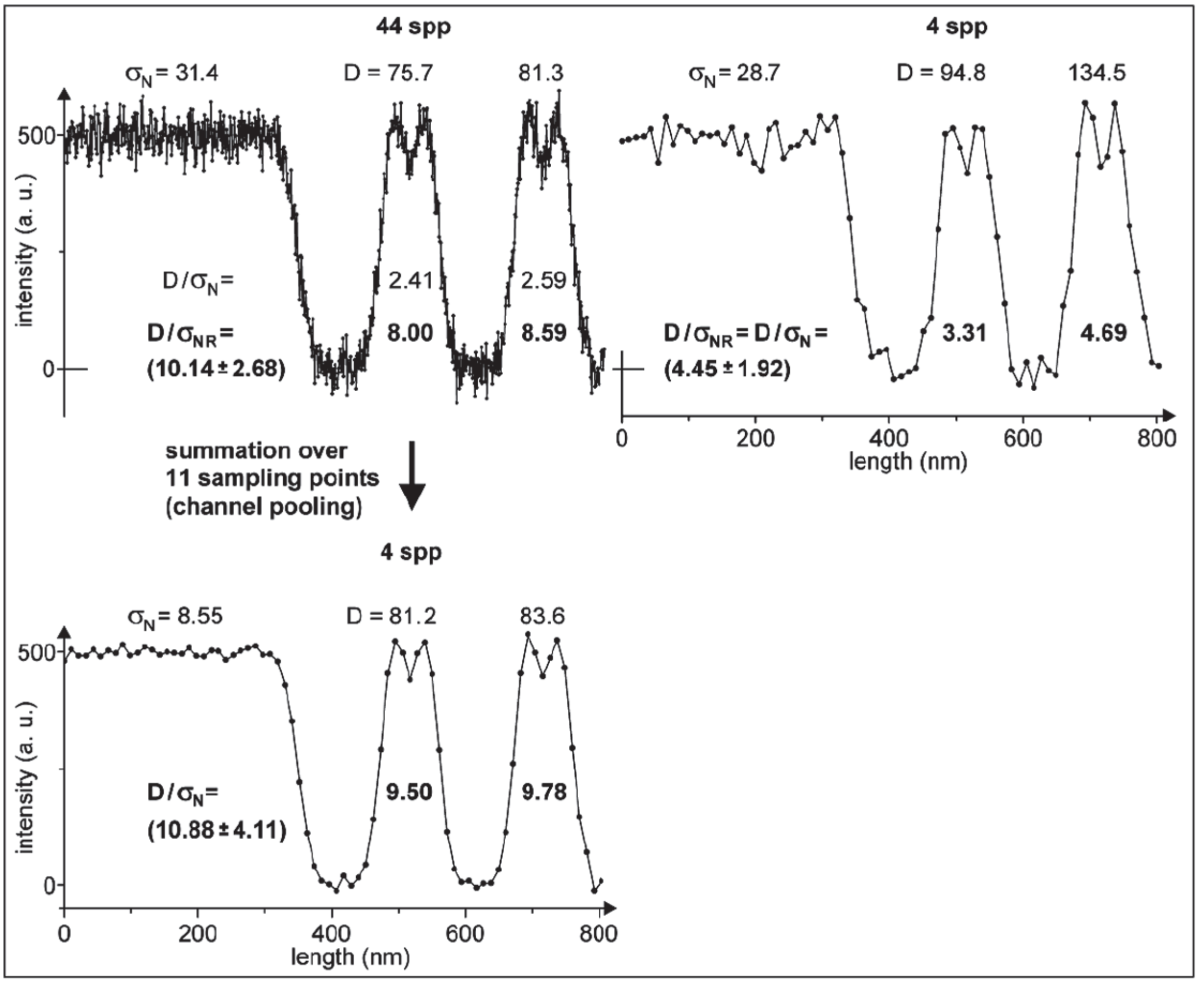

Figure 55 — The effect of the number of sampling points per period S_{PP} on the dip to noise ratios D/σ_N and D/σ_{NR}. The profiles were simulated by convolution of two square-wave gratings (period 48 nm) with a Gaussian LSF (w_{LSF} = 40 nm) and subsequent addition of Gaussian noise ($R_{S/N}$ = 17). σ_N was calculated from 300 values (44 spp) and 28 values (4 spp), respectively. D was calculated from medians over 11 values (44 spp), according to Figure 51 b), and single values (4 spp), according to Figure 51 a), respectively. The values in parenthesis are mean values and standard deviations calculated from 6 grating profiles with different sets of noise

4.4.2.3 Definition of a dip-to-noise ratio based resolution criterion

The definition of a resolution criterion using line scans across the image of square-wave gratings utilizing the ratio of the dip to the reduced noise is somewhat arbitrary because it depends on the required statistical significance. Nevertheless the criterion must set a threshold high enough to separate noise-induced intensity variations from those which are related to the square-wave grating of the object pattern. Therefore a new resolution criterion[26] based on the ratio of dip D to reduced noise σ_{NR} is proposed

$$R_{D/RN} = D/\sigma_{NR} \geq 4 \tag{37}$$

The value 4 was chosen because pure Gaussian noise sometimes shows “dips” which exceed $3\sigma_{NR}$. The given criterion is close to the Rose criterion which states that an object is readily detectable if the corresponding signal difference is at least 5 times the noise.[27] In electron microscopy the Rose criterion was defined as “condition for an average observer to be able to distinguish small features in the presence of noise, which requires that the change in signal for the feature should exceeds the noise by a factor of at least three”[3]. Threshold values of 4 σ_N[28] and 5 σ_N[29] were used in transmission electron microscopy and 3 σ_N in light microscopy,[30] respectively.

The utility of the resolution criterion was tested with simulated line scans of square-wave gratings of different periods. The resulting line scans were superimposed with different levels of additive noise. Furthermore the sampling step width and therefore the number of sampling points per period was varied (cf. Figure 56). Using the criterion $R_{D/RN} \geq 4$, 13 from a total of 18 grating images displayed in Figure 56 can be considered to resolve the grating.

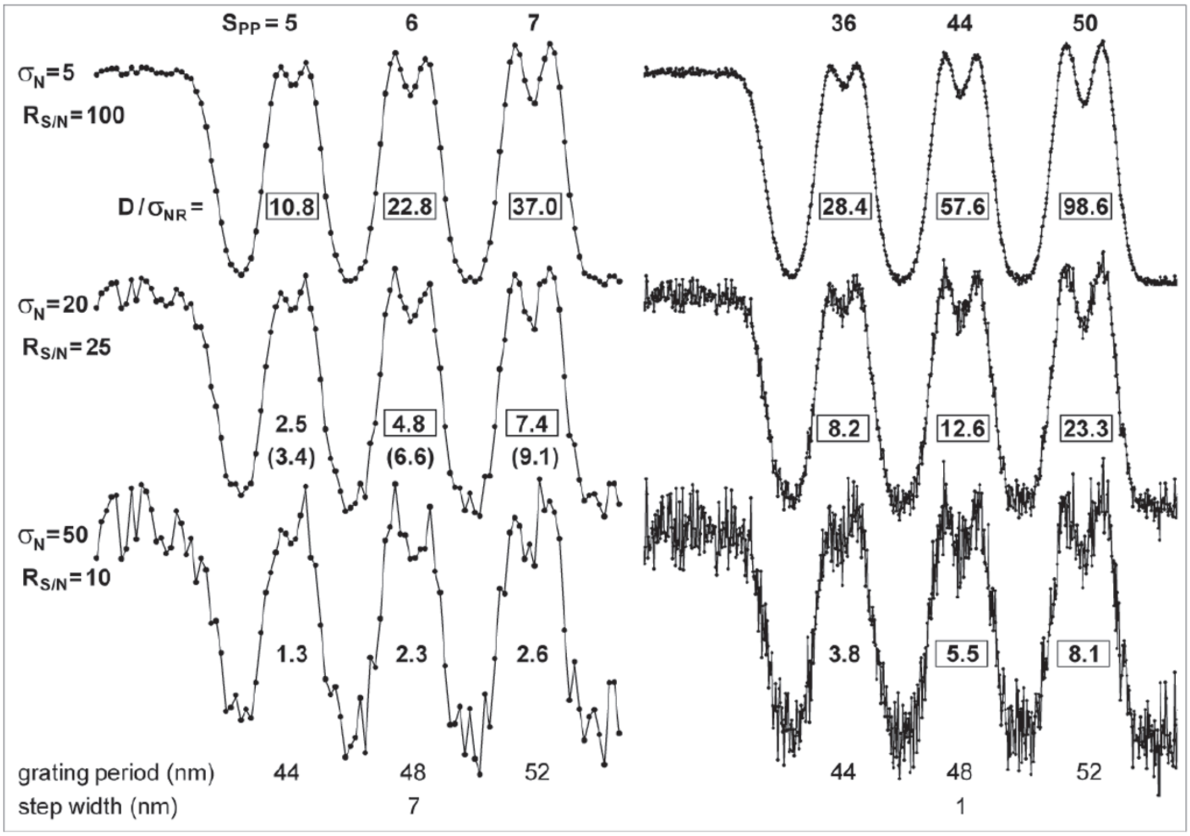

Figure 56 — Line scans calculated by the convolution of square-wave gratings with periods of 44 nm, 48 nm and 52 nm, respectively and a Gaussian with a FWHM of 40 nm. The sampling step width is 7 nm (left) and 1 nm (right), respectively. The number of sampling points per period S_{PP} given on top is related to the image period which is somewhat smaller than the original grating period for 3-stripe gratings (cf. 4.4.1.1 and Annex A). The added noise was generated with random numbers from a normal (Gaussian) distribution. Its standard deviation σ_N and the corresponding signal-to-noise ratio $R_{S/N}$ are given at the left. For each imaged grating $R_{D/RN}$ according to Formula (36) is given. For the upper left line scan and for the values given in brackets (middle left) the dip D was determined according to Figure 51 a). For the middle and bottom line scans on the left side D was determined from medians over 2 points according to Figure 51 b). For the right set of line scans the dip was determined from medians over 7 points (top), 9 points (middle) and 11 points (bottom), respectively [cf. Figure 51 b)]. The framed values of $R_{D/RN}$ are above the resolution threshold $R_{D/RN} = 4$

4.4.2.4 Determination of effective lateral resolution by a combination of interpolation and extrapolation

The simplest method for the determination of effective lateral resolution r_e from an image or an image profile is to take the period P_1 of the finest resolved grating as the value of effective lateral resolution

$$r_e = P_1 \tag{38}$$

The accuracy of this method may be sufficient if the test sample has a series of very fine graded gratings. For grading factors $q = P_{n+1}/P_n > 1.2$ the accuracy of this method is not sufficient for most purposes (cf. Figure 67).

According to the criterion (Formula 37) the effective lateral resolution is equal to the grating period P which corresponds to $R_{D/RN} = 4$. Therefore the intersection of the curves $R_{D/RN}$ (P) and $R_{D/RN} = 4$ correspond to the value of effective lateral resolution r_e. The curve $R_{D/RN}$ (P) has a sigmoid shape (cf. Figure 57 b) and therefore linear interpolation between the period of the finest resolved grating P_1 and the period of the first non-resolved grating P_0 may give no satisfying result. In most cases the interpolated value P_{int} is smaller than r_e, in particular if P_0 is much smaller than r_e (cf. Table 6).

Linear extrapolation of the straight line between the periods P_1 of the first resolved grating and P_2 of the second resolved grating to the line $R_{D/RN} = 4$ gives an intersection at P_{ext}. In most cases the value of P_{ext} is larger than the effective lateral resolution r_e (cf. Table 6), because the slope of the straight line P_1-P_2 is larger than that of P_0-P_1 (cf. Figure 57 b).

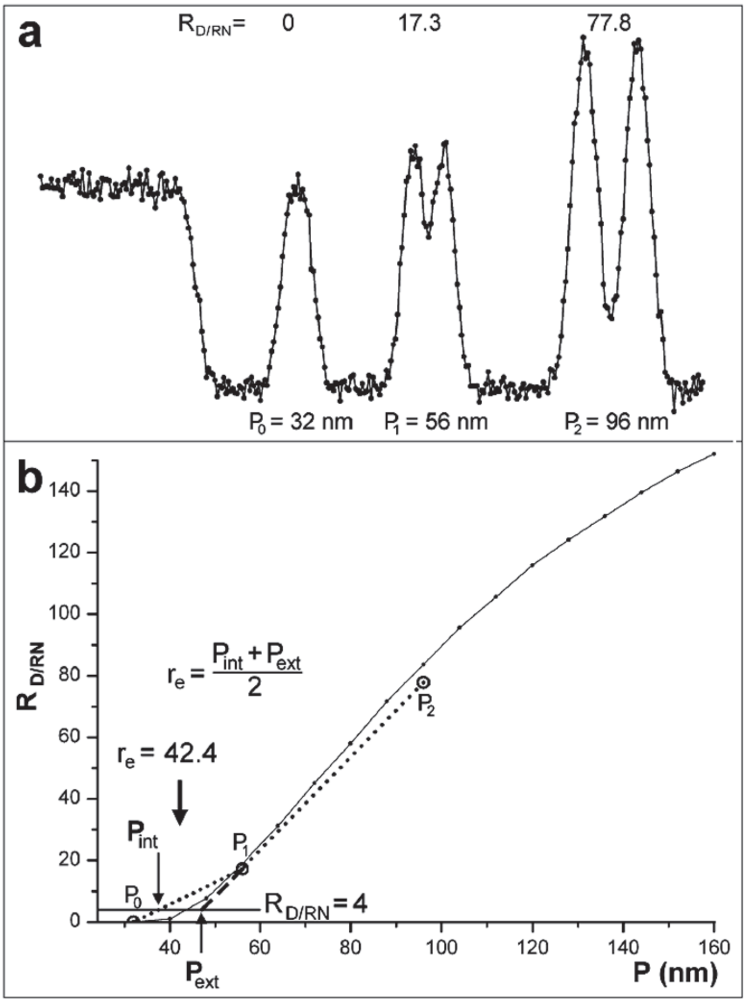

Figure 57 — a) Simulated line scans over a series of gratings with different periods. P_0 is the period of the largest non-resolved grating. P_1 and P_2 are the periods of the first and second resolved grating, respectively. The line scan was simulated by convolution of 3 square-wave gratings with a Gaussian LSF (w_{LSF} = 40 nm) and the subsequent addition of Gaussian noise ($R_{S/N}$ = 25). The sampling step width is 4 nm. The dip-to-reduced-noise ratios $R_{D/RN}$ have been calculated according to Formula (36). b) Determination of lateral resolution r_e by interpolation (P_{int}) and extrapolation (dashed line to P_{ext}) to $R_{D/RN}$ = 4. The small dots connected by a thin line correspond to the ideal values of $R_{D/RN}(P)$ without the effect of noise on the determination of the dip *D*. The open circles are data points $(P, R_{D/RN})$ corresponding to the three gratings shown in Figure 57 a). The deviations of $R_{D/RN}$ (P_1) and $R_{D/RN}$ (P_2) from the ideal curve are due to a slight reduction of the dip *D* by the calculation of medians according to Figure 51 b).

The tendencies of underestimation of r_e by interpolation and overestimation of r_e by extrapolation partly compensate each other if r_e is calculated from the arithmetic mean

$$r_e = \left(P_{int} + P_{ext}\right)/2 = P_1 - ½\left(R_1 - 4\right)\left[\left(P_1 - P_0\right)/\left(R_1 - R_0\right) + \left(P_2 - P_1\right)/\left(R_2 - R_1\right)\right] \quad (39)$$

For the sake of simplicity $R_{D/RN}$ is represented by R in Formula (39). It is an important criterion for the usefulness of a calculation method that the calculated value of effective lateral resolution is to a large extent independent from the grating periods P_0, P_1 and P_2 of the test sample. Table 6 shows the effective lateral resolutions calculated from simulated linescans over six series of gratings with very different periods. For series 1 to 4 the calculated values of r_e differ less than 5 % from the true value. This shows that the results of Formula (39) are nearly independent on a shift of grating periods and a slight increase of the grading factor. The strong deviations of r_e calculated from series 5 and 6 are due to the large differences $P_0 - P_1$ and $P_1 - P_2$ which lead to strong deviations of P_{int} (series 5) and P_{ext} (series 6) from $\mathrm{r_e}$, respectively. The effect of the small slopes at both sides of the sigmoid function $R_{\mathrm{D/RN}}$ (P) can be avoided if P_0 is not too small and P_2 is not to large. Therefore the application of Formula (39) is recommended for test samples with a grading factor

$$q \leq 1.8 \tag{40}$$

Table 6 — Calculation of effective lateral resolution r_{e} from simulated linescans. r_{e} has been calculated according to Formula (39) from series of gratings which differ in their periods P_0, P_1, and P_2. Series 3 corresponds to the line scan shown in Figure 57a. The simulated measurement conditions for all linescans are the same: Gaussian LSF with w_{LSF} = 40 nm, $R_{\mathrm{S/N}}$ = 25 and sampling step width S_{w} = 4 nm. Δr_{e} is the deviation of r_{e} from its true value 44.2 nm which was calculated from Table 8. Δr_{e} does not include the uncertainties caused by the uncertainties of grating periods P and dip-to-reduced-noise ratios $R_{\mathrm{D/RN}}$ (cf. 4.4.4).

series	grad. factor	grating periods			calculated values			true value	deviation	
of	$q = P_{n+1}/P_n$	P_0	P_1	P_2	P_{int}	P_{ext}	$r_e = (P_{\mathrm{int}} + P_{\mathrm{ext}}) / 2$	r_e	Δr_e	Δr_e
gratings		nm	nm	nm	nm	nm	nm	nm	nm	%
ser. 1	1.5	32	48	72	41.1	46.0	**43.6**	44.2	-0.7	**-1.47**
ser. 2	≈1.4	40	56	78	42.7	46.9	**44.8**	44.2	0.6	**1.32**
ser. 3	≈1.7	32	56	96	37.6	47.2	**42.4**	44.2	-1.8	**-4.07**
ser. 4	≈1.8	40	72	128	42.4	44.3	**43.4**	44.2	-0.9	**-1.92**
ser. 5	2	32	64	128	36.1	44.7	**40.4**	44.2	-3.8	**-8.60**
ser. 6	2	40	80	160	42.2	33.1	**37.7**	44.2	-6.6	**-14.82**

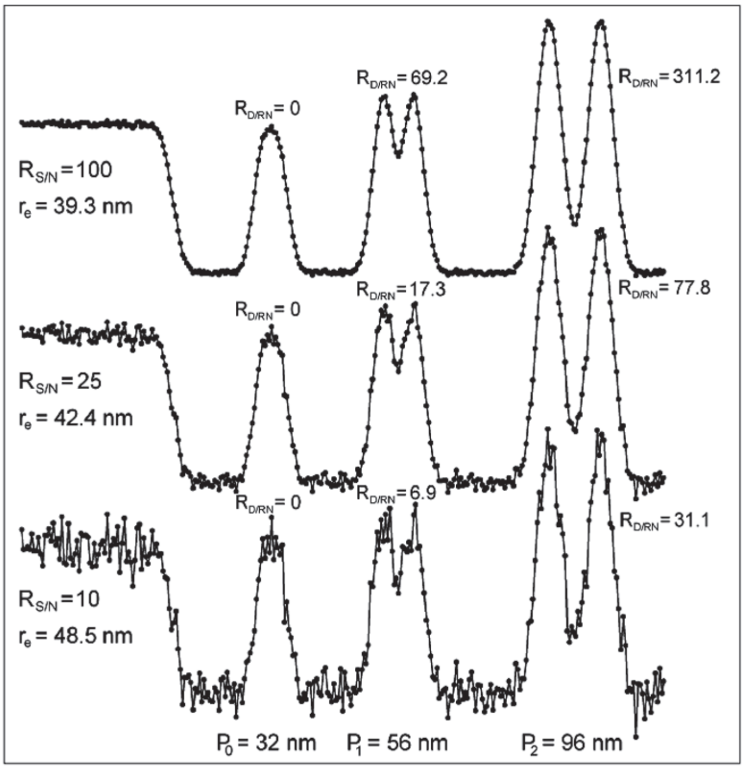

Figure 58 — Simulated line scans over the same series of gratings with different signal-to-noise ratios $R_{S/N}$. P_0 is the period of the largest non-resolved grating and P_1 and P_2 are the periods of the first and second resolved grating, respectively. The line scans have been simulated by convolution of a series of square-wave grating with a Gaussian LSF with w_{LSF} = 40 nm and the subsequent addition of Gaussian noise. The sampling step width is 4 nm. Dip-to-reduced-noise ratios $R_{D/RN}$ and effective lateral resolutions r_e have been calculated according to Formulae (36) and (39), respectively.

The calculation of lateral resolution r_e according to Formula (39) is demonstrated for three simulated linescans over the same gratings with different signal-to-noise ratios $R_{S/N}$ (cf. Figure 58). Without interpolation and extrapolation the value of effective lateral resolution corresponds in all three linescans to the period P_1 = 56 nm of the finest resolved grating. The calculated values of r_e are considerably smaller than that value and confirm the usefulness of the calculation method.

4.4.3 Determination of the contrast transfer function CTF

The contrast transfer function CTF characterizes the frequency response of an imaging system to a square-wave grating by the correlation of the image contrast c_i to the object contrast c_o measured as a function of spatial frequency k:

$$\text{CTF}(k) = c_i/c_o \tag{41}$$

k is the reciprocal of the period *P* of the imaged square-wave grating (cf. 4.1.5).

For imaging by scanning instruments CTF, LSF and ESF are determined by the width and shape of the probing beam and by beam-sample interaction, e.g. electron scattering in the sample, as well. This physical meaning is rather obvious for LSF and ESF (cf. 5.2.2) whereas the advantage of the CTF is to straightforwardly reveal the limit of lateral resolution (cf. Figure 62) and to give a more complete description of the imaging process. Therefore the CTF and, in the macroscopic range, the MTF (cf. 4.1.4 and 4.2.6), were used to characterize the performance of imaging instruments.[8,10]

In the high frequency range near the cut-off frequency at $c_\mathrm{i} = 0$ the image contrast and therewith the CTF of 3-stripe gratings is somewhat smaller than those of gratings with 7 or more stripes (cf. 4.4.1.1). However 3-stripe gratings are a favoured layout because they need a minimum of space on the test sample's surface and enable a maximum number of different gratings in the field of view of the imaging instrument. Because this is rather an important advantage for the determination of the CTF, only this type of grating is considered here. All simulations have been done for 3-stripe gratings with three stripes of the same width and a period/gap ratio of $P_\mathrm{gr}/G = 2$ (cf. 4.4.1.2).

4.4.3.1 The effect of the line spread function on image contrast

The line spread function LSF (cf. 4.1.2) and the contrast transfer function CTF reflect the same aspects of imaging performance. The LSF does that as its spatial representation and the CTF is its representation in the spatial frequency domain. There is a unique relation between both functions. However, for square-wave gratings this relation is not as simple as for sine-wave gratings, where one function is the Fourier transform of the other (cf. Figure 7).

Figure 59 shows the effect of width and shape of the LSF on the CTF. Values of image contrast $\mathrm{c_i}$ were determined from the images of 9 gratings of different periods.

Two types of LSF were used for the simulation of imaging. The Gaussian function may be used to describe the intensity distribution within a beam of light or particles. The Lorentzian function has long tails and is particularly suitable for the simulation of imaging of strongly scattering materials. The comparison of imaging with Gaussian and Lorentzian LSFs shows that the quality of images in terms of resolution depends not only on the halfwidth of the LSF but also on its shape. It is not easy to decide whether a Gaussian or a Lorentzian LSF result in a better image quality. At large periods (small frequencies), the Gaussian LSF gives a higher image contrast, but at small periods (high frequencies) the Lorentzian LSF gives a higher image contrast and therefore better lateral resolutions. Hence it follows that the performance of an imaging instrument cannot be described completely by a single parameter like the $\mathrm{w_{LSF}}$.

Nevertheless lateral resolution is the most important parameter and can be determined as the reciprocal of the cut-off frequency in the CTF. The cut-off frequency is the smallest spatial frequency where $c_\mathrm{i} = 0$. Moreover it corresponds to the information limit, which is the highest spatial frequency at which information is transferred from object to image. The term information limit was introduced previously in transmission electron microscopy.[31-34]

4.4.3.2 The generalized CTF

For a given shape of the LSF the image contrast $\mathrm{c_i}$ in a line scan across a square-wave grating is determined unequivocally by the ratio of the $\mathrm{w_{LSF}}$ to the grating period P_gr. This is clearly visible in Figure 59. For instance $c_\mathrm{i} = 0.52$ was found for $P_\mathrm{gr} = 400$ nm imaged with a Gaussian of $w_\mathrm{LSF} = 200$ nm but the same image contrast is obtained with $P_\mathrm{gr} = 100$ nm imaged with a Gaussian of $w_\mathrm{LSF} = 50$ nm. As a consequence it is possible to establish a generalized CTF where the $w_\mathrm{LSF}/P_\mathrm{gr}$ ratio constitutes the abscissa. Figure 60 shows generalized CTFs for three types of LSF (cf. 4.2.1). The cut-off of the generalized CTF gives the dimensionless quantity $w_\mathrm{LSF}/P_\mathrm{gr}$ at which the image contrast drops to zero (cf. Figure 60). It may be converted to a spatial frequency by division by w_LSF.

Table 7 gives the corresponding values of the generalized CTF.

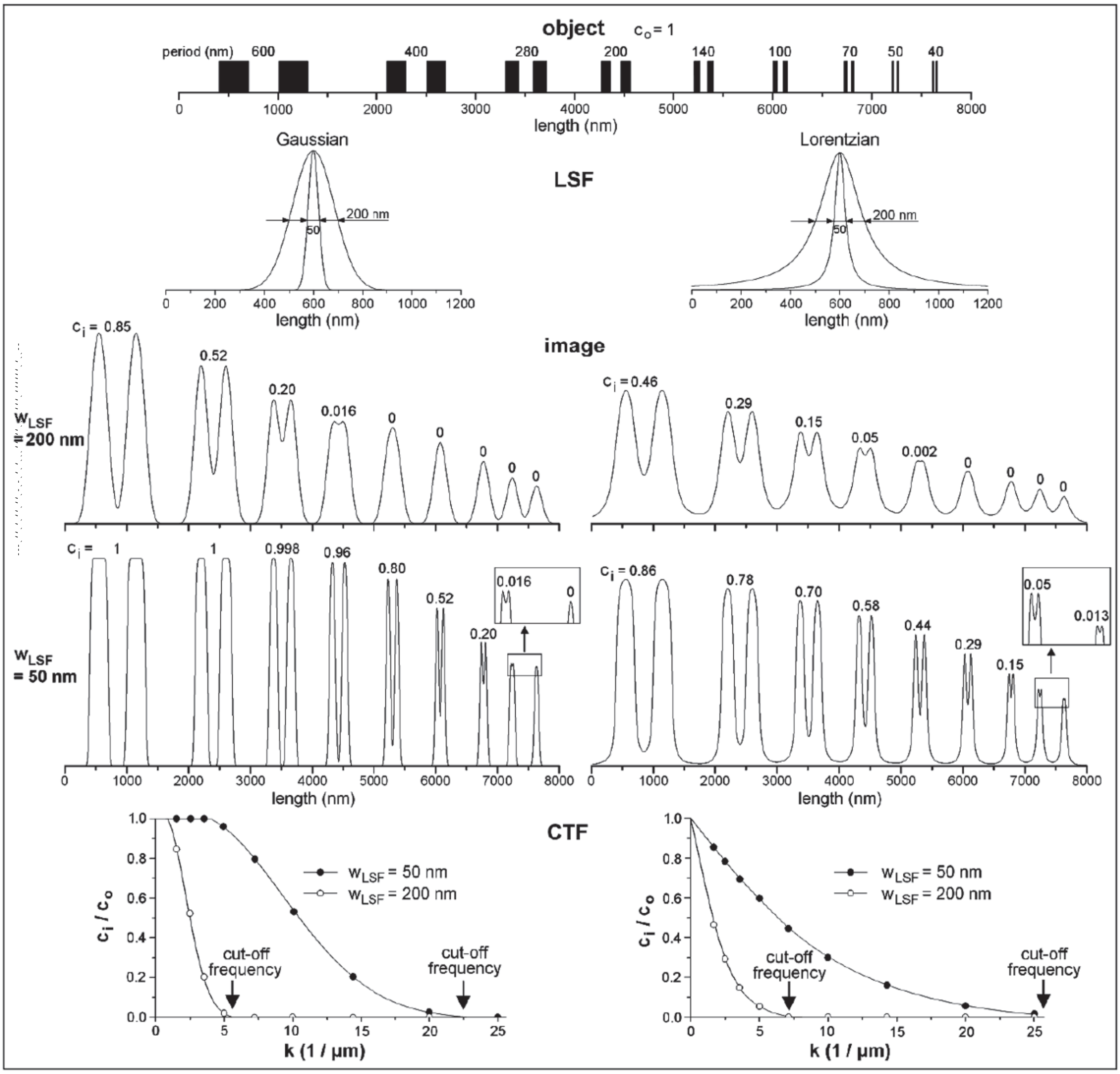

Figure 59 — Simulation of imaging by convolution of a square-wave grating with different line spread functions (LSF) and calculation of the CTFs.[26] **c_o – object contrast; c_i – image contrast; w_{LSF} – full width at half maximum of the LSF**

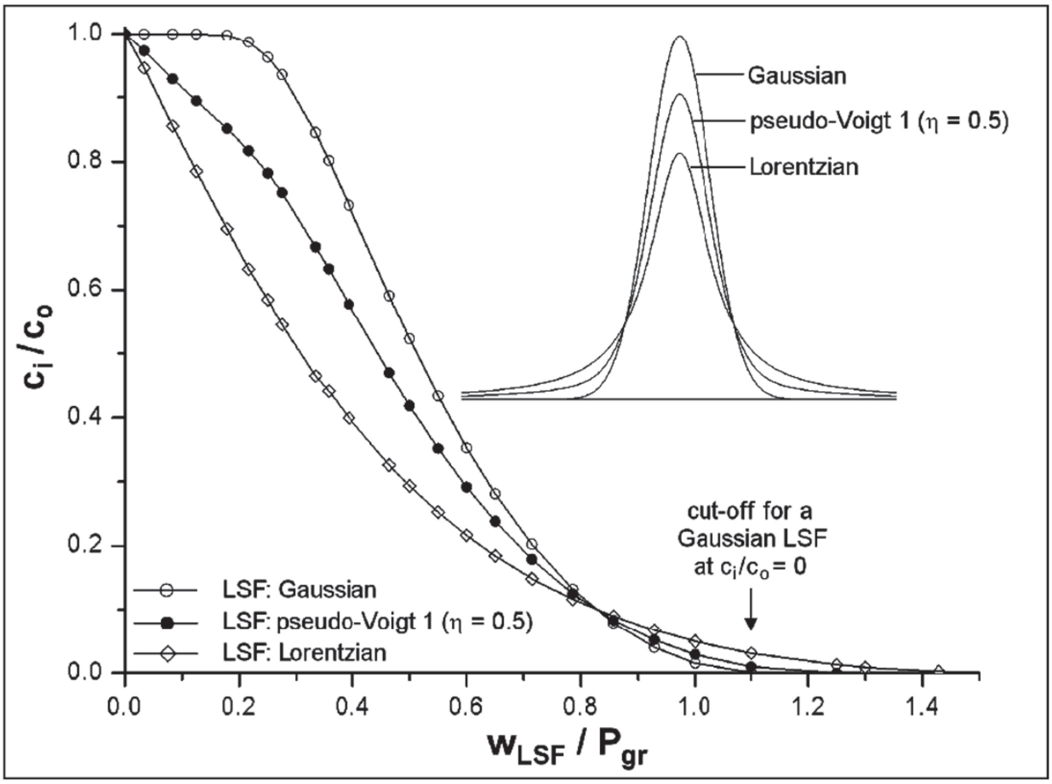

Figure 60 — Generalized CTFs for three types of LSF (cf. 4.2.1)

Table 7 — Values of the generalized CTF for three types of LSF (cf. 4.2.1)

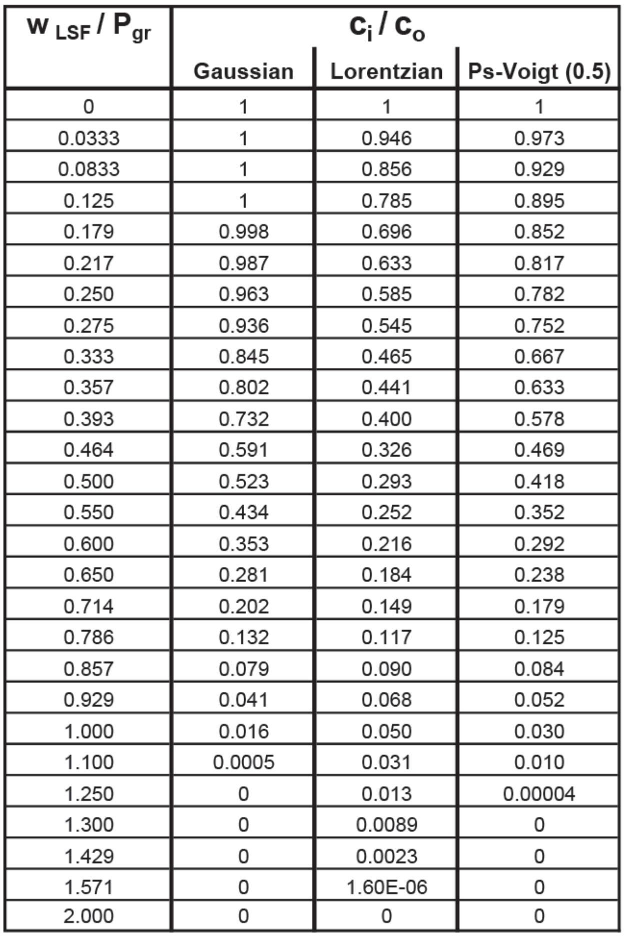

w_{LSF} / P_{gr}	c_i / c_o		
	Gaussian	Lorentzian	Ps-Voigt (0.5)
0	1	1	1
0.0333	1	0.946	0.973
0.0833	1	0.856	0.929
0.125	1	0.785	0.895
0.179	0.998	0.696	0.852
0.217	0.987	0.633	0.817
0.250	0.963	0.585	0.782
0.275	0.936	0.545	0.752
0.333	0.845	0.465	0.667
0.357	0.802	0.441	0.633
0.393	0.732	0.400	0.578
0.464	0.591	0.326	0.469
0.500	0.523	0.293	0.418
0.550	0.434	0.252	0.352
0.600	0.353	0.216	0.292
0.650	0.281	0.184	0.238
0.714	0.202	0.149	0.179
0.786	0.132	0.117	0.125
0.857	0.079	0.090	0.084
0.929	0.041	0.068	0.052
1.000	0.016	0.050	0.030
1.100	0.0005	0.031	0.010
1.250	0	0.013	0.00004
1.300	0	0.0089	0
1.429	0	0.0023	0
1.571	0	1.60E-06	0
2.000	0	0	0

w_{LSF}/P_{gr} is a dimensionless quantity. The division of this quantity by w_{LSF} convert it back to spatial frequency again and enable the calculation of families of CTF curves on different scales of spatial frequency as shown in Figure 61 for a Gaussian LSF. These families of CTF curves may be used to fit experimental data and therewith to characterize type and width of the LSF. The value of w_{LSF} must be selected in such a way that a CTF in the interesting region of spatial frequency will be created. One possibility is to use an estimated w_{LSF}. Another possibility is to use the reciprocal of the period of a square-wave grating of the test sample.

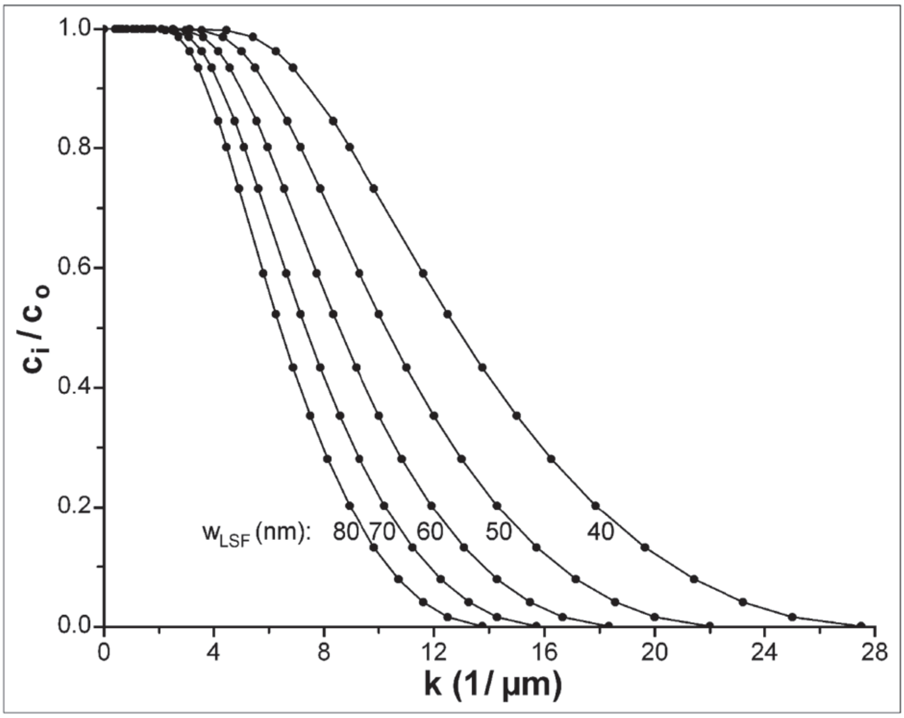

Figure 61 — CTFs for Gaussian LSFs of different w_{LSF}. The c_i / c_o values were taken from Table 7 and the corresponding k values were calculated by division of the w_{LSF}/P values from Table 7 by different values of w_{LSF}

4.4.3.3 CTF and the effective cut-off frequency

Figure 60 shows the cut-off of the generalized CTF. After conversion of the generalized CTF to a CTF for a defined w_{LSF} this cut-off is converted into a cut-off frequency which corresponds to the reciprocal of the threshold of resolution in the absence of noise. In practice, noise is a limiting factor of resolution and, therefore, in the following we introduce an effective cut-off frequency covering the effect of noise. According to Formula (41) the CTF is defined by

$$\mathrm{CTF} = \frac{c_\mathrm{i}}{c_\mathrm{o}} = \frac{1}{c_\mathrm{o}}\left(\frac{I_\mathrm{max} - I_\mathrm{min}}{I_\mathrm{max} + I_\mathrm{min}}\right) \tag{42}$$

With the dip $D = I_\mathrm{max} - I_\mathrm{min}$ and the mean intensity $I_\mathrm{m} = (I_\mathrm{max} + I_\mathrm{min})/2$ it follows from Formula (42)

$$\frac{c_\mathrm{i}}{c_\mathrm{o}} = \frac{D}{2c_\mathrm{o}I_\mathrm{m}} \tag{43}$$

The definition of D/σ_NR in Formula (36) and the resolution criterion (37) lead to the dip at the threshold of resolution D_ThR

$$D_\mathrm{ThR} = \frac{8\sigma_\mathrm{N}}{\sqrt{S_\mathrm{PP}}} \tag{44}$$

When D_ThR is inserted into Formula (43) it follows

$$\left(\frac{c_\mathrm{i}}{c_\mathrm{o}}\right)_\mathrm{ThR} = \frac{4\sigma_\mathrm{N}}{c_\mathrm{o}I_\mathrm{m}\sqrt{S_\mathrm{PP}}} \tag{45}$$

which gives the CTF at the threshold of resolution. With the signal-to-noise ratio $R_\mathrm{S/N} = I_\mathrm{m}/\sigma_\mathrm{N}$, Formula (45) may be written as

$$\left(\frac{c_\mathrm{i}}{c_\mathrm{o}}\right)_\mathrm{ThR} = \frac{4}{c_\mathrm{o}R_\mathrm{S/N}\sqrt{S_\mathrm{PP}}} \tag{46}$$

The number of samples per period may be expressed by the sampling step width S_w and the period P of the imaged grating

$$S_\mathrm{PP} = \frac{P}{S_\mathrm{w}} \tag{47}$$

Then Formula (46) takes the form

$$\left(\frac{c_\mathrm{i}}{c_\mathrm{o}}\right)_\mathrm{ThR} = \frac{4\sqrt{S_\mathrm{w}/P}}{c_\mathrm{o}R_\mathrm{S/N}} \tag{48}$$

Formula (48) can be displayed as a function of spatial frequency $k = 1/P$

$$\left(\frac{c_\mathrm{i}}{c_\mathrm{o}}\right)_\mathrm{ThR}(k) = \frac{4\sqrt{S_\mathrm{w}k}}{c_\mathrm{o}R_\mathrm{S/N}} \tag{49}$$

The intersection of $(c_\mathrm{i}/c_\mathrm{o})_\mathrm{ThR}(k)$ and CTF (k) gives the effective cut-off frequency (cf. Figure 62), which depends on the shape and width of the LSF, signal-to-noise ratio, and the ratio of sampling step width to grating period. This cut-off frequency is called effective because it corresponds to an effective limit of resolution which takes into account the experimental conditions, in particular noise. Spatial frequencies above the effective cut-off frequency were not transferred from object to image and therefore the effective cut-off frequency corresponds to an effective information limit. The effect of noise on the information limit has been discussed with respect to transmission electron microscopy[28,35] and piezoresponse force microscopy.[36]

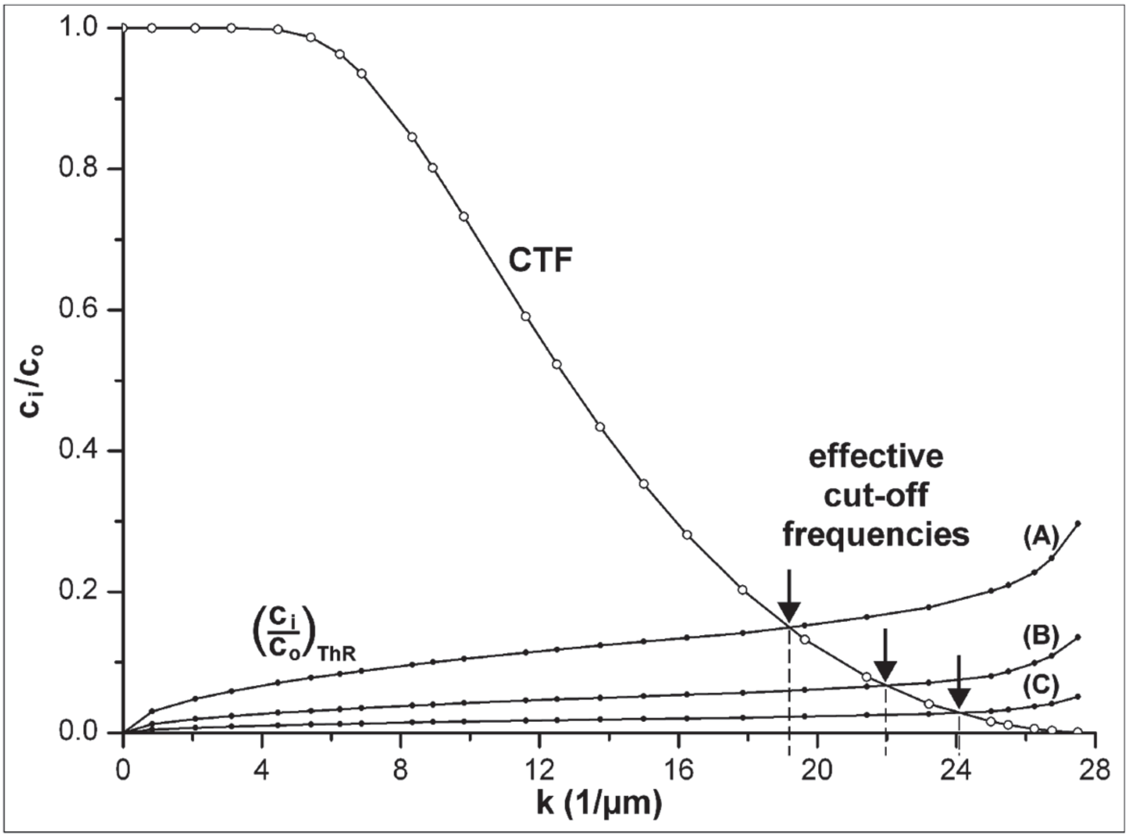

Figure 62 — Determination of effective cut-off frequencies for three sets of experimental conditions according to line scans given in Figure 56 (bottom left and middle left and right). (A): $R_{S/N} = 10$, $S_w = 7$ nm; (B): $R_{S/N} = 25$, $S_w = 7$ nm; (C): $R_{S/N} = 25$, $S_w = 1$ nm. The CTF was calculated for a Gaussian with $w_{LSF} = 40$ nm. Different curves $(c_i/c_o)_{ThR}(k)$ were calculated according to Formula (49). $k = 1/P$ is the spatial frequency. $R_{S/N}$ – signal-to-noise ratio, S_w – sampling step width, P – grating period; c_i and c_o – image and object contrast, respectively

Effective lateral resolution r_e is the reciprocal of the effective cut-off frequency. This definition enables a more accurate determination of lateral resolution than the application of the criterion $D/\sigma_{NR} \geq 4$ to images of distinct gratings (cf. Figure 56), because the determination of the effective cut-off frequency takes into account interpolated values of the CTF between spatial frequencies of different gratings.

In Figure 62 we demonstrate the determination of the effective cut-off frequency for three line scans taken from Figure 56 (bottom left and middle left and right). They differ in signal-to-noise ratio $R_{S/N}$ and sampling step width S_w. At first the generalized CTF (taken from Table 7) is transformed to a CTF for a Gaussian LSF with a $w_{LSF} = 40$ nm. Then the threshold of resolution $(c_i/c_o)_{ThR}(k)$ is calculated according to Formula (49). At high spatial frequencies $(c_i/c_o)_{ThR}$ is progressively increased by multiplication with a correction factor which takes into account the reduction of the period in the image of a 3-stripe-grating near the limit of resolution (cf. Annex A). The effective cut-off frequencies of 19.2 µm^{-1}, 22.0 µm^{-1} and 24.1 µm^{-1} correspond to effective lateral resolutions of 52.1nm, 45.5 and 41.5 nm, respectively. These results are in good agreement with the estimation of lateral resolution based on Figure 56.

An analytical solution for the calculation of the intersection between $(c_i/c_o)_{ThR}(k)$ and CTF (k) does not exist. Therefore we present in 4.4.3.4 a graph and a table for the effective lateral resolution r_e normalized to w_{LSF} and its relation to the normalized effective signal-to-noise ratio $(R_{S/N}/S_w^{1/2})\, w_{LSF}^{1/2}$, where $R_{S/N}$ is the signal-to-noise ratio and S_w is the sampling step width. For the case that noise is pure shot noise caused by counting statistics, for instance SIMS (cf. the application example in 4.4.5), then noise is determined by $R_{S/N} = I/I^{1/2} = I^{1/2}$ and the resolution is determined by $(I/S_w)^{1/2}\, w_{LSF}^{1/2}$.

4.4.3.4 Relation between effective lateral resolution and signal-to-noise ratio

Lateral resolution r_e is the reciprocal of the effective cut-off frequency. The latter is the intercept of $(c_i/c_o)_{ThR}(k)$ and CTF (k) and depends on shape and width of the LSF as well as on signal-to-noise ratio and sampling step width (cf. 4.4.3.3). The intercept of the curves and therewith the effective lateral resolution cannot be calculated analytically. Therefore the relation between the normalized effective lateral resolution $\mathrm{r_e/w_{LSF}}$ and the normalized effective signal-to-noise ratio $(R_{S/N}/S_w^{1/2})\, w_{LSF}^{1/2}$ is presented. w_{LSF} is the full width at half maximum of the LSF, $R_{S/N}$ is the signal-to-noise ratio and S_w is the sampling step width. Figure 63 and Table 8 give this relation for Gaussian and Lorentzian model functions for the LSF.

The intervals between the values have been chosen in such a way that linear interpolation in the intervals provides values of sufficient accuracy. At small values of the normalized effective resolution the curves are asymptotic to the value of resolution in the absence of noise which is determined by the Sparrow criterion $(\mathrm{c_i} > 0)$. The Lorentzian LSF has a much better resolution (smaller values of r_e/w_{LSF}) under good experimental conditions (large values of $(R_{S/N}/S_w^{1/2})w_{LSF}^{1/2}$) than the Gaussian LSF. This difference reflects the fact, that a Lorentzian peak is narrower at the top than a Gaussian peak with the same w_{LSF}.

The normalized values in Table 8 and Figure 63 enable the calculation of the effective lateral resolution r_e from the experimental parameters w_{LSF}, $R_{S/N}$ and S_w and vice versa the determination of experimental parameters which are necessary to obtain a required value of r_e. The latter case will be demonstrated for a Gaussian LSF with $w_{LSF} = 40$ nm. A required resolution $r_e = 48$ nm corresponds to a value $r_e / w_{LSF} = 1.2$. The corresponding value from Table 8 is

$$\left(R_{S/N} / S_w^{1/2}\right) w_{LSF}^{1/2} = 39.7 \qquad (50)$$

Inserting $\mathrm{w_{LSF}} = 40$ nm it follows

$$R_{S/N}/(S_w)^{1/2} = 39.7/40^{1/2} = 6.28\ \mathrm{nm}^{-1/2} \qquad (51)$$

For sampling step widths of $S_w = 7$ nm (Figure 56, left part) and $S_w = 1$ nm (Figure 56, right part) the experimental parameters given in Table 9 fulfil Formula (51). These values are in agreement with the results shown in Figure 56, where a grating with a period of 48 nm is well resolved at $R_{S/N} = 10$ and $S_w = 1$ nm whereas at $S_w = 7$ nm the threshold of resolution requires a signal-to-noise ratio of $10 < R_{S/N} < 25$.

Table 8 — Normalized effective lateral resolution r_e/w_{LSF} and the corresponding values of normalized effective signal-to-noise ratio $(R_{S/N}/S_w^{1/2})w_{LSF}^{1/2}$ for Gaussian and Lorentzian LSFs. $(I/S_w)^{1/2}\ w_{LSF}^{1/2}$ is the parameter for pure shot noise

r_e / w_{LSF}	$(R_{S/N} / S_w^{1/2})\ w_{LSF}^{1/2}$ for pure shot noise: $(I\ /\ S_w)^{1/2}\ w_{LSF}^{1/2}$	
	Gaussian LSF	**Lorentzian LSF**
0.68		5848
0.70		2801
0.72		1684
0.74		1109
0.76		741
0.78		538
0.80		408
0.82		326
0.84		262
0.86		217
0.88		184
0.90		159
0.92	5000	138
0.94	1563	120
0.96	714	107
0.98	435	95.2
1.00	294	85.8
1.02	206	78.7
1.04	156	71.4
1.06	123	65.0
1.08	99	59.7
1.10	82.3	55.0
1.12	68.3	51.1
1.16	51.3	44.3
1.20	39.7	39.1
1.24	31.9	34.7
1.28	26.5	31.2
1.32	22.2	28.0
1.36	19.0	25.5
1.40	16.6	23.3
1.50	12.5	19.2
1.60	10.0	16.2
1.70	8.25	13.9
1.80	7.03	12.2

Table 9 — Experimental parameters for an effective lateral resolution of 48 nm calculated from Table 8

w_{LSF} (nm)	S_w (nm)	$R_{S/N}$
40	1	6.3
40	7	16.6

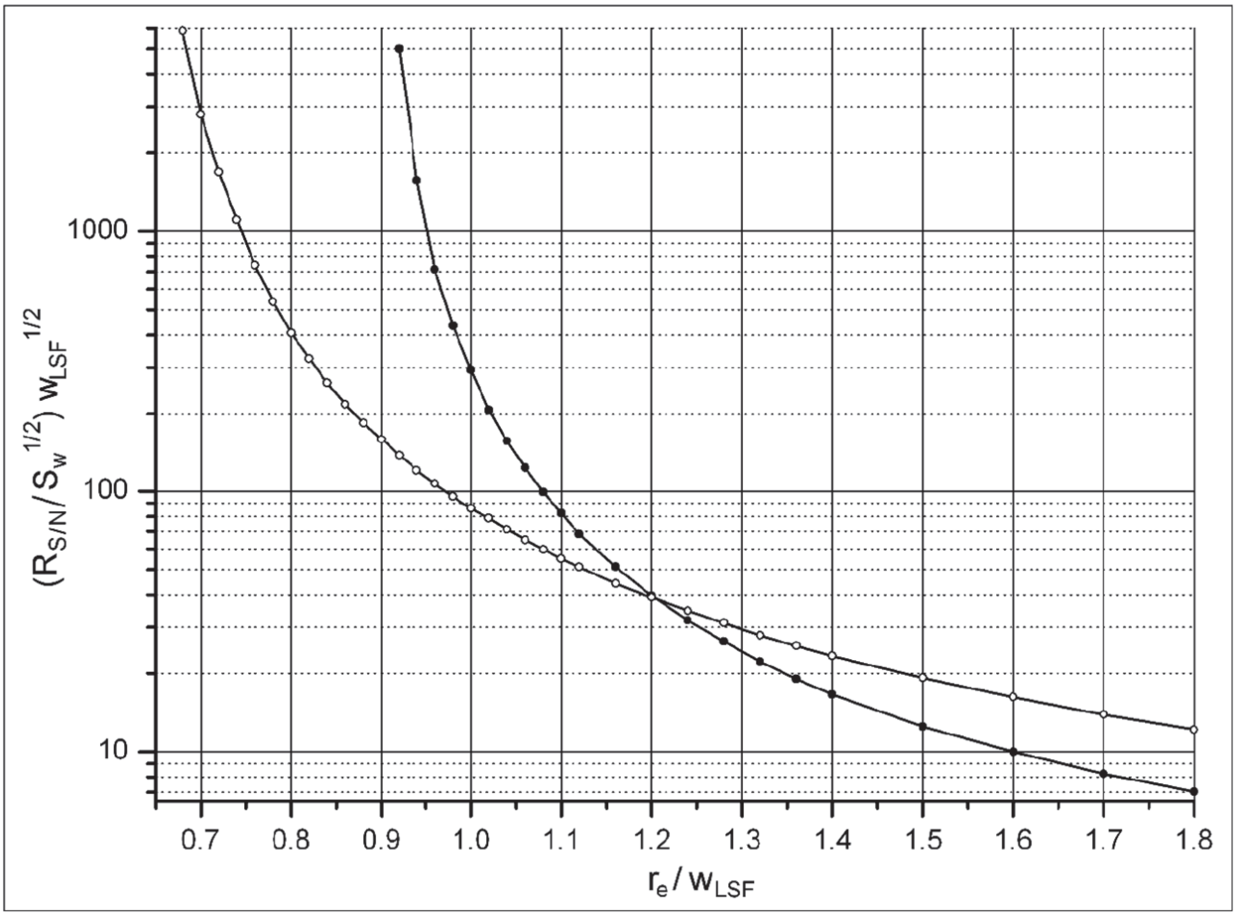

Figure 63 — Relation between normalized effective lateral resolution r_e/w_{LSF} and normalized effective signal-to-noise ratio $(R_{S/N}/S_w^{1/2})w_{LSF}^{1/2}$ for two types of LSF.[26] **Open symbols – Lorentzian LSF; closed symbols – Gaussian LSF**

In the case of pure shot noise the required signal intensity for a given resolution can be calculated from Table 8 also. For the same parameters used above it follows

$$(I/S_w)^{1/2} = 39.7/40^{1/2} = 6.28\ \text{nm}^{-1/2} \qquad (52)$$

The intensities given in Table 10 yields a resolution of 48 nm for the step widths S_w used.

Table 10 — Required intensities for an effective lateral resolution of 48 nm in the case of pure shot noise calculated from Table 8

w_{LSF} (nm)	S_w (nm)	I (counts)
40	1	39
40	7	276

4.4.3.5 The effect of scanning step width on image contrast

Most imaging methods in surface chemical analysis are based on scanning procedures. For these methods the quality of resulting images is substantially determined by the scanning step width used. Scanning step width issues in relation to signal-to-noise ratio were considered with respect to their relevance to image contrast and lateral resolution in 4.4.2.3 and 4.4.3.3. In the following the effect of scanning step width on image contrast is analysed neglecting noise. For imaging of gratings it is useful to express the scanning step width as the number of sampling points per period S_{PP}. Figure 64 demonstrates the effect of the scanning step width for the imaging of a square wave grating. Imaging was simulated by convolution of a 7-strip grating with a Gaussian LSF. The quality of imaging is characterized in terms of the related image contrast c_{i} (for definition, cf. Figure 46). This analysis reveals the following:

1. By increasing the number of sampling points per period S_{PP} the image quality is improved and the image contrast c_{i} can be determined more correctly.

2. For small numbers of sampling points per period, e.g. 4 as displayed in Figure 64, the image contrast strongly depends on the phase relation between sampling and image profile. A phase shift of a half scanning step width may vary the value of the image contrast from a maximum (c_{i} = 0.523) down to a minimum (c_{i} = 0.370), which is in that case an underestimation of 30 %.

3. If the ratio of the grating period to the scanning step width is an *integer* (e.g. 4 spp and 20 spp, respectively, in Figure 64), then sampling is in a fixed phase relationship with the image profile. In that case the measured image contrast yields the same value for all imaged periods of the grating. If this ratio is *not an integer* (e.g. 5.88 spp and 7.69 spp, respectively, in Figure 64), the measured image contrast varies from period to period. This variation decreases with increasing S_{PP}.

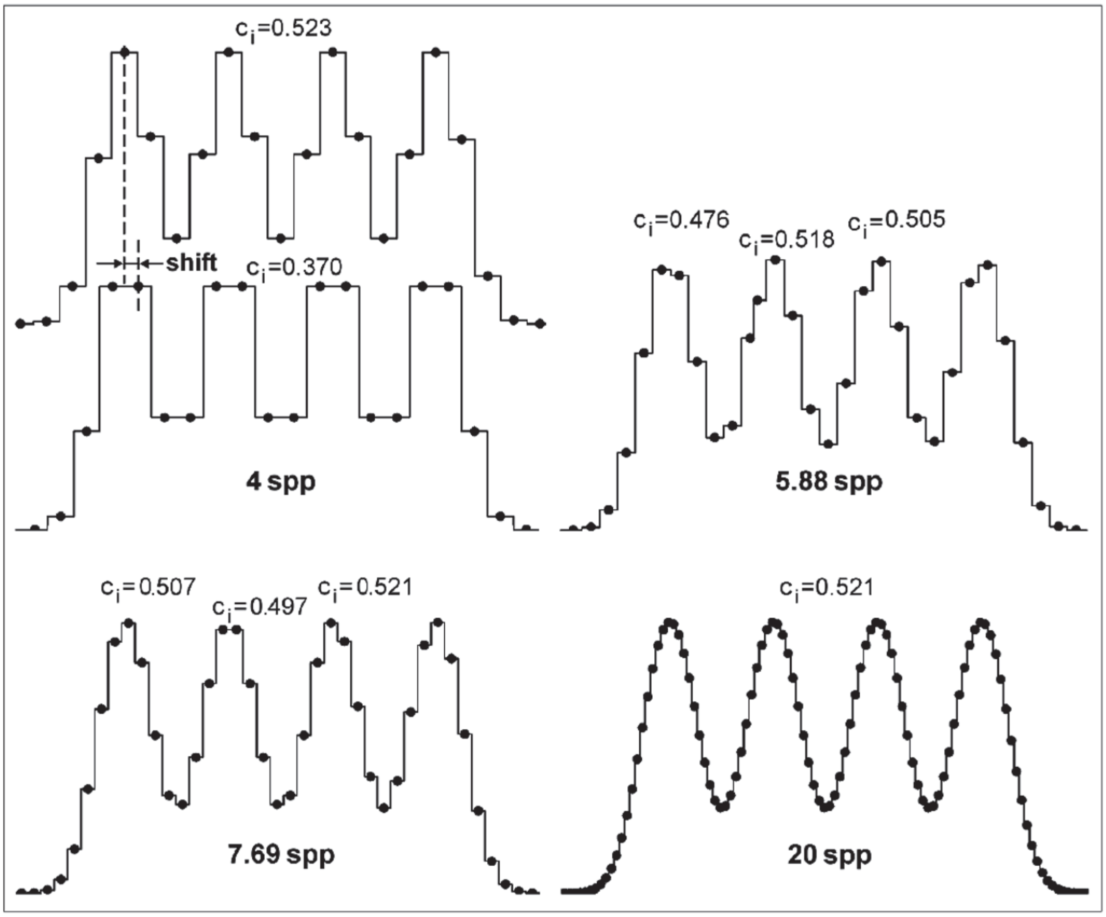

Figure 64 — Effect of scanning step width, expressed as S_{PP} (sample per period), on image contrast c_{i}. Imaging of a square-wave grating with a period of 100 nm was simulated by convolution with a Gaussian LSF (w_{LSF} = 50 nm). The black circles are the calculated image points. The phase shift between the values in the two images with 4 spp is 1/2 scanning step width (1/8 period)

The effects described by 1. to 3. can be minimized by choosing S_{PP} as large as possible in an experiment. However, for a determination of the CTF it is necessary to simultaneously image a complete set of gratings which may give only a small value of S_{PP} for the grating with the smallest period. To quantify the effect of SPP on c_i the imaging of a 3-stripe grating by convolution with a Gaussian LSF was simulated in Figure 65. For given SPP the worst case with respect to the resulting c_i is given at the top, the best case on the bottom. All possible values of c_i are found in between those extreme values. For even numbers of SPP the deviation of a measured c_i from its value measured at a large value of SPP may be zero. In this case sampling points hit the maxima as well as the minimum (Figure 65 for 4 spp and 6 spp). For odd and fractional numbers for SPP, there is always an underestimation of c_i. Figure 66 enables the determination of the minimum number of sampling points per period for a required accuracy of image contrast. For instance, maximum deviations of 10 % and 5 % require at least 6.5 spp and 9 spp, respectively.

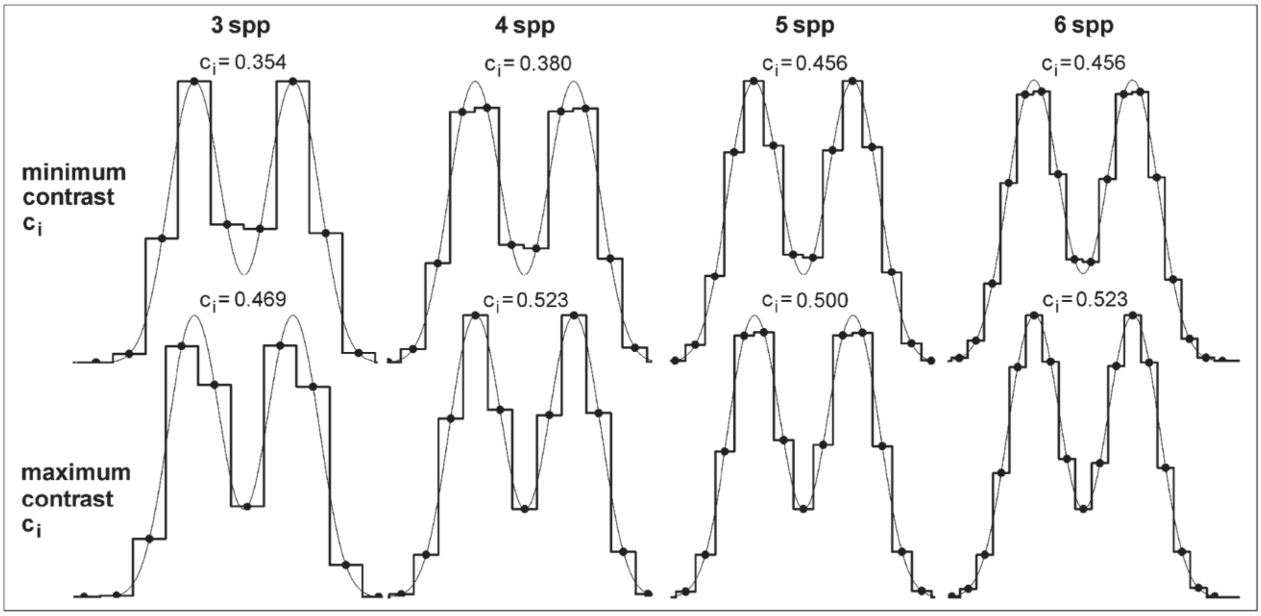

Figure 65 — The effect of phase shift between grating and sampling points on image contrast c_i for different scanning step widths (*S*PP: samples per period). The upper row shows the worst case (minimum contrast) and the lower row shows the best case (maximum contrast) imaging. Imaging of the grating with a period of 120 nm was simulated by convolution with a Gaussian LSF (w_{LSF} = 60 nm). The calculated image points (black circles) are connected by step functions (thick lines). The thin lines are image profiles with 120 spp

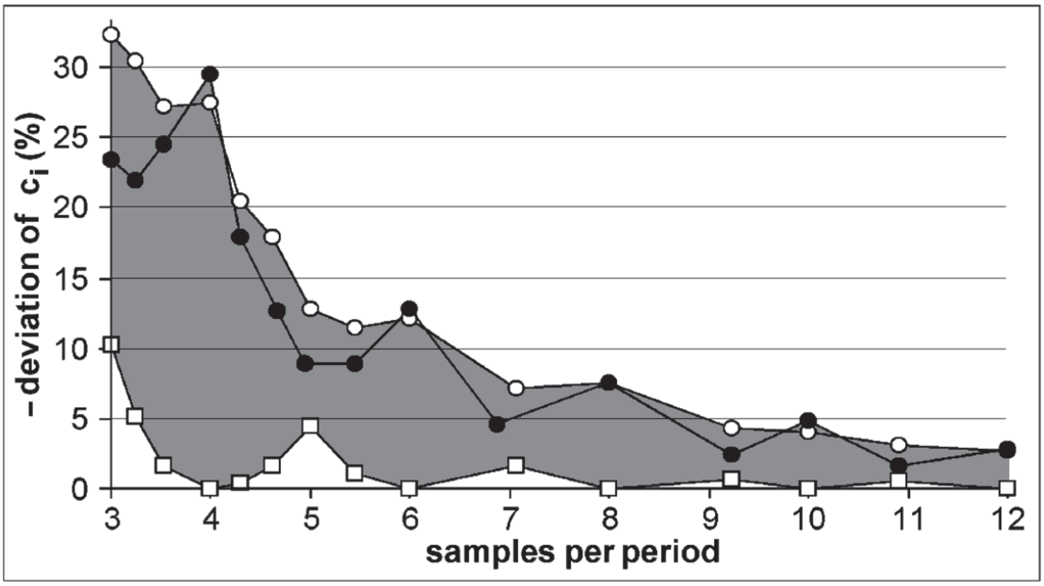

Figure 66 — Maximum (circle) and minimum (square) deviation of image contrast c_i from the value measured at large values of S_{PP}. White symbols were calculated for the case given in Figure 65 ($c_{i\ max}$ = 0.523). The black circles were calculated for a low resolution case with a grating period of 120 nm and a 100 nm FWHM Gaussian LSF giving a maximum image contrast of $c_{i\ max}$ = 0.095

4.4.4 Requirements for test samples and accuracy of measurement

The accuracy of the effective lateral resolution r_e

The value of effective lateral resolution r_e as well as its accuracy, expressed as the expanded uncertainty U(r_e), depend on measurement conditions like noise and sampling step width. The accuracy for the determination of effective lateral resolution will be discussed for two methods: 1) Visual inspection of an image of a series of gratings and 2) determination by interpolation/extrapolation from a line scan over at least three imaged gratings (cf. 4.4.2.4). The determination of effective lateral resolution from the effective cut-off frequency (cf. 4.4.3.3) will not be discussed here, because this method is time-consuming and its accuracy is comparable to that of the less time-consuming interpolation/extrapolation method.

Determination of effective lateral resolution by visual inspection of the image

The simplest method for the determination of effective lateral resolution is the visual identification of the finest resolved grating from of a series of gratings (cf. 4.4.2.). Effective lateral resolution can be determined directly during measurement and corresponds to the period of the finest resolved grating, see Formula (38).

This method is easy and quick to perform and therefore it is a favoured approach in practical surface analysis. Nevertheless this method has two drawbacks:

1. The decision whether a grating is resolved or not is subjective.
2. The accuracy of effective lateral resolution is limited by the difference between the period of the finest resolved grating P_1 and the period of the first non-resolved grating P_0.

The value $r_e = P_1$ is an upper estimate of effective lateral resolution. The true effective lateral resolution may be better (i.e. the true value of r_e may be smaller than P_1), but this deviation Δr_e cannot be quantified with this method. From a statistical point of view the deviation Δr_e is an uncertainty of r_e, but the asymmetric interval Δr_e extends only to smaller values of r_e (better resolutions) and therefore it is not an uncertainty of r_e in its usual meaning.

The maximum deviation of effective lateral resolution[10] $\Delta r_e{}^{max}$ can be used to characterize the accuracy of the determination of effective lateral resolution by visual inspection:

$$\Delta r_e{}^{max} = -(P_1 - P_0) \tag{53}$$

A more general measure of accuracy is the relative maximum deviation

$$\Delta r_e{}^{max} / r_e = -(P_1 - P_0)/P_1 = (1/q) - 1 \tag{54}$$

which depends only on the grading factor $q = P_1/P_0$[11] of the test sample (cf. Figure 67).

Correspondingly the accuracy of effective lateral resolution can be improved by decreasing the grading factor q of grating periods of the test sample. This approach has three limitations:

1. A decrease of the grading factor reduces the range of grating periods within the field of view of the instrument and therewith the covered range of effective lateral resolution.
2. Finely graded grating periods must have a high accuracy.
3. At high levels of noise and finely graded grating periods (small values of q) it may be difficult to decide whether a grating is resolved or not.

The optimum range of the grading factor for visual inspection of effective lateral resolution is

$$1.2 \le q \le 1.5 \tag{55}$$

The estimation of effective lateral resolution r_e and its maximum deviation $\Delta r_e{}^{max}$ is demonstrated for two examples given in Figures 72a and 72b, respectively:

from Figure 71a: $r_e = 193$ nm, $\Delta_r{}^{emax} = -57$ nm

from Figure 71b: $r_e = 136$ nm, $\Delta r_e{}^{max} = -39$ nm

The relative maximum deviations $\Delta r_e{}^{max}/r_e$ of −29.5 % [from Figure 72 a)] and −28.7 % (from Figure 72b), respectively, are within the 23 % to 33 % interval (grey shaded area in Figure 67) which is determined by the range of grading factors q of the used certified reference material BAM-L200.

The uncertainty, in its usual meaning, of lateral resolution established by visual inspection of the grating images is determined by the uncertainty of the period of the finest resolved grating

$$U(r_e) = U(P_1) \tag{56}$$

and depends on the quality of the test sample and its certification. The uncertainty of a grating period should be smaller than the distance between consecutive gratings

$$U(P_1) < (P_1 - P_0) \tag{57}$$

---

10) The deviation due to the uncertainty of certified grating periods of the test sample (see below) is not included.

11) The general definition of the grading factor is $q = P_{n+1}/P_n$, where $P_{n+1} > P_n$ are periods of consecutive gratings in a series. The grading factor may vary within a series of gratings and then r_e and Δr_e must be calculated with P_1 and P_0.

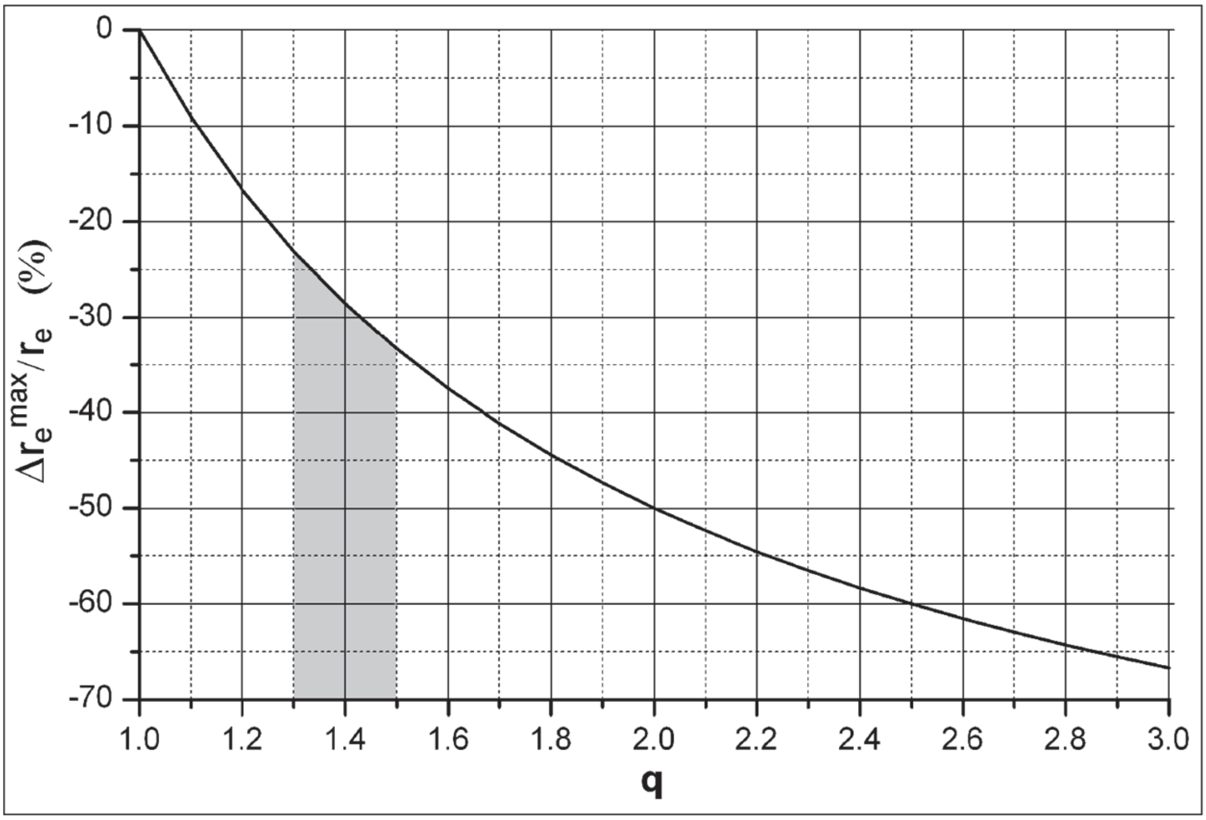

Figure 67 — The relative maximum deviation $\Delta r_e^{\max}/r_e$ of effective lateral resolution r_e as a function of grading factor q calculated from Formula (54). The uncertainty of grating periods is not included. The grey area marks the region of q-values of the certified reference material BAM-L200 which was used for the experimental examples given below

Determination of effective lateral resolution by a combination of interpolation and extrapolation

This method (cf. 4.4.2.4) is based on the analysis of a linescan over a series of gratings and enables a more accurate determination of effective lateral resolution r_e than the visual inspection of imaged gratings. The interpolation-extrapolation procedure (cf. Figure 57) is based on three points of the curve $R_{D/RN}$ (P), where $R_{D/RN}$ is the dip-to-reduced-noise ratio obtained from a linescan and P is the corresponding grating period.

Four sources of uncertainty must be considered with respect to the uncertainty of r_e:

1. The uncertainties of the dips D, depending on the signal-to-noise ratio $R_{S/N}$ of the line scan and the number of samples per grating period.
2. The uncertainty of noise σ_N, depending on the number of points from which σ_N has been determined (cf. Figure 54).
3. The uncertainty of grating periods P of the test sample.
4. The uncertainty of the interpolation-extrapolation procedure itself, depending on the grading factor q and the relation between grating periods and the width of the line spread function w_{LSF}.

Propagation of uncertainties into the final uncertainty of r_e has been studied by Monte Carlo simulation. The simultaneous variation of the variables $R_{D/RN}$ (R_0, R_1 and R_2 in Formula (39)) and P (P_0, P_1, and P_2 in Formula (39)) yields a more realistic value of the uncertainty of r_e than the separated analysis of the influence of variables with the subsequent combination of uncertainties. The values of $R_{D/RN}$ and P have been varied randomly (Gaussian distribution) and r_e has been calculated according to Formula (39) for different sets of gratings, different signal-to-noise ratios $R_{S/N}$ and different uncertainties of the grating periods P. For the variation of the variables $R_{D/RN}$ and P realistic standard deviations have been used.

The standard deviations $\sigma(D)$ for different gratings and 3 values of $R_{S/N}$ have been determined from simulated linescans with different sets of added noise. The relative standard deviation $\sigma(D)/\bar{D}$ varies between 0.5 % (at $R_{S/N}$ = 100, large value of D) and 160 % (at $R_{S/N}$ = 10, small value of D).

The relative standard deviation of noise $\sigma(\sigma_N)/\bar{\sigma}_N$ has been chosen as 10 % for all linescans. This value corresponds to the determination of σ_N from 40 measured values (cf. Figure 54).

The relative standard deviation of grating periods $\sigma(P)/\bar{P}$ has been taken from the certificate of the test sample BAM-L200.[6] 2.5 % corresponds to the relative standard deviation of P in the 100 nm region and 5 % corresponds to the relative standard deviation of P in the 10 nm region, respectively.

The Monte Carlo simulation yields the standard deviation of effective lateral resolution $\sigma(r_e)$ and the systematic deviation $\Delta r_e = r_e - r_e^{true}$, where r_e^{true} has been taken by interpolation from Table 8. The systematic deviation Δr_e originates from the determination of r_e by the interpolation-extrapolation method (cf. Table 6).

According to the GUM approach[22] the quadratic addition of different components, here the random deviation and the systematic deviation, gives the combined expanded uncertainty.

$$U_c(r_e) = \{[2\sigma(r_e)]^2 + (\Delta r_e)^2\}^{½} \qquad (58)$$

The coverage factor k = 2, which corresponds to a coverage probability of approximately 95 % for a normal distribution, has to be applied only to the random components of uncertainty and therefore Δr_e is not expanded. Table 11 shows 9 examples for the calculation of $U_c(r_e)$ from the results of the Monte Carlo simulation.

The calculated values of $U_c(r_e)$ for an example with a Gaussian line spread function with w_{LSF} = 40 nm (cf. Figures 56–58) are shown in Figure 68. The selected signal-to-noise ratios of 100, 25 and 10 correspond to very good, mean and poor experimental conditions as shown in Figure 58. For every value of the grading factor q different series of gratings were used for the calculation of the uncertainty $U_c(r_e)$. In accordance with the interpolation-extrapolation method described in 4.4.2.4 the grating periods must be chosen in such a way, that at the given signal-to-noise ratio $R_{S/N}$ the smallest grating with the period P_0 is not resolved and the gratings with the periods P_1 and P_2 are resolved, respectively.

Table 11 — Examples for the calculation of $U_c(r_e)$ according to Formula (58)

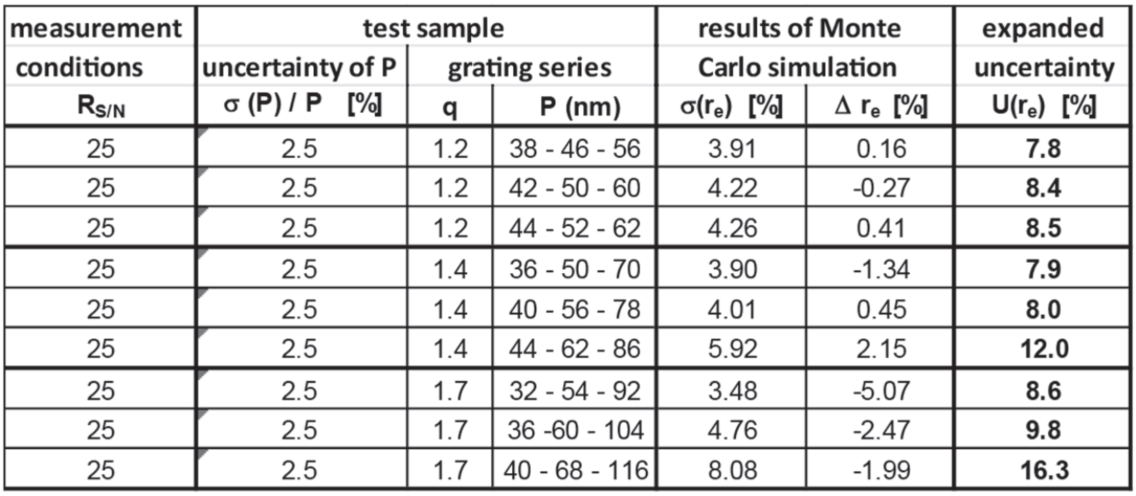

measurement conditions	test sample			results of Monte Carlo simulation		expanded uncertainty
	uncertainty of P	grating series				
$R_{S/N}$	σ (P) / P [%]	q	P (nm)	σ(r_e) [%]	Δ r_e [%]	U(r_e) [%]
25	2.5	1.2	38 - 46 - 56	3.91	0.16	**7.8**
25	2.5	1.2	42 - 50 - 60	4.22	-0.27	**8.4**
25	2.5	1.2	44 - 52 - 62	4.26	0.41	**8.5**
25	2.5	1.4	36 - 50 - 70	3.90	-1.34	**7.9**
25	2.5	1.4	40 - 56 - 78	4.01	0.45	**8.0**
25	2.5	1.4	44 - 62 - 86	5.92	2.15	**12.0**
25	2.5	1.7	32 - 54 - 92	3.48	-5.07	**8.6**
25	2.5	1.7	36 -60 - 104	4.76	-2.47	**9.8**
25	2.5	1.7	40 - 68 - 116	8.08	-1.99	**16.3**

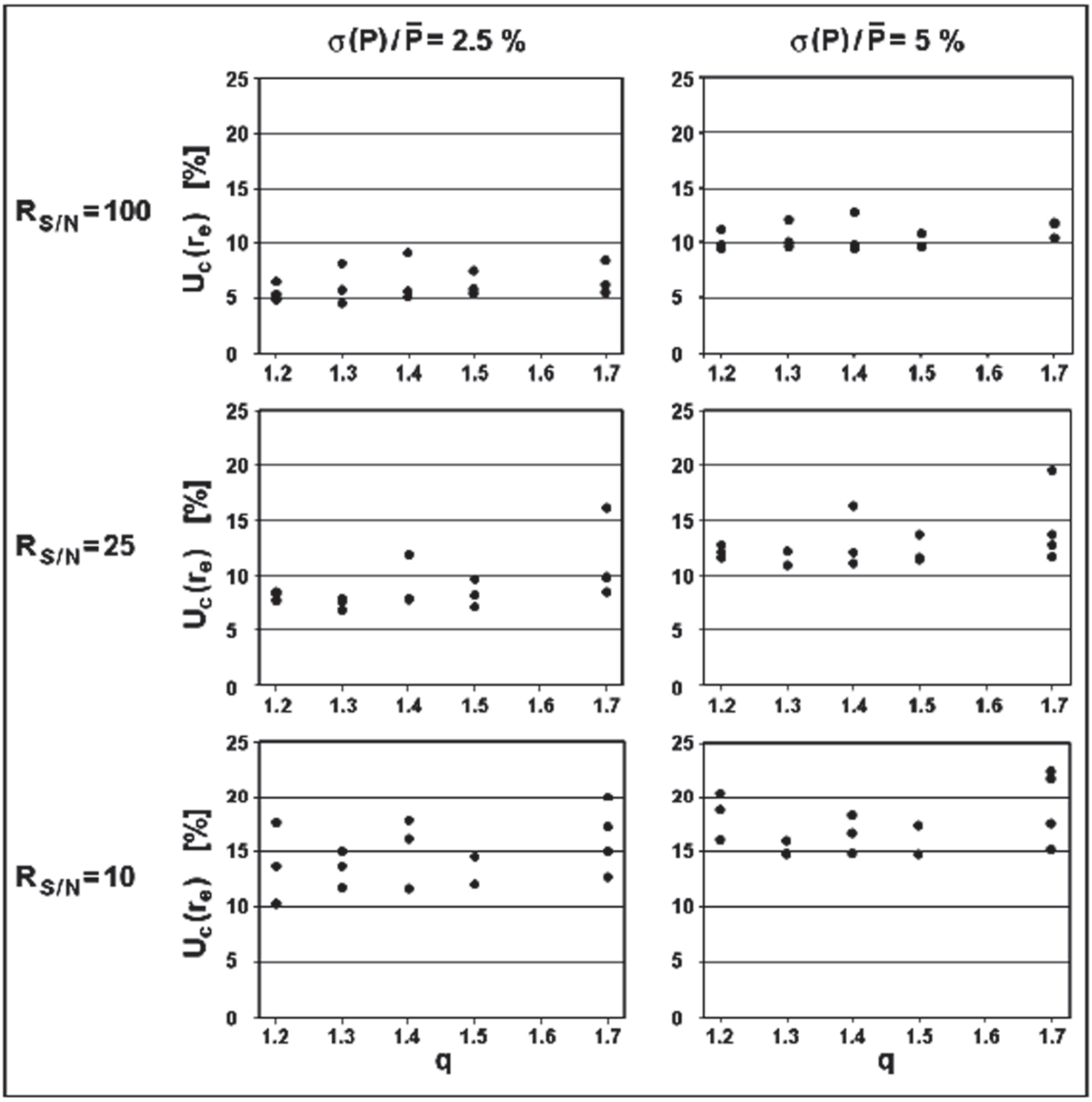

Figure 68 — The relative combined expanded (k = 2) uncertainty $U_c(r_e)$ of effective lateral resolution determined by Monte Carlo simulation and subsequent calculation according to Formula (58) for different measurement conditions and different test samples. The imaging of different series of gratings have been simulated by convolution with a Gaussian LSF with w_{LSF} = 40 nm. $R_{S/N}$ means the signal-to-noise ratio, $\sigma(P)/\bar{P}$ means the relative standard deviation of grating periods

At a low signal-to-noise ratio ($R_{S/N}$ = 10) the Monte Carlo simulation has been shown that outliers of $R_{D/RN}$ must be removed to obtain reasonable values of r_e, $\sigma(r_e)$ and Δr_e.

Figure 68 shows that the grading factor q has only a small effect on the expanded uncertainty of effective lateral resolution. This is due to the fact that $U_c(r_e)$ is mainly determined by the random variation $\sigma(r_e)$ which is, in contrast to the systematic deviation Δr_e, only slightly increasing with q (cf. Table 11). For q < 1.7 the expanded uncertainty of effective lateral resolution $U_c(r_e)$ is below 10 % at very good experimental conditions and below 25 % at poor experimental conditions.

Requirements for test samples

The definition of lateral resolution refers to the “minimum spacing at which two features of the image can be recognised as distinct and separate”[3]. This minimum spacing of separated features depends on the performance of the instrument as well as on properties of the features of the test sample. For that reason a series of gratings with different known periods is needed on an appropriate test sample. 3-stripe gratings need a minimum of required space on the test sample and, therefore, they may provide a maximum number of different gratings in the field of view of the instrument used for imaging. Simulations (cf. 4.4.1.1 and 4.4.1.2) and experiments with a semiconductor stripe pattern (cf. 4.4.5) document the suitability of chemical square-wave gratings A-B-A, where the stripes A and B are of the same width.

Grading factor

The most important parameter of a series of 3-stripe gratings with respect to the accuracy of effective lateral resolution r_e is the grading factor $q = P_{n+1}/P_n$, where P_{n+1} and P_n are the periods of consecutive gratings. The suitable range for the interpolation/extrapolation method (cf. Table 6 and Figure 68) is

$$1.2 \leq q \leq 1.7 \tag{59}$$

Distance between consecutive gratings of the test sample

On the one hand the distance between consecutive gratings of the test sample must be large enough to avoid the distortion of lateral resolution by superposition of grating profiles. Figure 69 shows two effects of grating distance on the profile of the grating image.

1. The separation of individual gratings may be difficult if the distance between the gratings is too small.
2. Different distances to the right adjacent grating and the left adjacent grating may cause an asymmetric shape of a grating profile if these distances are not large enough. This effect of superposition is to a large extent compensated by different signal intensities superimposed on both sides of a grating in a series of graded gratings.

Figure 70 shows this compensation for an example with a Lorentzian LSF, a grading factor $q = 2^{1/2}$ and a minimum grating distance of $d_{gr} = 1.5\,P$. In this case a slight asymmetry of grating profiles is visible only at the outside gratings with only one neighbour.

On the other hand large distances between consecutive gratings reduce the number of gratings in the field of view. As a result the range of grating periods and/or the accuracy of lateral resolution (by a larger grading factor) is reduced.

From these two limitations follows a general optimum value of grating distances

$$1.5\,P \leq d_{gr} \leq 3\,P \tag{60}$$

For imaging with a Gaussian LSF a grating distance $d_{gr} = P$ is sufficiently large.

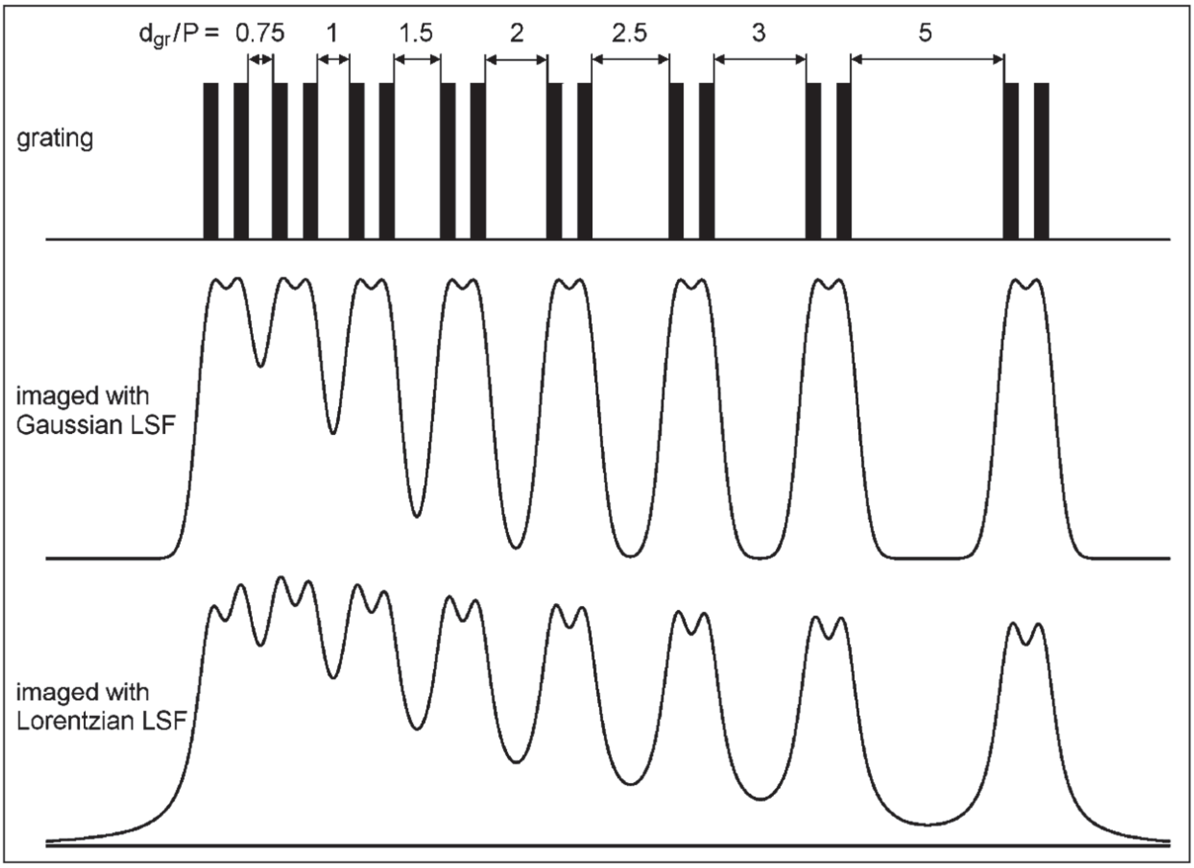

Figure 69 — The effect of grating distance d_{gr} on lateral resolution. Imaging of gratings with a period of $P = 200$ nm was simulated by convolution of these gratings with a Gaussian LSF and a Lorentzian LSF with $w_{\mathrm{LSF}} = 200$ nm both

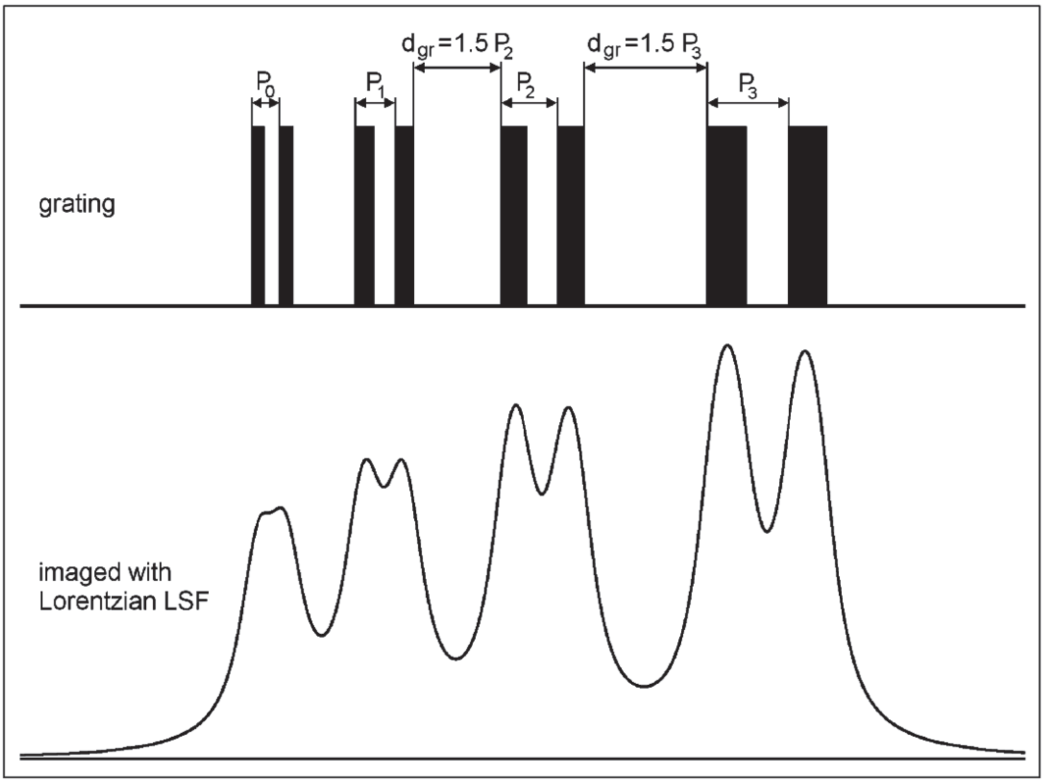

Figure 70 — The effect of neighboured gratings on the image profile in a series of gratings with a grading factor $q = 2^{1/2} = 1.41$. Imaging of gratings with periods P of 142 nm, 200 nm, 284 nm and 400 was simulated by convolution of these gratings with a Lorentzian LSF with $w_{LSF} = 200$ nm

4.4.5 Application example: Element mapping by SIMS

The certified reference material BAM-L200[6] enables the determination of lateral resolution by imaging square-wave gratings with different periods. It has been applied to different nanoscale imaging methods such as Auger electron spectroscopy, energy-filtered core-level photoelectron emission microscopy,[37] X-ray microscopy,[38] and Kelvin probe force microscopy.[39] Here we demonstrate the determination of lateral resolution of imaging SIMS.

BAM-L200 is a cross-section of an $Al_xGa_{1-x}As$ - $In_xGa_{1-x}As$ – GaAs multilayer stack grown by Metal Organic Vapour Phase Epitaxy (MOVPE). The layers form a complex stripe pattern at the surface of a carefully polished cross section.[6]

The stripe pattern was imaged with a ION-TOF IV instrument (ION-TOF GmbH, Münster, Germany) with 25 keV Ga^+ ions. In order to obtain high lateral resolution the extreme crossover mode at a small beam current of 1.36 pA was used. In combination with only a total acquisition time of 47 s the measurement conditions result in a somewhat noisy image, as shown in Figure 71.

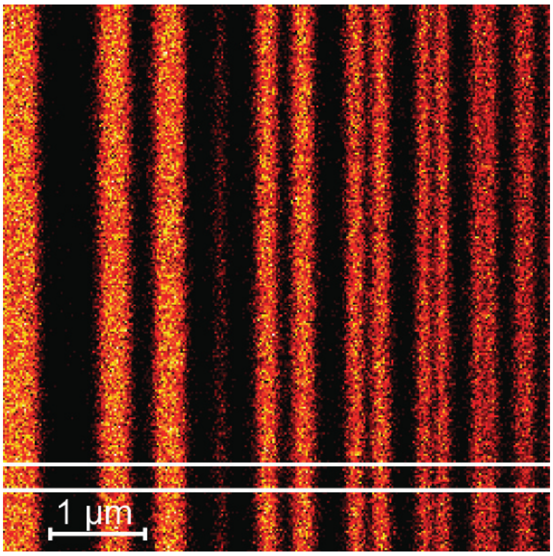

Figure 71 — Al^+ mapping of a section of the BAM-L200 surface including 6 square-wave gratings with periods ranging from 587 nm (left) to 97 nm (right). 256 × 256 pixels were measured with 1 scan, 5 pulses per pixel and a scanning step width of 22.7 nm. The white lines indicate an area comprising 10 scanned lines which were summed to create the linescan shown in Figure 72 a)

Visual inspection of Figure 71 shows that 5 gratings are resolved. The criterion for resolution is the appearance of a dark stripe between two bright stripes. The period of the finest resolved grating (second from right) is 136 nm.

Data from Figure 71 are condensed into two different linescans displayed in Figure 72. They are created by summing acquired counts over 10 lines [(Figure 72 a)] and all 256 lines [Figure 72 b)] with signal-to-noise ratios of 5.4 and 28, respectively. These linescans enable an objective determination of the effective lateral resolution. According to the resolution criterion $D/\sigma_{NR} \geq 4$ [Formula (37)], four gratings are resolved in the line scan in Figure 71a and five gratings are resolved in that of Figure 71 b). The lateral resolution can be estimated to be between 136 nm and 193 nm [Figure 71 a)] and between 97 nm and 136 nm [Figure 71 b)].

The effective lateral resolution can be calculated from a linescan across three gratings by a combination of interpolation and extrapolation (cf. 4.4.2.4). For that reason the dips *D* have been determined according to the procedure displayed in Figure 51 b). The noise of SIMS signals is pure shot noise and can be described by the Poisson distribution. Therefore the noise σ_N at the level of the mean intensity $I_m = (I_{max}+I_{min})/2$ of the grating images has been calculated by $\sigma_N(I_m) = I_m^{1/2}$.

Application of Formula (39) yields effective lateral resolutions $r_e = 173$ nm for the linescan shown in Figure 71 a) and $r_e = 122$ nm for the linescan shown in Figure 71 b), respectively. This considerable difference for linescans measured with the same primary ion beam profile verifies the strong effect of noise on the effective lateral resolution.

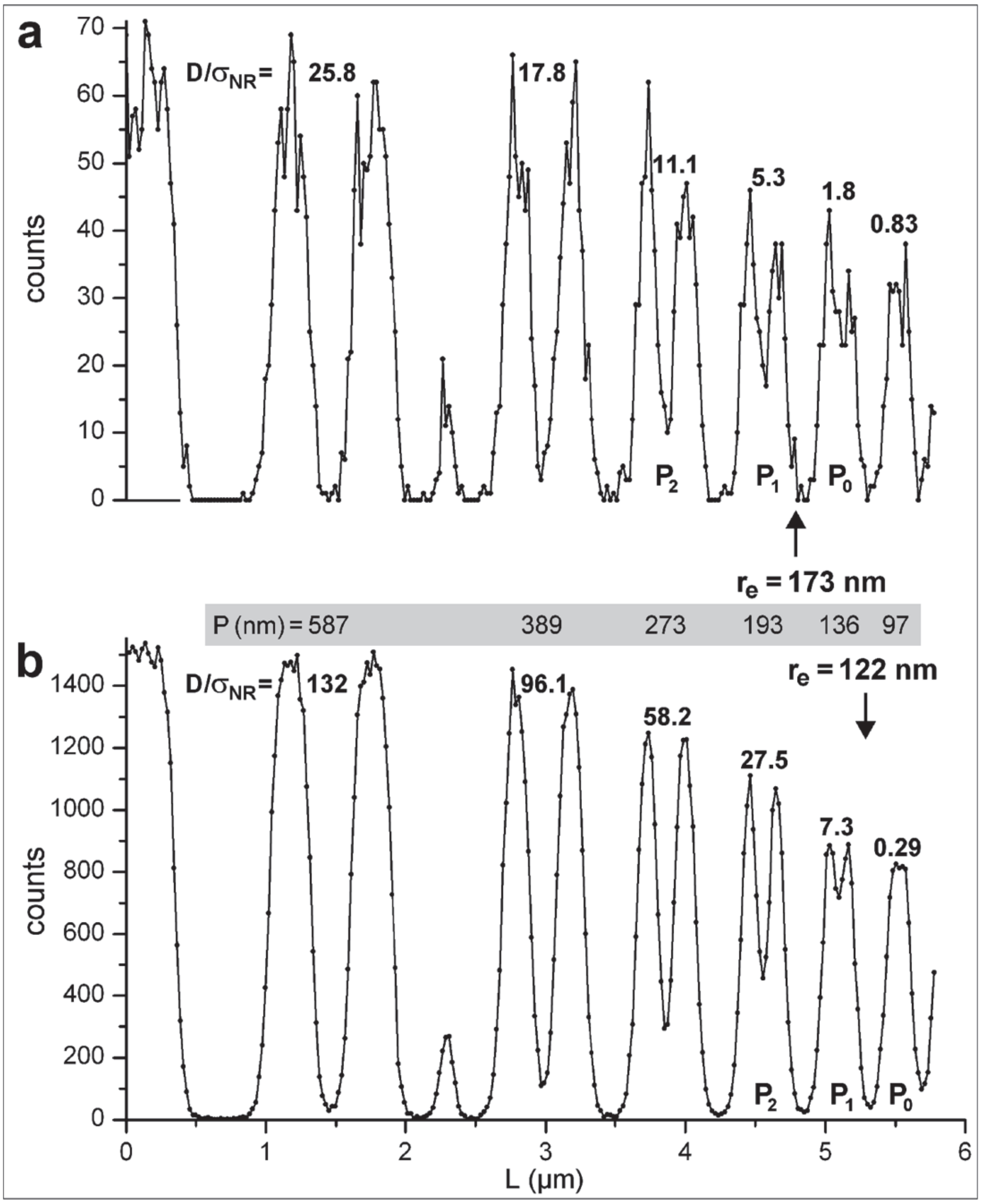

Figure 72 — Linescans created from sums of (a) 10 scanned lines (between the white lines in Figure 71) and b) all 256 lines of the 256 × 256 pixel^2 Al$^+$ map in Figure 71, respectively. For each linescan, values of D/σ_{NR} calculated according to Formula (36) are given. P_0, P_1 and P_2 designate the periods of the first non-resolved grating and the first and second resolved gratings, respectively. Grating periods P are given in the shaded bar between the linescans. The effective lateral resolution $\mathrm{r_e}$ has been calculated according to Formula (39)

5 Physical factors affecting lateral resolution, analysis area and sample area viewed by the analyser in AES and XPS

5.1 General information

A common need in AES and XPS is the measurement of composition as a function of position on the sample surface. Typically, an analyst wishes to determine the local surface composition of some identified region of interest. This region of interest could be a feature on a semiconductor wafer (such as an unwanted defect particle or contamination stain), a corrosion pit, a fibre, or an exposed surface of a composite material. With growing industrial fabrication of devices with dimensions on the micrometre and nanometre scales, particularly in the semiconductor industry[40] and for emerging nanotechnology applications, there is an increasing need to characterize materials using tools with lateral resolutions and dimensions of analysis areas that are smaller than those of the features of interest. It is generally necessary in these applications to be able to determine that devices have been fabricated as intended (quality control), to evaluate new or current fabrication methods (process development and process control), and to identify failure mechanisms (failure analysis) of a device during its service life or after exposure to different ambient conditions. The lateral resolution and the analysis area are important and related parameters in the application of characterization techniques such as AES and XPS for the surface characterization of materials containing features with micrometre and nanometre dimensions. Another parameter that is important in some measurements is the sample area viewed by the electron energy analyser. The needs for measurements of lateral resolution, analysis area, and sample area viewed by the analyser are described in the following sections.

As in optical[10][41]–[43] and various forms of electron microscopy,[12][44][45] the achievable lateral resolution is related to the contrast found in a measured image. It is pointed out, however, that the contrast transfer function is a useful means for describing the contrast in an image as a function of spatial frequency (cf. 4.1.5, 4.4.3[10][12][41]–[45]). At the highest detectable spatial frequency, the contrast approaches zero. The achievable lateral resolution in a particular AES or XPS measurement will therefore depend not only on the instrumental characteristics but on the available contrast (e.g. from the signals associated with two neighbouring chemical phases for a particular measurement time).

An overview is given in this chapter of certain instrumental and measured properties that are described in terms of Gaussian functions. This approach is believed to be a useful guide but it should be emphasized that the properties of real instruments and of real measurements can depart from the Gaussian model considered here (cf. 4.2.1). In addition, the detectability of a feature in AES and XPS measurements depends in part on the measure of lateral resolution of the instrument and in part on the difference in signal intensities for measurements made on and off the possible feature and the observation time (through the statistical variations in the signal intensities). The detectability of a feature thus depends on the contrast transfer function for the measurement and the measurement time. The specific results will thus be a function of both instrumental and sample properties. Reliable detection of a feature will also depend on instrumental stability (particularly the stability of the incident electron beam current in AES and the X-ray flux in XPS, and the positional stability of the sample stage with respect to the electron or X-ray beam) and the chemical stability of the sample during the time needed for acquisition of AES or XPS data.

5.2 Lateral resolution of AES and XPS

5.2.1 Introduction

It is clearly desirable that the lateral resolution of the technique be smaller than the lateral dimensions of the feature of interest in order that the feature can be reliably analysed. The feature of interest in an AES instrument might typically be initially detected in a scanning electron micrograph. The primary electron beam could then be positioned on the feature, and an Auger electron spectrum recorded. In XPS instruments, the feature of interest must generally be detected from an image or a line scan in which a particular signal (often the intensity of a selected photoelectron peak) is displayed as a function of position on the sample surface.

Many authors have described and discussed the lateral resolution (often referred to as spatial resolution) of AES and XPS instruments. Useful information can be found in a review by Cazaux[12] for AES and in a review by Escher et al.[46] for XPS.

Figures 73 to 75 show schematic diagrams of typical experimental configurations for AES and XPS. These Figures show the exciting radiation incident on the sample surface. For AES (Figure 73), an electron beam with an energy between 3 keV and 25 keV is focused to a “spot” on the sample surface. With a field-emission electron source, the full width at half maximum (FWHM) intensity of the focused spot may be between 5 nm (or even lower) and 50 nm depending on the beam energy and the beam current. The beam is scanned across a region of interest on the sample surface, and various signals collected (such as secondary-electron and Auger electron signals). The Auger electron signal arises from inner-shell ionisations caused in part by the incident beam and in part by backscattered electrons.[12] The lateral resolution in AES is mainly determined by the FWHM of the focused spot[12]; further details are given in 5.2.2.

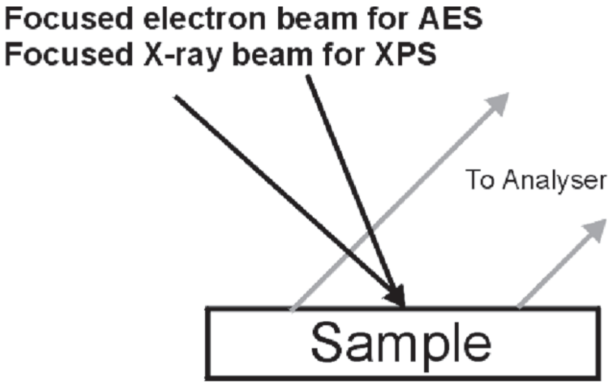

Figure 73 — Schematic outlines of experimental configurations for AES and XPS with a focused incident beam

Figure 73 also indicates an XPS configuration in which the incident X-ray beam is focused to a spot on the sample surface. With a conventional X-ray source and a bent-crystal focusing X-ray monochromator, the FWHM of the focused spot can be less than 10 µm. With a synchrotron source of X-rays and a zone-plate, the FWHM of the focused spot can be about 50 nm.[47] The experimental configurations for AES and XPS in Figure 73 are thus similar in that an incident beam is focused to a small area on the sample surface. Lateral variations of surface composition can thus be detected as the beam is positioned on different regions of interest, is linearly scanned across a selected region, or is rastered to obtain information from a selected area. If the incident beam in Figure 73 is not normally incident on the sample surface, the beam profile will be elliptical instead of circular. In such cases, the lateral resolution depends on the FHWM of the beam profile in two orthogonal directions (parallel and perpendicular to the plane of incidence).

Figure 74 a) illustrates an XPS configuration in which the electron energy analyser is part of an electron-optical configuration that views a selected single small area on the sample surface. The lateral resolution for this configuration depends on the electron-optical design and can be less than 10 µm. Figure 74 b) shows an XPS configuration in which the electron-optical system produces an image of a selected region of the surface. In this mode, different pixels of the image correspond to particular regions of the surface; information from multiple points on the surface can be recorded in parallel. Figures 74 a) and 74 b) are similar in that the regions of interest are selected by the electron-optical system. Lateral variations of surface composition can be detected, in principle, by mechanically moving the sample with respect to the analyser or, usually, by adjustment of the electron-optical system to select the particular regions of interest on the sample surface from which photoelectrons are detected. As for Figure 73, photoelectron signals can be obtained from a selected region, from multiple regions along a line, or from multiple regions within a selected area.

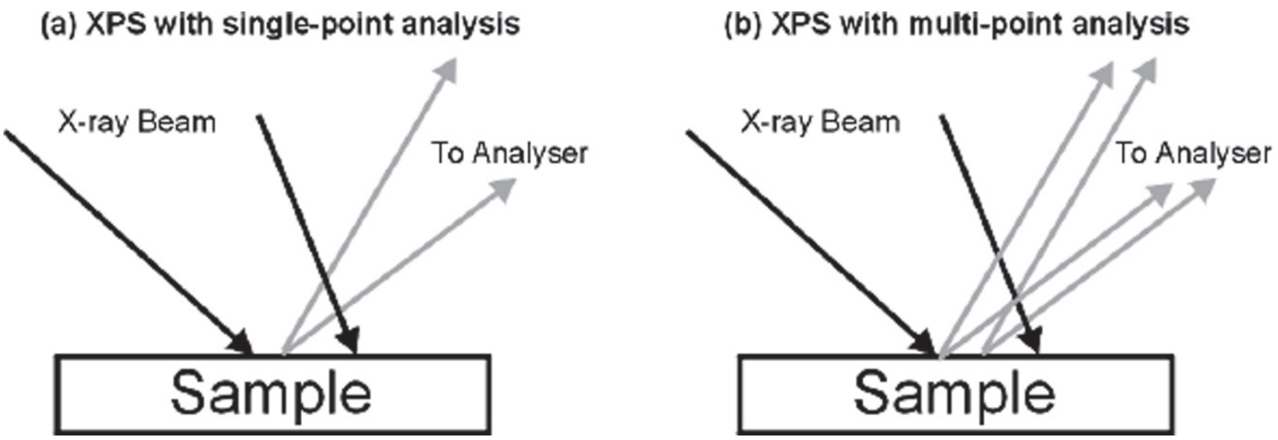

Figure 74 — Schematic outlines of XPS configurations in which (a) the analyser accepts photoelectrons from a selected area on the sample surface (single-point analysis) or (b) the analyser accepts photoelectrons from multiple regions on the sample surface to create an image of the surface (multi-point analysis)

Figure 75 shows a simpler XPS configuration in which the sample is irradiated by X-rays from a nearby X-ray source and photoelectrons are detected as in Figure 74 from an area defined by the electron-optical properties of the analyser. Unlike the configurations of Figure 74, however, the instruments represented by Figure 75 were not designed to detect lateral variations of surface composition except by movement of the sample with respect to the analyser. In this way, a lateral resolution of about 0,1 mm to 1 mm could be achieved.

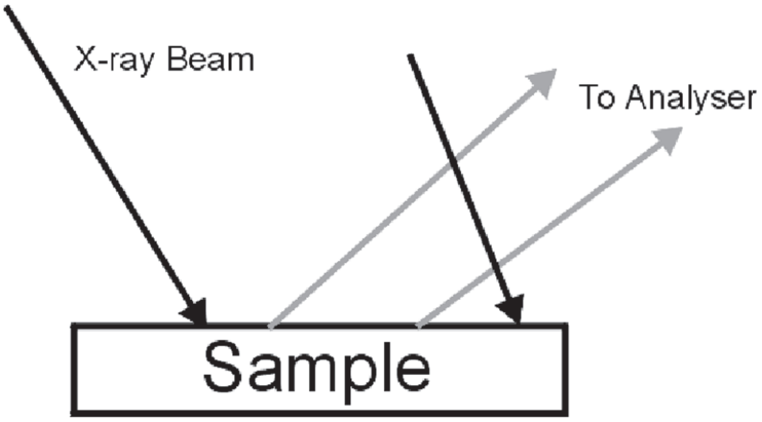

Figure 75 — Schematic XPS configuration in which the sample is irradiated by a broad X-ray beam and in which photoelectrons are accepted by the analyser from a larger area of the sample surface than for Figure 74

5.2.2 Lateral resolution for AES

For simplicity in the following discussion, it will be assumed that the sample has a plane surface and that the primary electron beam is normally incident on the sample. It is also assumed that the analysis area is smaller than the sample area viewed by the analyser and that the detection efficiency of the analyser is uniform within the analysis area.

Although the incident electron beam in AES can be focused to a spot with FWHM less than 50 nm, detected Auger electrons originate from ionisations caused by the incident beam and by backscattered electrons.[12,48] Due to multiple elastic- and inelastic-electron scattering, the backscattered electrons can cause inner-shell ionisations that lead to detected Auger electrons from sample regions of up to about 1 µm from the incident-beam spot. The intensity distribution $J_{\mathrm{A}}(r)$ of detected Auger electrons as a function of radius r can be described by the sum of two Gaussian functions (cf. 4.2.1 and[12,14,16,48]):

$$J_{\mathrm{A}}(r)=(I_{\mathrm{i}}/2\pi\sigma_{\mathrm{i}}^2)\exp(-r^2/2\sigma_{\mathrm{i}}^2)+[(R-1)I_{\mathrm{i}}/2\pi\sigma_{\mathrm{b}}^2]\exp(-r^2/2\sigma_{\mathrm{b}}^2) \tag{61}$$

or

$$J_{\mathrm{A}}(r)=J_{\mathrm{Ai}}(r)+J_{\mathrm{Ab}}(r) \tag{62}$$

where I_{i} is the incident beam current, σ_{i} is the Gaussian parameter describing the radial distribution of the incident electron beam, σ_{b} is the Gaussian parameter describing the radial distribution of backscattered electrons, R is the backscattering factor, and $J_{\mathrm{Ai}}(r)$ and $J_{\mathrm{Ab}}(r)$ are the radial intensity distributions for Auger electrons created by the incident beam and by backscattered electrons, respectively. The FWHM values for these two Gaussian functions are $2{,}35\sigma_{\mathrm{i}}$ and $2{,}35\sigma_{\mathrm{b}}$, respectively.

Seah[49] has shown that, with 20 keV incident electrons, the FWHM values for backscattered electrons vary between about 0,2 µm and 3,0 µm for different elements; values of σ_{b} thus range from about 0,085 µm to about 1,3 µm. As an illustrative example, Figure 76 shows a plot of $J_{\mathrm{A}}(r)$ with σ_{i} = 10 nm, σ_{b} = 200 nm, and R = 1,5; for simplicity, $J_{\mathrm{A}}(r)$ has been normalized to unity at r = 0. Because $\sigma_{\mathrm{b}} > > \sigma_{\mathrm{i}}$, $J_{\mathrm{Ai}}(r=0)$ is about three orders of magnitude greater than $J_{\mathrm{Ab}}(r=0)$ in this example. It is thus possible for the lateral resolution to be determined mainly by the value of σ_{i} although, as will be shown, the magnitude of $J_{\mathrm{Ab}}(r)$ in the vicinity of $r=0$ also affects the lateral resolution.

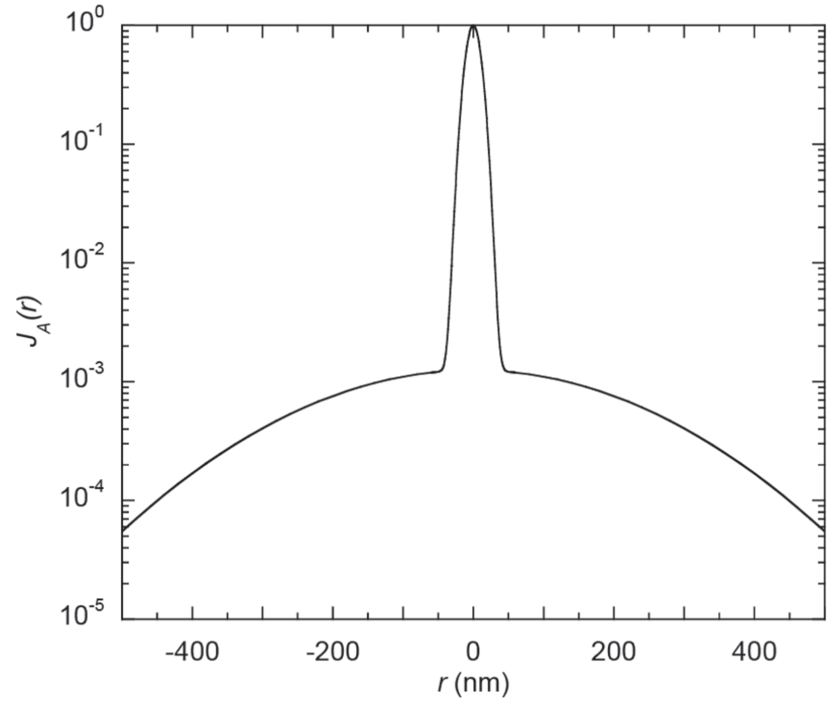

Figure 76 — Plot of the total Auger electron intensity distribution $J_{\mathrm{A}}(r)$ **(normalized to unity at** r = 0**) from Formula (61) as a function of** r **with** σ_{i} = 10 nm**,** σ_{b} = 200 nm**, and** R = 1,5

The lateral resolution in AES has often been determined by scanning the primary electron beam across a sufficiently sharp chemical gradient (a chemical edge) in the plane of the sample; the scan direction is normal to the chemical edge in such measurements. The Auger electron intensity, *I*, for one of the materials is then measured as a function of beam position on the sample. In common practice lateral resolution, Δ*r*, has been variously defined as the distance $D_{\mathrm{x-(100-x)}}$ over which the intensity *I* changes from 25 % to 75 % of its maximum value, $I_{\max}$, the distance over which I changes from 20 % to 80 % of $I_{\max}$, the distance over which I changes from 16 % to 84 % of $I_{\max}$, the distance over which I changes from 12 % to 88 % of $I_{\max}$, and the distance over which I changes from 10 % to 90 % of $I_{\max}$ (cf. 4.3.2 and[4,48]).

The intensity distribution of detected Auger electrons shown in Formula (61) can also be written in Cartesian coordinates.[14,48] It is then possible to calculate the change in detected Auger intensity as the primary beam is scanned across an abrupt chemical interface as in the experiments. Figure 77 shows a plot of $I/I_{\max}$ as a function of scan distance for the same parameters used in Figure 76. While there is a steep increase in the value of $I/I_{\max}$ in the vicinity of the origin in Figure 77 (corresponding to the primary-beam component $J_{\mathrm{Ai}}(r)$ in Figure 76), there are significant tails in the plotted $I/I_{\max}$ due to the backscattered-electron component $J_{\mathrm{Ab}}(r)$ in Figure 76.

In the example of Figure 77, the measures of the lateral resolution are about 15 nm, 22 nm, 32 nm, 102 nm, and 150 nm for the 25 % to 75 %, 20 % to 80 %, 16 % to 84 %, 12 % to 88 %, and 10 % to 90 % Auger intensity changes, respectively. It is clear that this measure of lateral resolution is mainly determined by the FWHM of the primary beam [that is, the parameter σ_{i} in Formula (61)] if, in this example, the measure of lateral resolution is found from the distances corresponding to the 25 % to 75 %, 20 % to 80 %, and 16 % to 84 % Auger electron intensity changes (although, as will be shown shortly, these measures of lateral resolution also depend weakly on σ_{b} and R). In contrast, the measure of lateral resolution is a strong function of all three parameters in Formula (61) (σ_{i}, σ_{b}, and R) if the measure of lateral resolution is found from the distances corresponding to the 12 % to 88 % and 10 % to 90 % Auger electron intensity changes. Since the values of σ_{b} and R depend on the sample and the primary electron energy,[44][50] it is desirable for a measure of lateral resolution in AES to be determined in a way that is least dependent on the sample properties. It is therefore recommended that the lateral resolution be obtained from the distances corresponding to the 25 % to 75 % Auger electron intensity changes in a scan such as that shown in Figure 77.

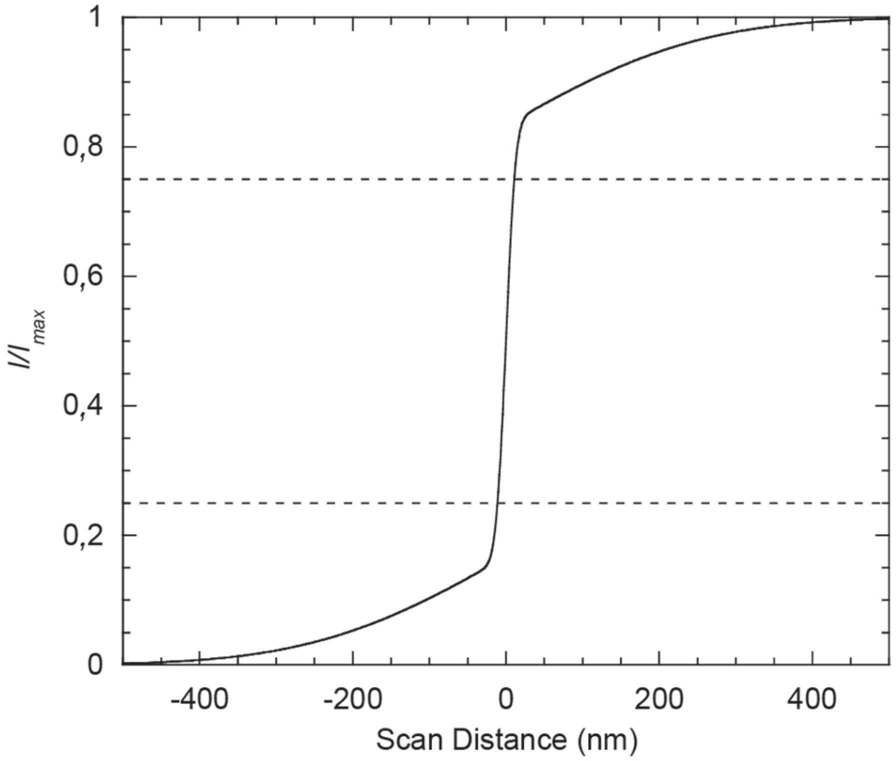

Figure 77 — Plot of the ratio of the calculated Auger electron intensity, I, to the maximum Auger electron intensity, I_{max}, as a function of scan distance as the primary beam is scanned across a sharp chemical boundary located at the origin (with the beam and backscattering parameters used in Figure 76. (In this example, I/I_{max} is plotted for the material on the right-hand side of the edge. The horizontal dashed lines show $I/I_{\text{max}} = 0{,}25$ and $I/I_{\text{max}} = 0{,}75$. A measure of lateral resolution can be determined from the difference between the scan distances for these values of I/I_{max}; in this example, it is about 15 nm)

Seah[14] has shown that the measure of the lateral resolution, $\delta r(50)$, corresponding to the 25 % to 75 % change in Auger electron intensity across an abrupt chemical edge can be determined from the relation:

$$0{,}5R = \text{erf}[z(\sigma_\text{i})] + (R-1)\text{erf}[z(\sigma_\text{b})] \quad (63)$$

where erf(z) is the error function defined by:

$$\text{erf}(z) = (2/\sqrt{\pi})\int_0^z \exp(-t^2)dt \quad (64)$$

and where $t = \delta r(50)/\sqrt{2}\sigma_i$ and $t = \delta r(50)/\sqrt{2}\sigma_b$ for the first and second terms in Formula (63), respectively. Figure 78 shows plots of $\delta r(50)/\sigma_\text{i}$ versus $\sigma_\text{b}/\sigma_\text{i}$ for four values of the backscattering factor R. These plots show that the value of $\delta r(50)/\sigma_\text{i}$ does not vary appreciably with $\sigma_\text{b}/\sigma_\text{i}$ when the latter ratio is greater than about 20. The value of $\delta r(50)/\sigma_\text{i}$ does, however, depends on R although $\delta r(50)/\sigma_\text{i}$ is between 1,35 (when R = 1) and about 3,1 (when $R = 1{,}8$). If, however, the measure of the lateral resolution was determined from the 10 % to 90 % changes in Auger electron intensity across an edge, Cazaux has shown that this measure changes almost linearly with $\sigma_\text{b}/\sigma_\text{i}$ and with a slope that depends on the value of R.[48]

Besides scattering also aberration of the incident electron beam caused by the focusing electron optics is a factor affecting lateral resolution. Aberration phenomena influence the radial distribution of the incident electrons described by σ_i. The radial distribution depends on beam energy and beam current used for imaging.[51]

The results shown in Figures 76 to 78 were for normal incidence of the primary electron beam. Cazaux[48] has made similar analyses for primary beams at non-normal incidence. The results of these model calculations agree well with experimental measurements and with Monte Carlo simulations of Auger electron production by backscattered electrons.[48][52] Cazaux[12] has also considered the detectability of features in the form of stripes in the plane of the surface and has examined Auger electron intensity profiles for chemically non-abrupt edges. El Gomati et al.[53] have shown the importance of edge effects in Auger electron line profiles when the primary electron beam was scanned across metal lines with sharp rectangular cross sections; good agreement was found between the experimental profiles and those obtained from Monte Carlo simulations.

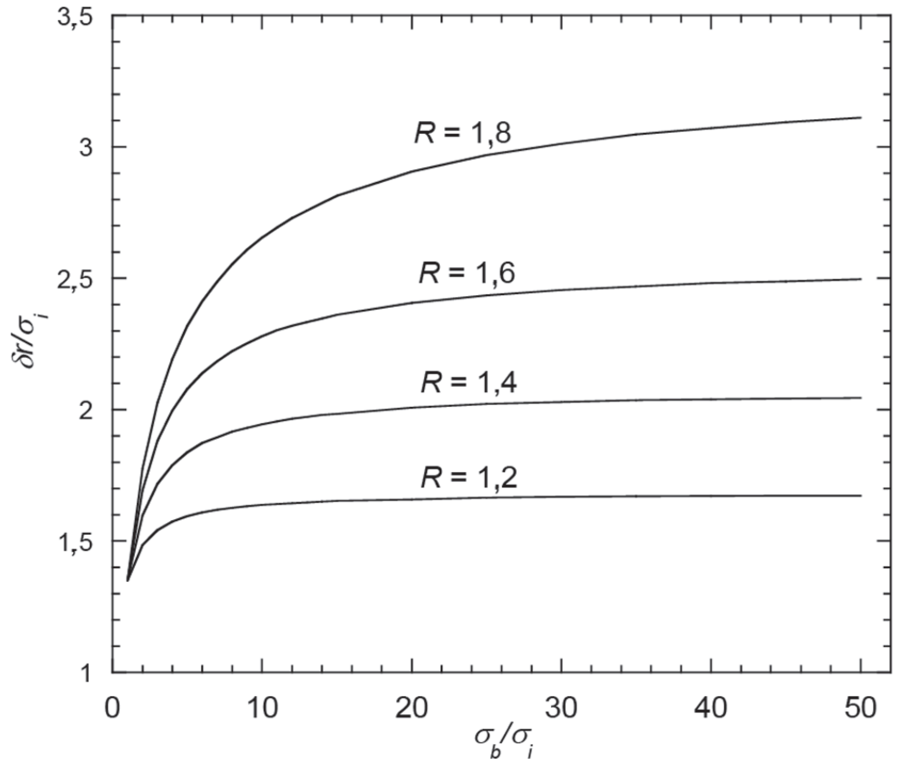

Figure 78 — Plot of $\delta r(50)/\sigma_\mathrm{i}$ versus $\sigma_\mathrm{b}/\sigma_\mathrm{i}$ for the indicated values of the backscattering factor R

5.2.3 Lateral resolution for XPS

The lateral resolution for XPS can be described in a similar way as for AES, except there is no backscattering effect. A single Gaussian function can be used to describe the intensity-position distribution of a focused X-ray beam on the sample surface for an XPS instrument of the type illustrated in Figure 73 or the intensity-position response of the electron-optical system for an XPS instrument of the types shown in Figure 74.

Baer and Engelhard[54] reported measurements of analysis areas (discussed in 5.3.3) for two XPS instruments, one having a focused X-ray beam incident on the sample surface as in Figure 73 and the other having an electron-optical system to select a small area of interest on the sample surface as in Figure 74 a). They measured the lateral resolution δr of their instruments to be between 9 µm and 200 µm for different instrumental settings from the distances between the 16 % and 84 % intensity points across an edge between two materials of different compositions. For these instruments, the lateral resolution could be described by a Gaussian function although other functions (a Lorentzian function, a function with a constant central intensity and sharp edges, a function with a $1/(1+|r|^3)$ intensity distribution, and a function with a constant intensity for small radii and $1/(1+|r|^3)$ tails] gave essentially similar results.

5.3 Analysis area

5.3.1 Introduction

After detection of a feature of interest in an AES or XPS instrument, it is often desired to analyse the AES or XPS data in order to obtain elemental and chemical information on the feature. For such data, it is important to know the analysis area so that the AES or XPS data can be reliably analysed. We now describe the factors that affect the analysis area for the AES and XPS configurations shown in Figures 73 and 74. It will again be assumed that the sample has a plane surface and that the analysis area is smaller than the sample area viewed by the analyser.

5.3.2 Analysis area for AES

Consideration is again given to the Auger electron intensity distribution of Formula (61) and the illustrative example in Figure 73 showing $J_A(r)$ versus r for σ_i = 10 nm, σ_b = 200 nm, and R = 1,5. The ratio of the total Auger electron intensity, I, from a circular area of radius r_{max} to the total Auger electron intensity, I_{max}, from a circular area of infinite radius can be found by integrations of Formula (61):

$$\frac{I}{I_{\text{max}}}=\frac{\int_0^{r_{\text{max}}} rJ_{\text{A}}(r)dr}{\int_0^{\infty} rJ_{\text{A}}(r)dr}=\{[1-\exp(-r_{\text{max}}^2/2\sigma_i^2)]+(R-1)[1-\exp(-r_{\text{max}}^2/2\sigma_{\text{b}}^2)]\}/R \qquad (65)$$

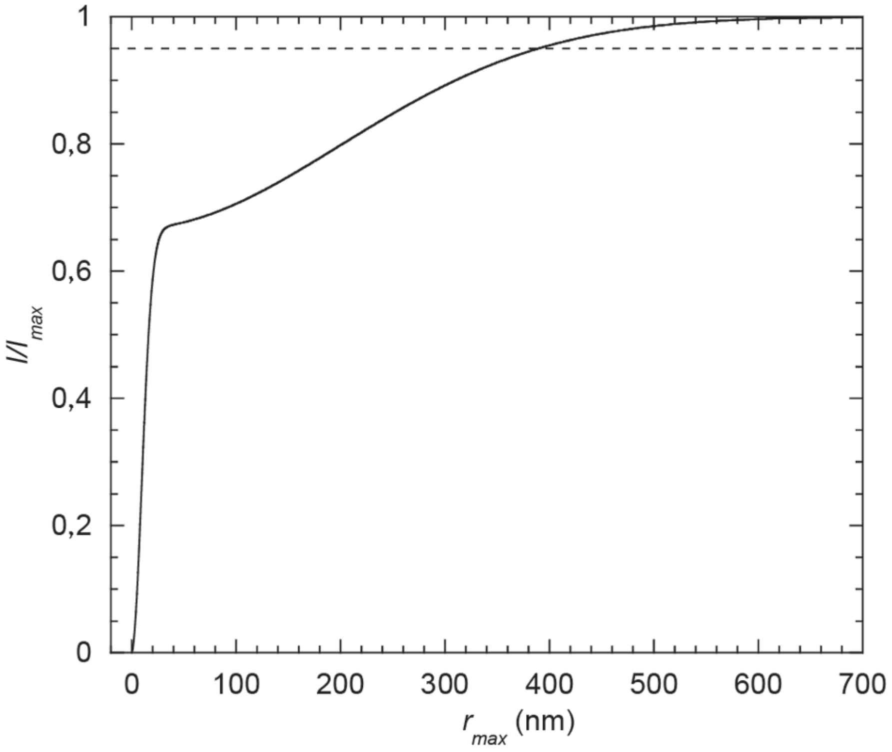

Figure 79 — Plot of I/I_{max} versus r_{max} from Formulae (61) and (65) with the same parameter values as for Figure 76 (The horizontal dashed line shows I/I_{max} = 0,95, for which the corresponding value of r_{max} is 390 nm)

Figure 79 shows a plot of I/I_{max} from Formula (65) as a function of r_{max} for the same parameter values selected for Figure 76. As expected, the intensity distribution in Figure 79 consists of two regions. Two-thirds of the total intensity is due to Auger electrons created by the primary beam while the remaining one-third is due to backscattered electrons. Approximately 28 % of the total intensity comes from an area of radius 10 nm (the value of σ_i in this example), about 59 % from an area of radius 20 nm, and about 66 % from an area of radius 30 nm. The remaining intensity comes from a much larger area, with 90 %

from an area of radius about 310 nm, 95 % from an area of radius about 390 nm, and 99 % from an area of radius about 530 nm. Thus, while the lateral resolution δr(50) is about 15 nm for this example, about two-thirds of the total Auger intensity comes from an area of radius 30 nm (double the lateral resolution) while 95 % of the total intensity comes from an area of radius 390 nm (26 times the lateral resolution). The intensity from this larger area needs to be considered in interpretations of line scans and of "point" analyses (with the incident beam at a fixed location on the sample surface). In general, the analysis area will depend on the relevant material parameters (σ_b and R) and on the particular percentage chosen in the operational definition for the analysis area (percentages of 90 %, 95 % and 99 % of the total Auger intensity were used as examples here). It should also be emphasized that Formula (61) is only expected to be a useful guide when the primary beam is normally incident on the sample surface. For other angles of incidence, analytical expressions[48] can be utilized or Monte Carlo simulations[50,52,53] can be performed to determine the analysis area. Monte Carlo calculations would be required if the sample of interest consisted of materials with significantly different values of σ_b and R.[53] Finally, the Gaussian expression for the incident-beam profile in Formula (61) may not be realistic for some instruments.[40]

5.3.3 Analysis area for XPS

Baer and Engelhard[54] described measurements made with a test sample that had a series of circular spots with diameters between 2 µm and 100 µm. The spots consisted of an indium-tin-oxide coating while the surrounding material was a chromium-containing compound. If the XPS instruments were adjusted to obtain data from the centre of a spot, Baer and Engelhard found that the spot radius had to be about four times δr to obtain 80 % of the maximum signal for the spot material that could be measured for much larger spot radii. These results were interpreted in terms of a function describing the spatial distribution of X-ray intensity on the sample surface (for the instrument represented by Figure 73) and a similar function describing the spatial selectivity for the detection of photoelectrons emitted from the sample surface [for the instrument represented by Figure 74 a)]. While a Gaussian function has been conventionally used to describe the intensity-position functions for these two types of XPS instruments, Baer and Engelhard found that such a function was inadequate for their instruments. Instead, they were able to describe their spot-intensity measurements with either an $1/(1+|r|^3)$ intensity-position function or a function consisting of a constant intensity for small radii and $1/(1+|r|^3)$ tails. These functions had higher intensities in the tail regions (that is, for $r > > \Delta r$) than a Gaussian function representing the same value of Δr. It is thus clear that the analysis area for these instruments would be about $10\pi(\delta r)^2$ if the analysis area was defined to include 94 % of the total photoelectron signal. Baer and Engelhard pointed out that the extent of non-Gaussian behaviour (that is, the intensity of the tails in the intensity-position function for an XPS instrument) could be highly dependent upon lens operation and set-up parameters.[54]

Scheithauer[55] reported an alternative kind of procedure and test sample for the determination of the analysis area of an XPS instrument represented by Figure 73. The approach is also useful for the characterization of XPS instruments represented by Figure 74. The test samples are called "inverse dots" and are actually platinum apertures known from electron microscopy with different diameters between 50 µm and 600 µm. When the axis of the X-ray beam is centred within the Pt aperture, the measured Pt photoelectron intensity represents the total photoemission excited at areas outside the hole. Variation of the diameter of the aperture and one measurement of the respective maximum photoelectron intensity remote from the hole enable a quantitative characterization of the real X-ray beam shape including long-tail signal contributions in all directions in terms of Pt count rates normalized to the maximum count rate. As a result, the size of a sample feature necessary to reduce the signal contribution from outside the feature below a selected percentage (e.g. 1 %) can be determined for selected X-ray beam settings This knowledge is essential to ensure a reliable detection of minor components on small sample features such as bond pads, etc. The use of apertures has some advantages over micro-structured circular patterns and "chemical edges". First, no assumption about the primary X-ray beam profile is necessary. Second, independent from the exact in-plane X-ray beam profile, the long-tail signal contributions in all directions are measured when the primary X-ray beam is centred in the aperture. And third, if the apertures are cleaned by sputtering, redeposited material is not detected by the energy analyser.

5.4 Sample area viewed by the analyser

For the instruments represented by Figure 73, the analysis area is defined by the incident electron beam or the incident X-ray beam and, for AES, by sample properties as described in 5.3.1. The electron energy analyser in these instruments is designed to view a larger area of the sample surface so that particular regions of interest of different areas, up to some maximum area given by the analyser design and settings, can be viewed in the imaging or line-scan modes of the instruments. It may be necessary for some applications to measure the sample area viewed by the analyser that can depend on experimental conditions such as electron energy, analyser pass energy, choice of apertures, and sample alignment in the instrument.

The sample area viewed by the analyser is particularly important for XPS instruments represented by Figure 75. The sample surface here is irradiated by a broad X-ray beam (often of about 1 cm diameter), and photoelectrons are detected from a sample area defined by the analyser design, the analyser settings, and the extent of any sample misalignment. For such instruments, the analysis area is the sample area viewed by the analyser.

Three groups have reported measurements of the sample area viewed by the analyser for XPS instruments.[56-60] A focused electron beam from an available electron gun was rastered across the sample surface and measurements were concurrently made of a selected analyser signal, generally the intensity of elastically scattered electrons, as a function of the position of the electron beam on the surface. Measurements of this type have been reported for different types of electron energy analysers, for various analyser settings, and for particular sample misalignments.[56-60] As an example, Figure 80 shows illustrative elastic-peak images for a double-pass cylindrical-mirror analyser operated at electron energies of 100 eV, 500 eV, and 1000 eV.[58] The sample area viewed by the analyser can be determined from these images for a specified percentage of the total analytical signal.

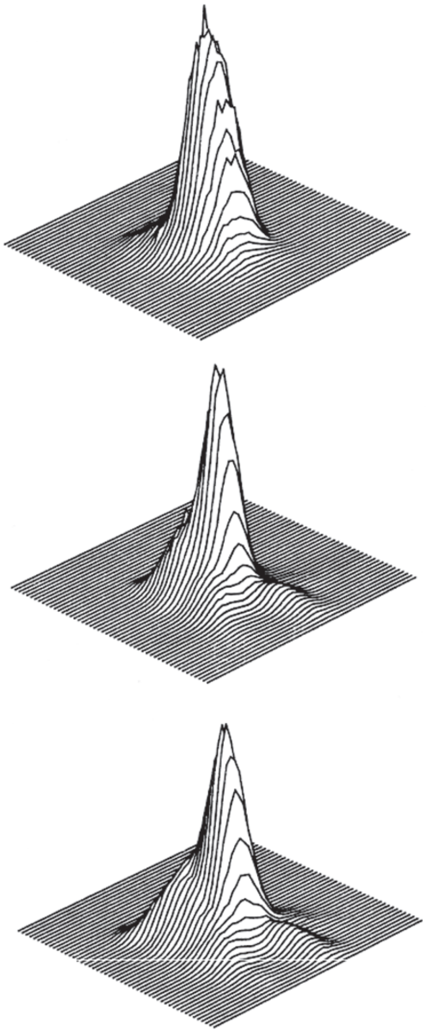

NOTE Elastic-peak images were recorded for an analyser pass energy of 50 eV and for electron energies of 100 eV (top), 500 eV (centre), and 1000 eV (bottom). The horizontal distance scanned by the electron beam on the sample surface (corresponding to the bottom left to right line scan in each image) was 13 mm and the vertical distance was 15 mm.

Figure 80 — Examples of electron elastic-peak images obtained with a double-pass cylindrical-mirror electron energy analyser in an XPS instrument[58]

The importance of adequate alignment of the sample surface with respect to the X-ray source and electron energy analyser of an XPS instrument has been pointed out by Seah et al.[61] For some XPS instruments, the sample area viewed by the analyser is independent of the electron energy while for other instruments this area depends on electron energy. In the latter class of instruments, it is important that the sample be aligned correctly at the smallest sample area viewed by the analyser. This condition generally corresponds to the highest electron energy that is to be measured.

6 Measurements of analysis area and sample area viewed by the analyser in AES and XPS

6.1 General information

Information on measurements of lateral resolution in AES is given in References [12],[38],[46],[49],[50],[59] and[60] together with references therein. For test samples consisting of steps, Monte Carlo calculations may need to be performed to separate chemical and topographic effects.[53] Reimer[44] has discussed aspects of resolution tests in scanning electron microscopy and Cazaux[12,48,62] has described corresponding tests in scanning Auger-electron microscopy. Cazaux[12] also points out that fluctuations in Auger-electron intensity due to variations in sample topography can complicate determinations of lateral resolution. Postek et al.[64,65] have developed an objective procedure for determining the "sharpness" of images obtained by scanning electron microscopy. Briefly, a two-dimensional Fourier transform is made of an image, and an evaluation is made of the resulting frequency components. This approach can also be used to check and optimize the focus and astigmatism of the incident electron beam.

Information on measurements of lateral resolution in XPS is given in reference [54]. Seah and Smith[66] have described a means for optimising the lateral resolution on XPS instruments not equipped with an imaging system but which have an auxiliary electron gun to produce a focused electron beam on the sample. Briefly, a line profile of a suitable feature can be observed with the electron beam (for example, an Auger electron profile). By adjusting the analyser optics and reducing the lens aperture, one can optimize the lateral resolution. These settings can then be used for XPS measurements.

Measurements of lateral resolution on AES and XPS instruments represented by Figures 73 and 74 can be made with test samples having known lateral dimensions such as electron microscope grids or cross-sectioned layer stacks ([67] and cf. Figure 48). Other suitable test samples are gold islands on a carbon substrate or distinct edges or steps between two different materials. The gold islands/carbon substrate test sample is attractive for AES because the effects of backscattered electrons on the lateral resolution should be negligible with a substrate of low atomic number. Compositional gradients (in the plane of the sample surface) of the test samples should occur over lateral distances much smaller than the expected lateral resolution.

6.2 Analysis area

Measurements of analysis area on AES and XPS instruments represented by Figures 73 and 74 can be made with test samples in the form of circular spots of known diameters, as used by Baer and Engelhard for XPS instruments[54] or with a selection of platinum apertures as used by Scheithauer.[55] The minimum spot diameter should be $2\delta r$. For AES, the maximum spot diameter should be selected based on estimated or calculated values of σ_b and R; it is recommended that the maximum spot diameter be at least $4\sigma_b$. For XPS, the results of Baer and Engelhard indicate that the maximum spot diameter should be approximately $20\delta r$.

The incident electron or X-ray beam should be centred in turn on spots of different diameters (for instruments represented by Figure 73) or the electron-optical system should be adjusted to select photoelectrons from the centres of spots of different diameters (for instruments represented by Figure 74). Measurements should be made of selected Auger electron or photoelectron intensities as a function of spot diameter.[54] A plot should then be made of the selected intensity as a function of spot diameter in order to determine the analysis area corresponding to a particular percentage in the definition of analysis area. Information on measurements of this type for XPS instruments is given in reference [52].

Measurements using "inverse dot" test samples (commercial platinum apertures) should be made with the axis of the X-ray beam centred within each hole of a series of apertures with selected diameters. The measured Pt 4f photoelectron intensity originating from the aperture represents the photoemission excited at areas outside the aperture. A plot should then be made of those intensities normalized to the respective maximum photoelectron intensity measured remote from the hole as a function of hole diameter in order to determine the analysis area corresponding to a particular percentage in the definition of analysis area. Information on measurements of this type for an XPS instrument represented by Figure 73 is given in reference [55].

Similar procedures should be applicable to AES.

Measurements of analysis area should be made at different electron energies to determine whether the analysis area for one energy was the same as for another energy and whether these areas coincided. These tests should be made for the analyser conditions (that is, pass energy or retardation ratio and aperture sizes) in common use.

6.3 Sample area viewed by the analyser

Measurements of the sample area viewed by the analyser are most conveniently performed on instruments equipped with an electron gun that can be operated to produce a focused electron beam on the sample surface that can be rastered across the expected sample area viewed by the analyser.[56-60] On such instruments, measurements are made of the intensity of elastically scattered electrons of different selected energies as a function of electron-beam position on the surface. Procedures for such measurements are described in an ASTM standard practice.[68]

Measurements of sample area viewed by the analyser can be readily made with the ASTM standard practice on AES instruments. Similar measurements can be made on XPS instruments in which a suitable auxiliary electron gun is available or can be mounted, in which the sample area irradiated by X-rays is larger than the specimen area viewed by the analyser (as represented by Figure 75), and in which the photoelectrons travel in a field-free region from the sample to the analyser entrance apertures.

For XPS instruments represented by Figures 73 and 74, it may be possible to make measurements of the sample area viewed by the analyser by following a procedure analogous to the ASTM standard practice.[68] It is suggested that test samples of copper, silver, and gold be positioned in turn in the XPS instrument, and that measurements be made of the Cu $2p_{3/2}$, Ag $3d_{5/2}$, and Au $4f_{7/2}$ photoelectron intensities, respectively, as the X-ray beam is rastered across the sample surface (for instruments represented by Figure 73) or as the electron-optical system is adjusted to produce similar scans (for instruments represented by Figure 74). The scan range for such measurements clearly has to be large enough to allow photoelectron intensities to be measured from the entire sample area viewed by the analyser, and preferably larger than this area so that images similar to Figure 80 can be produced.

Another possible approach for measuring the sample area viewed by the analyser at relatively low electron energies for XPS instruments represented by Figure 73 is to mount a test sample of aluminium or silicon and to bombard this test sample with a focused beam of argon ions (for example, from the ion gun that may be used for sputter cleaning or sputter-depth profiling). Ion bombardment of this type produces relatively intense Auger electron features with energies less than 100 eV.[69] The ion beam should be rastered across the sample surface and measurements made of the intensity of a selected low-energy Auger-electron peak as a function of ion-beam position on the surface in a manner similar to that described in the ASTM standard practice.[68] This approach may, however, give misleading results because of the presence of stray magnetic fields. The area of analysis will then shift as the electron kinetic energy is reduced, particularly for energies less than about 200 eV. In such situations, it will not be possible to optimize the analysis position and to adjust the lens settings of the analyser for optimum focus.

Annex A
(informative)

Reduction of image period for 3-stripe gratings

For 3-stripe gratings (A-B-A) the image period may be smaller than the period of the object grating (cf. 4.4.1.1 and Figure A.1). This effect depends on the ratio of LSF width w_{LSF} to the object grating period P. Table A.1 and Figure A.2 show the systematic relation between the ratio w_{LSF}/P and the normalized reduction of image period for Gaussian and Lorentzian LSFs. Due to the long tails of the Lorentzian LSF the reduction of image period begins far from the limit of lateral resolution.

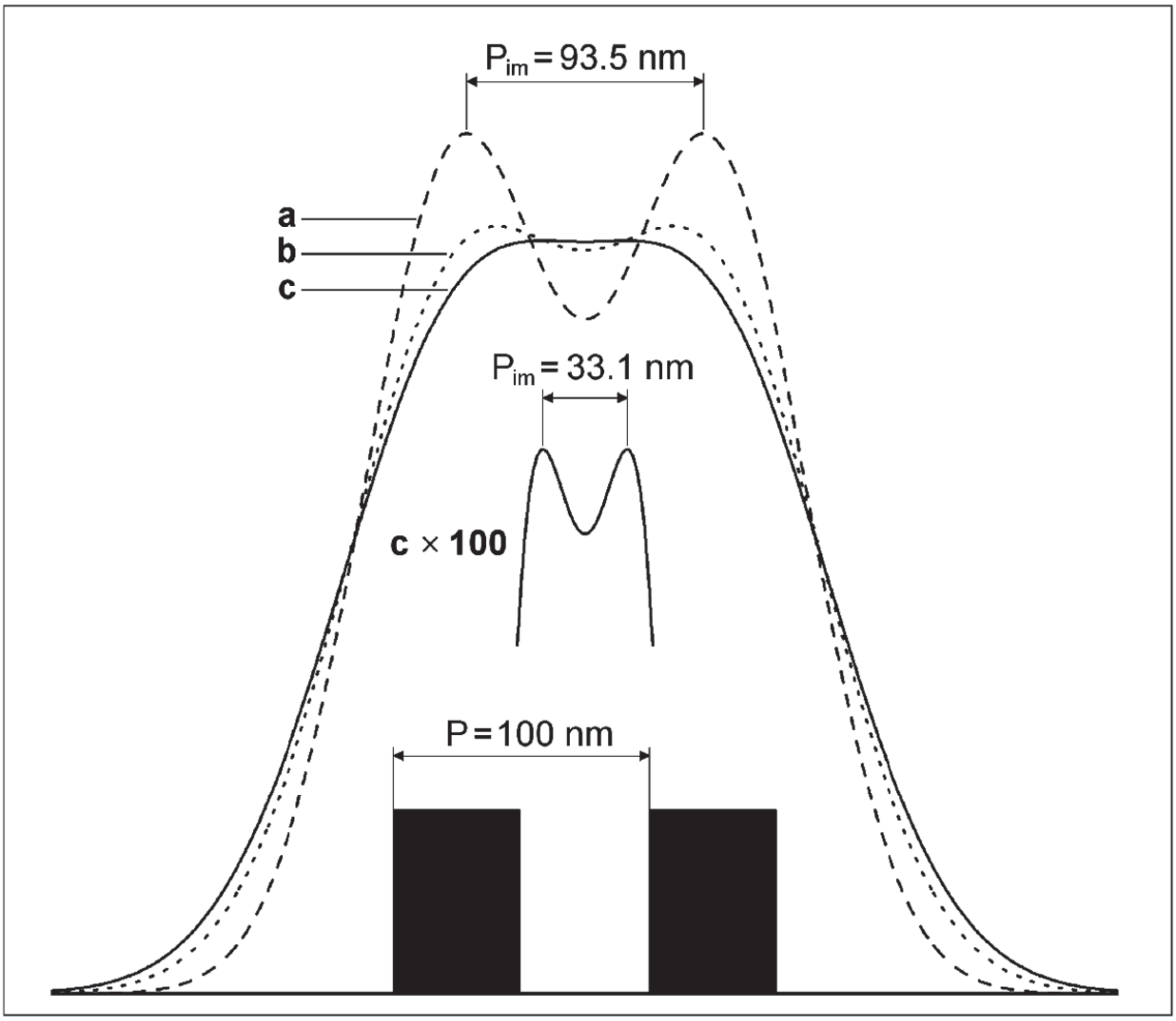

Figure A.1 — Reduction of image period P_{im} compared to the period of the object grating P. Imaging of a 3-stripe square-wave grating with a period of 100 nm is simulated by convolution with Gaussian LSFs of different widths: *a* – w_{LSF} = 80 nm; *b* – w_{LSF} = 100 nm; *c* – w_{LSF} = 110 nm. **Image profile** *c* **is shown additionally on an elongated intensity scale**

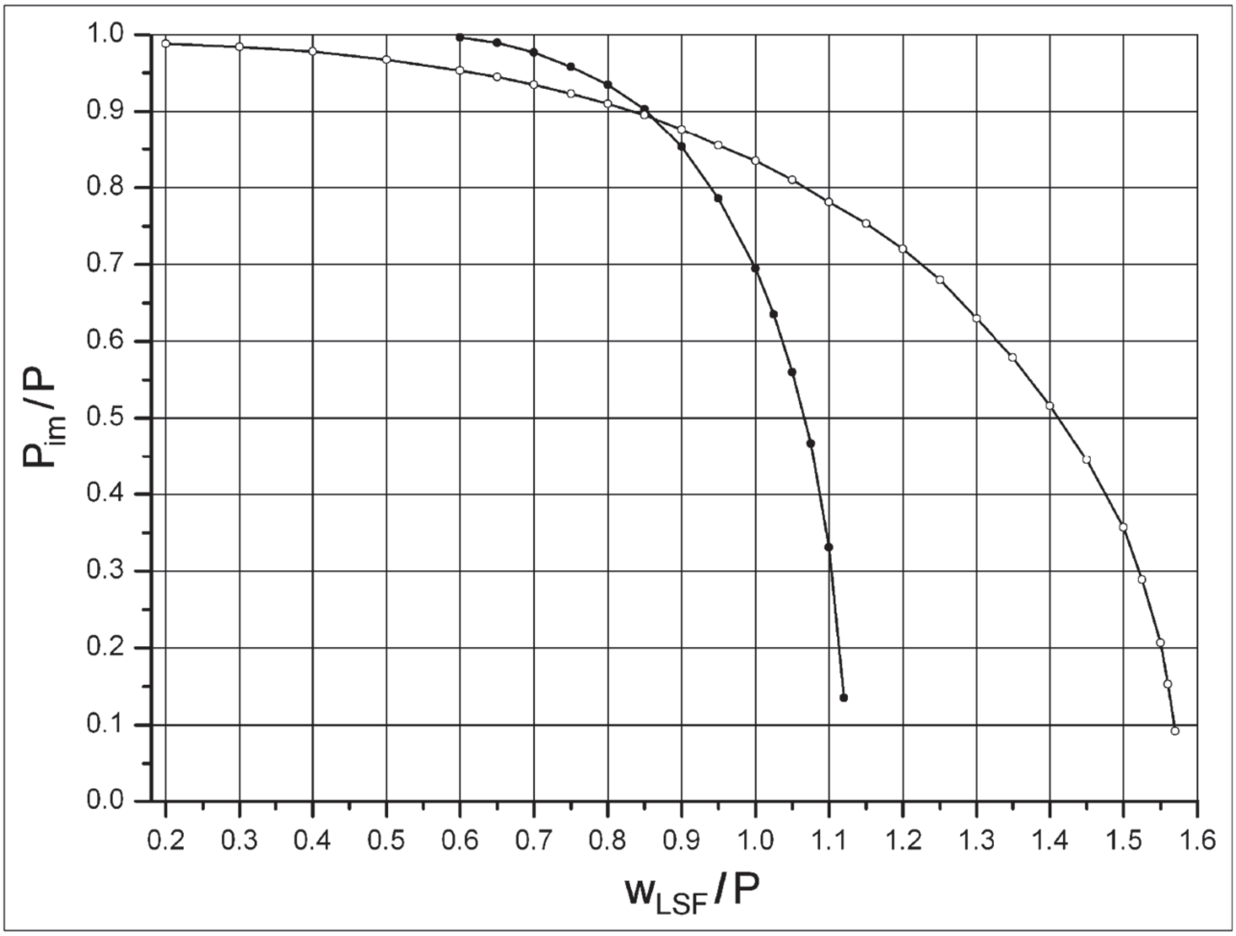

Figure A.2 — Relation between the normalized width of the LSF w_{LSF}/P and the reduction of the normalized image period P_{im}/P for Gaussian and Lorentzian model functions for the LSF. Open symbols – Lorentzian LSF; closed symbols – Gaussian LSF

Table A.1 — Relation between the normalized width of the LSF w_{LSF}/P and the reduction of the normalized image period for Gaussian and Lorentzian model functions for the LSF

w_{LSF}/P	P_{im}/P	
	Gaussian	Lorentzian
0.2		0.988
0.300		0.984
0.400		0.978
0.500		0.967
0.600	0.996	0.953
0.650	0.989	0.945
0.700	0.977	0.935
0.750	0.958	0.923
0.800	0.935	0.91
0.850	0.903	0.895
0.900	0.853	0.876
0.950	0.786	0.855
1.000	0.695	0.835
1.025	0.635	
1.050	0.560	0.81
1.075	0.467	
1.100	0.331	0.781
1.120	0.1350	
1.150		0.753
1.200		0.72
1.250		0.68
1.300		0.63
1.350		0.579
1.400		0.516
1.450		0.445
1.500		0.357
1.525		0.289
1.55		0.207
1.56		0.153
1.57		0.092

Bibliography

[1] Abbe E. Beiträge zur Theorie des Mikroskops und der mikroskopischen Wahrnehmung, *Schultzes Archiv für mikroskopische Anatomie*, 1873, vol. IX, pp. 412-468

[2] Lord Rayleigh. Investigations in optics with special reference to the spectroscope. 1. Resolving, or separation power of optical instruments. *Philos. Mag.* 1879, **8** pp. 261–274

[3] ISO 22493:2008, *Microbeam analysis — Scanning electron microscopy — Vocabulary*

[4] ISO 18516:2006, *Surface chemical analysis — Auger electron spectroscopy and X-ray photoelectron spectroscopy — Determination of lateral resolution*

[5] Senoner M., Wirth Th., Unger W., Österle W., Kaiander I., Sellin R.L. et al. BAM-L002 - A new type of certified reference material for length calibration and testing of lateral resolution in the nanometre range. *Surf. Interface Anal.* 2004, **36** pp. 1423–1426

[6] *BAM-L200 certificate* available at<http://www.rm-certificates.bam.de/de/rm-certificates_media/rm_cert_layer_and_surface/bam_l200e.pdf>

[7] Sparrow C.M. On spectroscopic resolving power. *Astrophys. J.* 1916, **44** pp. 76–86

[8] Williams T.L. *The Optical Transfer Function of Imaging Systems*. Institute of Physics Publishing, Bristol, Philadelphia, 1999

[9] Senoner M., Wirth Th., Unger W., Österle W., Kaiander I., Sellin R.L. et al.Testing the lateral resolution in the nanometre range with a new type of certified reference material. In: *Nanoscale Calibration Standards and Methods: Dimensional and Related Measurements in the Micro- and Nanometer Range*, (Wilkening G., & Koenders L.eds.). Wiley-VCH Weinheim, 2005, pp. 282–94.

[10] Williams C.S., & Becklund O.A. *Introduction to the Optical Transfer Function*. Wiley, New York, 1989

[11] den Decker A.J., & von den Bos A. Resolution: a survey. *J. Opt. Soc. Am. A Opt. Image Sci. Vis.* 1997, **14** pp. 547–557

[12] Cazaux J. Minimum detectable dimension, resolving power, and quantification of scanning Auger microscopy at high lateral resolution. *Surf. Interface Anal.* 1989 June/July, **14** (6/7) pp. 354–366

[13] Senoner M., & Unger W.E.S. Lateral resolution of Secondary Ion Mass Spectrometry — results of an inter-laboratory comparison. *Surf. Interface Anal.* 2007, **39** pp. 16–25

[14] Seah M.P. Resolution parameters for model functions used in surface analysis. *Surf. Interface Anal.* 2002, **33** pp. 950–953

[15] El Gomati M.M., & Prutton M. Monte Carlo calculations of the spatial resolution in a scanning Auger electron microscope. *Surf. Sci.* 1978, **72** pp. 485–494

[16] Powell C.J. Effect of backscattered electrons on the analysis area in scanning Auger microscopy. *Appl. Surf. Sci.* 2004, **230** pp. 327–333

[17] Egerton R.F., & Crozier P.A. The Effect of Lens Aberrations on the Spatial Resolution of an Energy-filtered TEM Image. *Micron*. 1997, **28** pp. 117–122

[18] Sherwood P.M.A.Appendix 3. Data Analysis in X-ray Photoelectron Spectroscopy. In: *Practical Surface Analysis by Auger and X-ray Photoelectron Spectroscopy*, (Briggs D., & Seah M.P.eds.). Wiley, Chichester, 1983, pp. 445–75.

[19] Seah M.P., Dench W.A., Gale B., Groves T.E. Towards a single recommended optimal convolutional smoothing algorithm for electron and other spectroscopies. *J. Phys. E Sci. Instrum.* 1988, **21** pp. 351–363

[20] Seah M.P., & Dench W.A. Smoothing and the signal-to-noise ratio of peaks in electron spectroscopy. *J. Electron Spectrosc. Relat. Phenom.* 1989, **48** pp. 43–54

[21] ORIGIN8 user guide available at <http://www.originlab.com/www/helponline/Origin/en/origin.htm>

[22] ISO/IEC Guide 98-3:2008, *Uncertainty of measurement — Part 3: Guide to the expression of uncertainty in measurement (GUM:1995)*

[23] Kirchhoff W.H., Chambers G.P., Fine J. An analytical expression for describing Auger sputter depth profile shapes of interfaces. *J. Vac. Sci. Technol. A*. 1986, **4** pp. 1666–1670

[24] Wight S.A., & Powell C.J. Evaluation of the shapes of Auger- and secondary-electron line scans across interfaces with the logistic function. *J. Vac. Sci. Technol. A*. 2006, **24** pp. 1024–1030

[25] Available at http://www.cstl.nist.gov/div837/Division/outputs/LFPF/LFPF.htm

[26] Senoner M., Wirth Th., Unger W.E.S. Imaging surface analysis: lateral resolution and its relation to contrast and noise. *J. Anal. At. Spectrom.* 2010, **25** pp. 1440–1452

[27] Rose A. The sensitivity Performance of the Human Eye on an Absolute Scale. *J. Opt. Soc. Am.* 1948, **38** pp. 196–208

[28] Unser M., & Trus B. L.and Steven, A. C. A new resolution criterion based on spectral signal-to-noise ratios. *Ultramicroscopy*. 1987, **23** pp. 39–52

[29] Kohl H., & Berger A. The resolution limit for elemental mapping in energy-filtering transmission electron microscopy. *Ultramicroscopy*. 1995, **59** pp. 191–194

[30] Ronzitty E., Vicidomini G., Caorsi V.and Diaspro, A. Annular pupil filter under shot-noise condition for linear and nonlinear microscopy. *Opt. Express*. 2009, **17** pp. 6867–6880

[31] de Jong A.F., & Van Dyck D. Ultimate resolution and information in electron microscopy – II. The information limit of transmission electron microscopes. *Ultramicroscopy*. 1993, **49** pp. 66–80

[32] Peng Y., Oxley M.P., Lupini A.R., Chisholm M.F., Pennycook S.J. Spatial Resolution and Information Transfer in Scanning Transmission Electron Microscopy. *Microsc. Microanal.* 2008, **14** pp. 36–47

[33] O'Keefe M.A. "Resolution" in high-resolution electron microscopy. *Ultramicroscopy*. 1992, **47** pp. 282–297

[34] Nellist P.D., McCallum B.C., Rodenburg J.M. Resolution beyond the "information limit" in transmission electron microscopy. *Nature*. 1995, **374** pp. 630–632

[35] Sato M., & Orloff J.A new concept of theoretical resolution of an optical system, comparison with experiment and optimum condition for a point source. *Ultramicroscopy*. 1992, **41** pp. 181–192

[36] Kalinin S.V., Jesse S., Rodriguez B.J., Shin J., Baddorf A.P., Lee H.N. et al. Spatial resolution, information limit, and contrast transfer in piezoresponse force microscopy. *Nanotechnology*. 2006, **17** pp. 3400–3411

[37] Bailly, A., Renault, O., Barrett, N., Desrues, T., Mariolle, D., Zagonel, L. F. and Escher, M.: Aspects of lateral resolution in energy-filtered core level photoelectron emission microscopy, *Journal of Physics: Condensed Matter*, 2009, vol. 21, 314002 (7pp)

[38] Vila-Comamala J., Jefimovs K., Raabe J., Pilvi T., Fink R.H., Senoner M. et al. Advanced Thin Film Technology for Ultrahigh Resolution X-Ray Microscopy. *Ultramicroscopy*. 2009, **109** pp. 1360–1364

[39] Machleidt, T., Sparrer, E., Kapusi, D. and Franke, K-H.: Deconvolution of Kelvin probe force microscopy measurements – methodology and application, *Measurement Science and Technology*, 2009, vol. 20, 084017 (6pp)

[40] King P.L. Artefacts in AES microanalysis for semiconductor applications. *Surf. Interface Anal.* 2000 Aug., **30** (1) pp. 377–382

[41] Barnes K.R. *The Optical Transfer Function*. American Elsevier Publishing Company, New York, 1971

[42] ISO 9334:2007, *Optics and photonics — Optical transfer function — Definitions and mathematical relationships*

[43] ISO 9335:1995, *Optics and optical instruments — Optical transfer function — Principles and procedures of measurement*

[44] Reimer L. *Scanning Electron Microscopy: Physics of Image Formation and Microanalysis*. Springer-Verlag, Berlin, 1998

[45] Reimer L. *Transmission Electron Microscopy: Physics of Image Formation and Microanalysis*. Chapter 6. Springer-Verlag, Berlin, Fourth Edition, 1997

[46] Escher M., Winkler K., Renault O., Barrett N. Applications of high lateral and energy resolution imaging XPS with a double hemispherical analyser based spectromicroscope. *J. Electron Spectrosc. Relat. Phenom.* 2010, **178-179** pp. 303–316

[47] Barinov, A., Dudin, P., Gregoratti, L., Locatelli, A., Mentes, O. N., Nino, M. A., and Kiskinova, M.: Synchrotron-based photoelectron microscopy, *Nuclear Instruments and Methods in Physics Research A*, March 2009, vol. 601, no. 1, pp. 195-202

[48] Cazaux J. Mathematical and physical considerations on the spatial resolution in scanning Auger electron microscopy. *Surf. Sci.* 1983 Feb., **125** (2) pp. 335–354

[49] Seah M.P. Quantification of AES and XPS, in Briggs, D, and Seah, M. P., editors: *Practical Surface Analysis – Vol. 1: Auger and X-ray Photoelectron Spectroscopy*, Wiley, Chichester, 1990, p. 242

[50] Goldstein J.I., Newbury D.E., Echlin P., Joy D.C., Romig A.D. Jr., Lyman C.E. et al. *Scanning Electron Microscopy and X-ray Microanalysis*. Chapter 3. Plenum, New York, 1992

[51] Reimer L. *Image formation in low-voltage scanning electron microscopy*. SPIE Press, Bellingham, 1993

[52] El Gomati M.M., Janssen A.P., Prutton M., Venables J.A. The interpretation of the spatial resolution of the scanning Auger electron microscope: A theory/experiment comparison. *Surf. Sci.* 1979 July, **85** (2) pp. 309–316

[53] El Gomati M.M., Prutton M., Lamb B., Tuppen C.G. Edge effects and image contrast in scanning Auger microscopy: a theory/experiment comparison. *Surf. Interface Anal.* 1988 Mar., **11** (5) pp. 251–265

[54] Baer D.R., & Engelhard M.H. Approach for determining area selectivity in small-area XPS analysis. *Surf. Interface Anal.* 2000 Nov., **29** (11) pp. 766–772

[55] Scheithauer U. Quantitative Lateral Resolution of a Quantum 2000 X-ray Microprobe. *Surf. Interface Anal.* 2008, **40** pp. 706–709

[56] Seah M.P., & Mathieu H.J. Method to determine the analysis area of X-ray photoelectron spectrometers – Illustrated by a Perkin-Elmer PHI 550 ESCA/SAM. *Rev. Sci. Instrum.* 1985 May, **56** (5) pp. 703–711

[57] Erickson, N. E., and Powell, C. J.: Characterization of the imaging properties of a double-pass cylindrical-mirror analyzer, *Surface and Interface Analysis*, July 1986, vol. 9, nos. 1-6, pp. 111-117

[58] Erickson N.E., & Powell C.J. Imaging properties and energy aberrations of a double-pass cylindrical-mirror analyzer. *J. Vac. Sci. Technol. A*. 1986 May-June, **4** (3) pp. 1551–1556

[59] Grazulis L., & Grant J.T. Real-time imaging of analyzed areas in surface analysis. *Rev. Sci. Instrum.* 1986 Sep., **57** (9) pp. 2326–2331

[60] Tomich D.H., Grazulis L., Koenig M.F., Grant J.T. Applications of a system for real-time imaging of analyzed areas in surface analysis. *Surf. Interface Anal.* 1988 Mar., **11** (5) pp. 243–250

[61] Seah M.P., Spencer S.J., Bodino F., Pireaux J.J. The alignment of spectrometers and quantitative measurements in X-ray photoelectron spectroscopy. *J. Electron Spectrosc. Relat. Phenom.* 1997 Dec., **87** (2) pp. 159–167

[62] Cazaux J. Capabilities and limitations of high spatial resolution A.E.S. *J. Surf. Anal.* 1997 Mar., **3** (2) pp. 286–311

[63] Cazaux J., Chazelas J., Charasse M.N., Hirtz J.P. Line resolution in the sub-ten-nanometer range in SAM. *Ultramicroscopy*. 1988 May, **25** (1) pp. 31–34

[64] Postek M.T., & Vladar A.E. Image sharpness measurement in scanning electron microscopy — Part I. *Scanning*. 1998 Jan., **20** (1) pp. 1–9

[65] Vladar A.E., Postek M.T., Davidson M.P. Image sharpness measurement in scanning electron microscopy — Part II. *Scanning*. 1998 Jan., **20** (1) pp. 24–34

[66] Seah, M. P., and Smith, G. C.: Concept of an imaging XPS system, *Surface and Interface Analysis*, Jan. 1988, vol. 11, nos. 1 and 2, pp. 69-79

[67] Senoner M., Wirth Th., Unger W.E.S., Escher M., Weber N., Funnemann D. et al. Testing of lateral resolution in the nanometre range using the BAM-L002 - Certified Reference Material: Application to ToF-SIMS IV and NanoESCA instruments. *J. Surf. Anal.* 2005, **12** pp. 78–82

[68] ASTM E 1217-00, *Standard Practice for Determination of the Specimen Area Contributing to the Detected Signal in Auger Electron Spectrometers and Some X-Ray Photoelectron Spectrometers*

[69] Grant J.T., Hooker M.P., Springer R.W., Haas T.W. Comparison of Auger spectra of Mg, Al, and Si excited by low-energy electron and low-energy argon ion bombardment. *J. Vac. Sci. Technol.* 1975 Jan./Feb., **12** (1) pp. 481–484 [1]

ICS 71.040.40

Price based on 116 pages